I

BACKSCATTERING AND CHANNELING EFFECT STUDIES

ON SEMICONDUCTOR-METAL SYSTEMS

II

LOW TEMPERATURE MIGRATION OF SILICON

THROUGH METAL FILMS

Thesis by

Eriabu Lugujjo

In Partial Fulfillment of the Requirements for the Degree of

Doctor of Philosophy

California Institute of Technology

Pasadena, California

(Submitted Jan. 29, 1974)

To my Father and Grandmother

iv

Special thanks are extended to Mrs. Betty Mayer, Mrs. Paula Samazan and Mrs. Karen Current who have helped me at one time or another during my stay at Caltech. For her skillful handling of a difficult typing job, I thank Mrs. Carol Norris.

I am very grateful to my sponsors, the Afrikan-American Institute, New York, who brought me to this country, placed me in a graduate school and at the same time provided financial support for the entire program. Special thanks go to Miss Jill Haas and Mrs. Heather Monroe of the above organization for giving me the initial phychological therapy for the American educational system.

Research financial assistance from L. Cooper is gratefully acknowledged.

ABSTRACT

PART I

Channeling measurements by backscattering of He and H ions have been made on <111>- and <110>-oriented Si covered with evaporated layers of Al and Au. The energy range was 0.4 - 1.8 MeV and the film thicknesses ranged between 100 and 1100Å for Au, and between 900 and 3000Å for Al. As a first approach to analysis of disorder in crystals, we have investigated the effects of simulated disorder in form of metal layers on the surface of Si and Ge. This has an advantage in that particle scattering in the metal films can be controlled independently of scattering in the underlying substrate. The minimum yield, half-width of the angular-yield profile and the depth dependence of aligned yield have been studied as a function of metal-film thickness and beam energy. Comparisons between experimental and calculated values have been made on the basis of two different treatments of plural scattering.

The minimum yield values obtained by applying only a step-function approximation to the angular yield profile were first evaluated as a function of film thickness. The minimum yield, angular-yield profiles and dechanneling dependence on depth obtained with Al films follow the

predictions of Meyer's treatment of plural scattering.

A detailed study of minimum yield values on covered Si was then made. In this case the minimum yield was calculated from the Meyer treatment and probability curves determined from (i) a step-function approximation to the angular-yield profile, and (ii) two different axial scans on uncovered Si, one of which is azimuthally averaged. The minimum yields calculated using the step-function approximation and average probability curves are in good agreement with experimental results. This suggests that the step-function approximation, although less accurate than the azimuthally averaged procedure, is adequate for use with investigations of disorder in crystals by channeling-effect measurements. On the basis of the step-function approximation, we have established universal curves from which minimum yield values as a function of disorder may be obtained.

PART II

The backscattering spectrometry using 2 MeV He^+ ions have been employed to study the phenomenon of low-temperature migration of Si through thin films of Au and Ag evaporated on <110> and <111> Si single crystal substrates. The thicknesses of Au films ranged from 200 to 4000Å, and those of Ag from 200 to 800Å. Migration of Si into these metal films is observed when the systems are

heat treated in an oxidizing ambient at low temperatures
(150°C for Au, 400°C for Ag), well below their eutectic
points (375°C for Au and 830°C for Ag).

The migration of Si is followed by formation of a
silicon-oxide layer on top of the metal film. The initial
growth of this oxide layer is proportional to $(\text{time})^{\frac{1}{2}}$. The
factors controlling this low-temperature oxide formation
have been investigated. Both oxidizing ambient and orien-
tation of the substrate influence the oxide growth rate,
and the thickness of evaporated film determines the final
thickness of the oxide. A model to explain the oxide-growth
mechanism is presented.

The migration of Si also has been studied through
layers of Au with superimposed layers of Ag, and vice
versa. It is found that the interface between Si and the
metal film plays a leading role in these low-temperature
migration studies.

Some aspects of the work contained in this thesis
have been published previously under the following titles:

"Channeling in Si Overlaid with Al and Au films,"
Phys. Rev. $\underline{B6}$, 718 (1972), E. Rimini, E. Lugujjo and J.W.
Mayer.

"Energy Dependence of He^+ and H^+ Channeling in Si
Overlaid with Au films," Phys. Rev. $\underline{B7}$, 1782 (1973), E.
Lugujjo and J.W. Mayer.

"Low-Temperature Migration of Si through Metal

Films: Importance of Silicon-Metal Interface," Phys. Status
Solidi(a) 7, 401 (1971), A. Hiraki, E. Lugujjo, M-A. Nicolet
and J.W. Mayer.

"Formation of Silicon Oxide over Gold Layers on
Silicon Substrates," J. Appl. Phys. 43, 3643 (1972), A.
Hiraki, E. Lugujjo and J.W. Mayer.

Other publications not included in this thesis are:

"Low-Temperature Migration of Silicon in Metal
Films on Silicon Substrates Studied by Backscattering Tech-
niques," J. Vac. Sci. Technol. 9, 155 (1972), A. Hiraki
and E. Lugujjo.

"Influence of Scattering in MeV He$^+$ Channeling in
Si Overlaid with Amorphous Films," Phys. Lett. 37A, 157
(1971), E. Rimini, E. Lugujjo and J.W. Mayer.

"Channeling in Si Overlaid with Dielectric Layer,"
Presented in the International Conference on Ion Beam Sur-
face Layer Analysis, Yorktown Heights, New York, June 18,
1973, W.K. Chu, E. Lugujjo, J.W. Mayer and T.W. Sigmon.

"Optical Line and Broad-band Emission from Ion-
Bombarded Targets," Presented at the 5th International
Conference on Atomic Collision in Solids, Tennessee,
Sept. 1, 1973, W.F. van der Weg and E. Lugujjo.

"Stoichiometry of Thin Silicon Layers on Silicon,"
Phys. Lett. (in press), T.W. Sigmon, W.K. Chu, E. Lugujjo
and J.W. Mayer.

ix

TABLE OF CONTENTS

PART I

BACKSCATTERING AND CHANNELING EFFECT STUDIES

ON SEMICONDUCTOR-METAL SYSTEMS

I. INTRODUCTION

A. General

Experimental and theoretical studies have established that the channeling of an energetic beam of particles in a single crystal occurs whenever a crystal axis or plane is aligned with the incident-beam direction. In the channeling process, the incident particles are steered by a series of gentle collisions with the lattice atoms of the rows or planes. In order for an energetic beam of particles to be steered by the lattice, the beam direction must be oriented within a certain critical angle ($\psi_{\frac{1}{2}}$) of the crystal axis or plane. The effect of channeling on particle trajectories in the crystal is most strikingly observed in the significant reduction in the measured yield of processes requiring a close encounter with the lattice atoms. Such processes include wide angle elastic scattering, Coulomb excitation, nuclear reactions and production of inner shell x-rays.[1-4]

The reduction in the yield of these processes is very sensitive to crystalline imperfections both on the surface and inside the crystal and has been used to determine disorder distributions in ion-implanted samples[4-7] and in epitaxially grown single-crystal layers.[8,9] The yield of close-encounter process is, in fact, influenced

by the initial distribution in transverse momentum of
the particles as they enter the crystal and also by scat-
tering from off-lattice atoms in addition to the normal
scattering events experienced in a perfect crystal. Super-
position of amorphous layers on single crystals causes a
spreading in the angular distribution of the incident beam
due to scattering events in the film. This increase in
transverse momentum leads to an increase in the aligned
yield as has been found for silicon covered with dielectric
layers[8,10] and metal films.[11,12] A similar increase in
aligned yield is also observed in crystals containing
lattice disorder such as ion implanted Si.[13]

Analysis of channeling effects in imperfect
crystals requires knowledge of the transverse momentum
and of the probability that a particle with a given trans-
verse momentum will be transferred out of the aligned
component into the random component of the beam (de-
channeled). For the dechanneling probability it is
always assumed (step-function approximation) that a
particle is in the random component of the beam when its
angle with the channel axis is greater than $\psi_{\frac{1}{2}}$, the
critical angle for channeling. In channeling measurements
of disorder, various scattering treatments have been used
to obtain the angular distributions of the particles:
single,[4,14] plural,[6] and multiple[4,5] scattering.
These scattering regimes are classified according to the

mean value m of the number of collisions. A single-scattering regime is characterized by m << 1. For m >> 1 (m > 20), the number of scattering events is large and the process is called multiple scattering. In between single- and multiple-scattering regimes lies plural scattering.

A plural-scattering treatment seems most reasonable to apply to the small numbers of scattering centers typically encountered in disorder analyses of ion-implanted or epitaxial layers. Early estimates of plural scattering were based on the treatment of Keil et al.,[15] who used the Moliére cross section.[16] This treatment leads to a strongly peaked forward scattering distribution. Recently a new treatment of plural scattering has been proposed by Meyer[17] on the basis of Thomas-Fermi cross sections. This treatment does not lead to as strongly a peaked distribution as that of Keil et al. Experimental measurements[18,19] of scattering of heavy ions of keV energies transmitted through thin films show good agreement with calculations based on the Meyer treatment. For large numbers of scattering centers, the two treatments give the same distribution which merges with the Moliére multiple scattering theory. For a general reference to multiple scattering in the high-energy regime, see Scott.[20]

At the start of this study, there had not been an evaluation of the applicability of the Meyer treatment of plural scattering to channeling analysis of disorder in

crystals. To carry out this evaluation of channeling analysis we devised a simple technique to simulate disorder. This has been achieved by covering the single crystals with an evaporated layer of metal films. The aim was to obtain a direct test of the more appropriate distribution to be used to extract disorder profiles by channeling-effect measurements. Use of an evaporated amorphous metal layer allows a more direct analysis because the amount of scattering in the film can be controlled independently of the underlying substrate. This study has centered on the investigation of the dependence of the minimum yield values and dechanneling rates on metal layer thicknesses and beam energies. A comparison of these experimental measurements with those calculated using existing plural scattering treatments has been made.

B. Scattering

When an energetic particle is scattered through an angle, the scattering may be the result of the accumulated effect of a number of small deflections produced by different atomic nuclei in the matter traversed, or it may be due to a single deflection through the same angle produced by some one nucleus.[21] The first type of scattering is spoken of an "multiple" or "plural", depending on whether the number of contributing collisions is large or small. The second type is referred to as 'single' scatter-

ing. The extent to which either process dominates depends on the nature and velocity of the scattering particle, the matter traversed and the scattering angle. [22]

Single scattering dates back to Rutherford in the first decade of this century. [23] Rutherford's alpha-particle scattering experiments (1911) aroused great interest in the study of the interaction of charged particles with matter. Plural and multiple scattering were first studied theoretically by Wentzel (1922) who recognized [24] that some of Rutherford's later scattering experiments were not only due to single scattering but to a combination of both single and multiple scattering. Nearly two decades later E.J. Williams (1939, 1940) worked out a moderately successful theory of multiple scattering based on a method of fitting together a Gaussian curve for the central part of the distribution and a single scattering tail for large angles. [22,25] A more refined treatment of multiple scattering was developed in 1948 by Moliére. [16] This treatment was based on the statistical procedure of Wentzel. [24] In 1960 Keil et al. [15] evaluated scattering distributions in the plural scattering regime using Moliére's differential cross section. Recently a new treatment of plural scattering has been advanced by Meyer. [17] This treatment modifies the analysis developed by Keil et al. with respect to the differential scattering cross section. In this case the Thomas-Fermi potential was used.

Shown in Fig. 1 are the angular distributions of the number of 1.8 MeV He particles scattered per steradian in traversal of an 88Å Au film and 1550Å Al film. The film thicknesses are specified by the parameter m which is given by[17]

$$m = \pi (a_{TF})^2 Nt \qquad (1)$$

where a_{TF} is the Thomas-Fermi screening parameter ($a_{TF} = 0.105$Å for Au and $a_{TF} = 0.176$Å for Al), N is the number of atoms per $(Å)^{-3}$, and t is the film thickness in angstroms. Physically, m is the mean value of the number of collisions experienced by particles traversing a target with Nt atoms with a cross section of $\pi (a_{TF})^2$.

The angular distributions $f(\theta)$ were obtained directly from the Keil et al. and Meyer tabulations. For low values of m the Keil treatment predicts that a large fraction (proportional to e^{-m}) of the beam passes through the film without deflection. For instance, for m = 0.2 the integrated distribution $\int_0^\infty f_{0.2}^K (\theta) 2\pi\theta \, d\theta$ is 0.18, indicating that 82% of the particles are undeflected for an 88Å thick Au film. On the other hand, in the Meyer treatment, all the particles are scattered ($\int_0^\infty f_{0.2}^M (\theta) 2\pi\theta \, d\theta = 1$). In both cases, the distribution becomes broader with increasing values of m. For large values of m (m > 20, Au $\geq$ 9000Å, and Al $\geq$ 3000Å), the two distribution approach the Moliére

Figure 1. Differential angular distributions $f(\theta)$ for 1.8 MeV He$^+$ ions after traversing a reduced thickness m = 0.2 (88Å of Au) and m = 10 (1550Å of Al) according to the Meyer (Ref. 17) treatment (full lines) and Keil et al. (Ref. 15) treatment (dashed lines). The integral of the differential distribution for m = 0.2 is 0.181 in the Keil et al. treatment. The experimental values of the critical angle for Si <111>, <110> and {110} are shown on the bottom left.
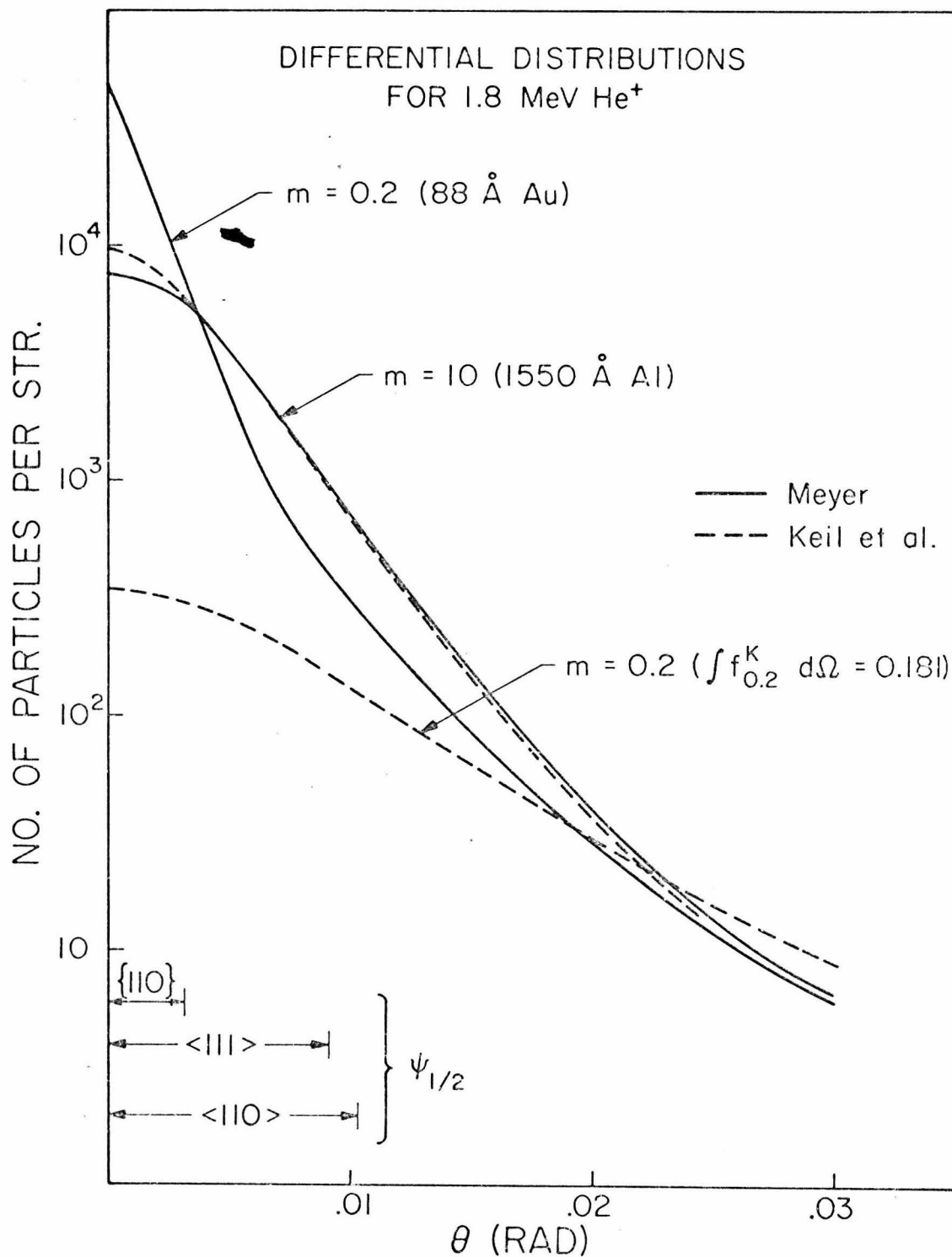
Figure 1

analytical computations.

As a further comparison of the two treatments the projected planar differential distributions are shown in Fig. 2. We consider the number of particles scattered through the angle θ_p with respect to the plane, i.e. the projection of the angle θ on a surface both normal to the plane and parallel to the beam direction,

$$f_p(\theta_p) = 2 \int_0^\infty d\phi \; f[(\theta_p^2 + \phi^2)^{1/2}] \qquad (2)$$

The distributions shown correspond to 1.8 MeV He$^+$ traversing a reduced thickness m = 0.6 (264Å of Au). For m = 0.6 we have $2 \int_0^\infty f_p^M(\theta_p)d\theta_p = 1$ and $2 \int_0^\infty f_p^K(\theta_p)d\theta_p = 0.45$, where $f_p^M(\theta_p)$ and $f_p^K(\theta_p)$ refer to Meyer and Keil et al. angular distributions, respectively. The arrow in the Keil et al. distribution indicates the undeflected part of the beam which amounts to 55%.

C. Channeling and Backscattering

The main purpose of this section is to introduce the basic concepts of channeling and backscattering as will be applied in this work. Channeling in single crystals is described on the basis that a particle moving at a small angle with respect to a row or plane of atoms is steered by a series of gentle correlated collisions with many

Figure 2. Planar differential distributions $f_p(\theta_p)$ for 1.8 MeV He^+ ions after traversing a reduced thickness m = 0.6 equivalent to 264$\overset{o}{A}$ of Au, according to Meyer (full line) and Keil et al. (dashed line).
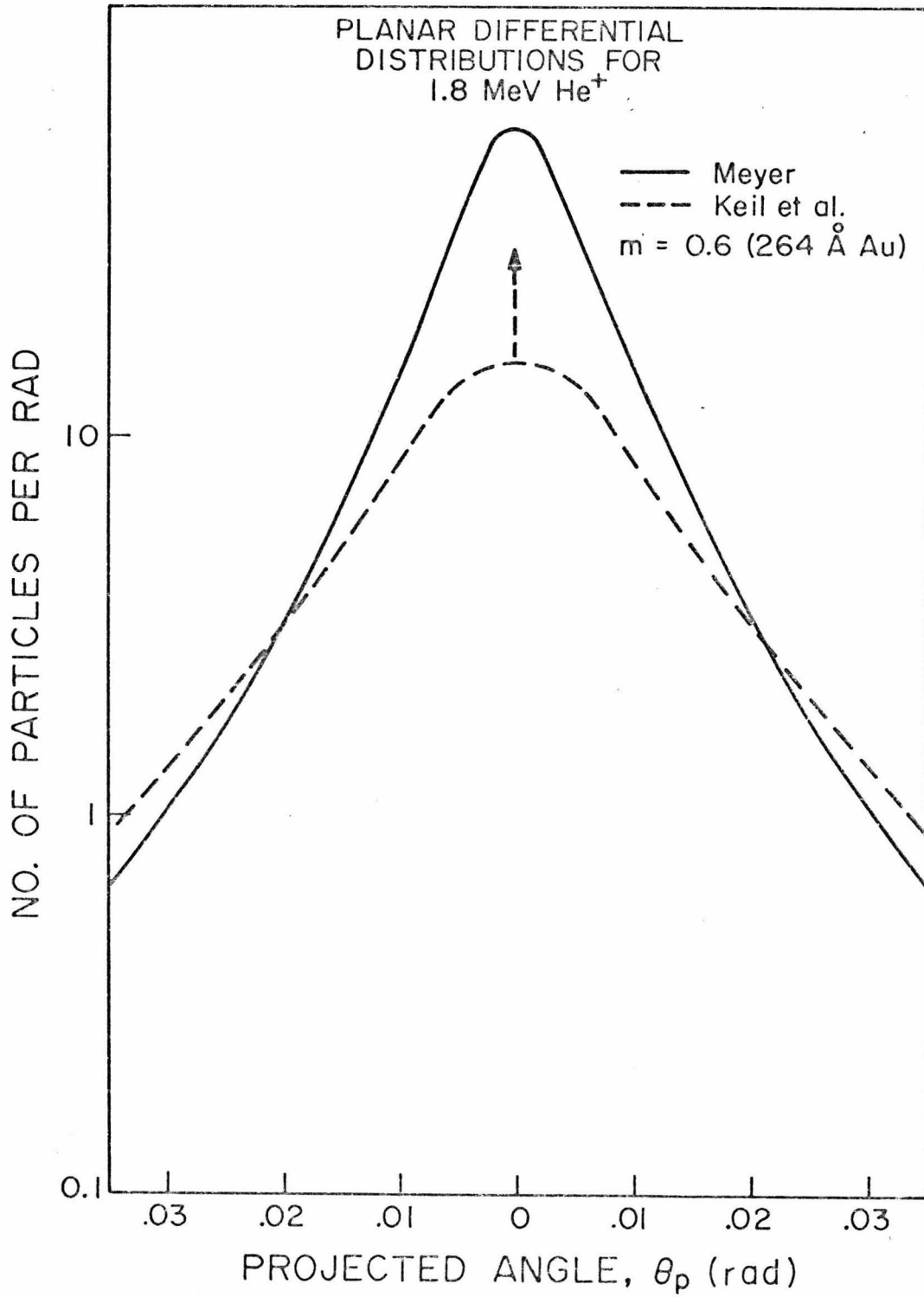
Figure 2

lattice atoms in the row or plane.[26,27] The requirement that the individual atomic collisions be gentle implies that the deflection given to the particle during a single collision is small compared to the total angle through which the particle is steered.

In Lindhard's treatment,[26] the steering of the particle is described by its interaction with the average potential of the row or plane. The discrete atomic potentials are replaced by a continuum model giving an average potential $\bar{V}(r)$ depending only on the perpendicular distance r from the row or plane. If the energy $E_\perp$ for the transverse motion of the particle is insufficient to overcome the potential barrier presented by the lattice row then one may write[27]

$$E_\perp = \bar{V}(r) + \frac{1}{2} M(v \sin \psi)^2 \cong \bar{V}(r) + E\psi^2 \qquad (3)$$

where $(1/2)Mv^2$ is the kinetic energy E of the incident particle, ψ the instantaneous angle of incidence of the particle with respect to the row and $\bar{V}(r)$ the average potential at an impact parameter r with the row. The minimum impact parameter (r_{min}) corresponds to the maximum or "critical" angle $(\psi = \psi_{1/2})$ for which the particle can be steered by the crystal row. Thus from Eq. 3

$$\psi_{1/2} = \sqrt{\frac{|V(r_{min})|}{E}} \qquad (4)$$

For axial channeling we have

$$\psi_{1/2} = \alpha\psi_1, \quad \text{for } (\psi_1 < a_{TF}/\alpha) \tag{5}$$

where

$$\psi_1 = \left[\frac{2Z_1 Z_2 e^2}{Ed}\right]^{\frac{1}{2}} \tag{6}$$

is the Lindhard critical angle for a static lattice and

$$\alpha = \left[\frac{1}{2} \log\left(\frac{3(a_{TF})^2}{\rho_r^2 \log 2} + 1\right)\right]^{\frac{1}{2}} \quad \text{for } (\psi_1 < \frac{\rho_r}{d}) \tag{7}$$

is a parameter calculated by Picraux et al.[28] and accounts for the thermal vibrations. Detailed numerical calculations by J.U. Andersen[29] have shown that Eq. 7 is accurate in the region $\psi_1 < \rho_r/d$. Z_1, Z_2 are projectile and lattice atomic numbers, d is the spacing along the row and ρ_r^2 the mean square vibrational amplitude of the lattice atoms in the plane perpendicular to the row. The main functional dependence of the critical angle is contained in ψ_1 which involves energy, atomic number and lattice spacing. It should be noted that $Z_2 e/d$ is simply the nuclear charge per unit distance along the row.

The main channeling principles discussed above are summarized in Fig. 3. If the angle of approach is well

Figure 3. Influence of crystal lattice on the motion of
energetic charged particles. Upper Part: Charged
particle trajectories for several typical values
of θ, the angle between the incident beam and a
close-packed atomic row. Random trajectory is
indicated by C. The channeled beam A does not
approach closer than $\sim 0.1\text{Å}$ (the Thomas-Fermi
screening distance) to the row. Lower Part:
shows angular dependence of the yield for any
process requiring impact parameters $\sim 0.1\text{Å}$. The
lowest height of the yield curve corresponds to
minimum yield χ_o. The dotted curve shows the
predicted angular dependence for a perfect non-
vibrating lattice.
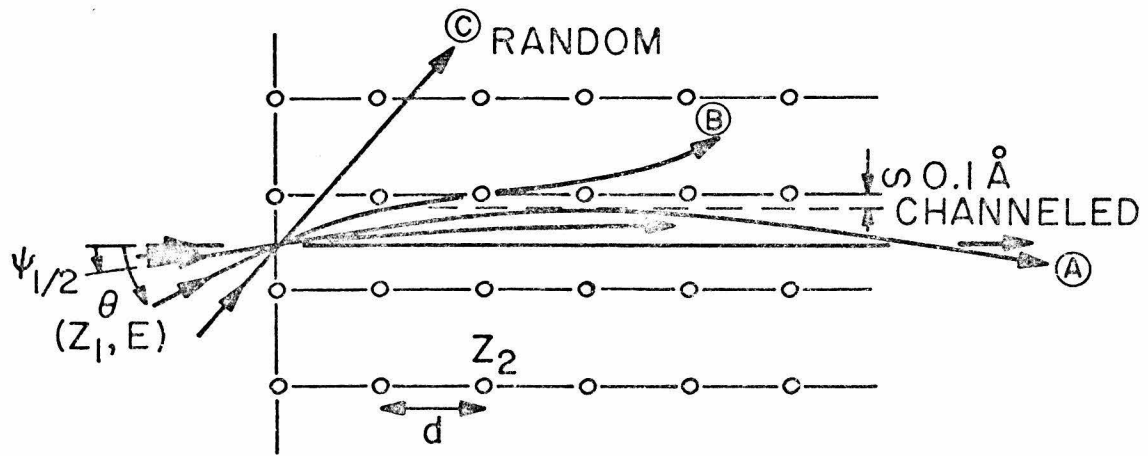
$$\psi_{1/2} = \sqrt{\frac{2Z_1 Z_2 e^2}{Ed}}$$
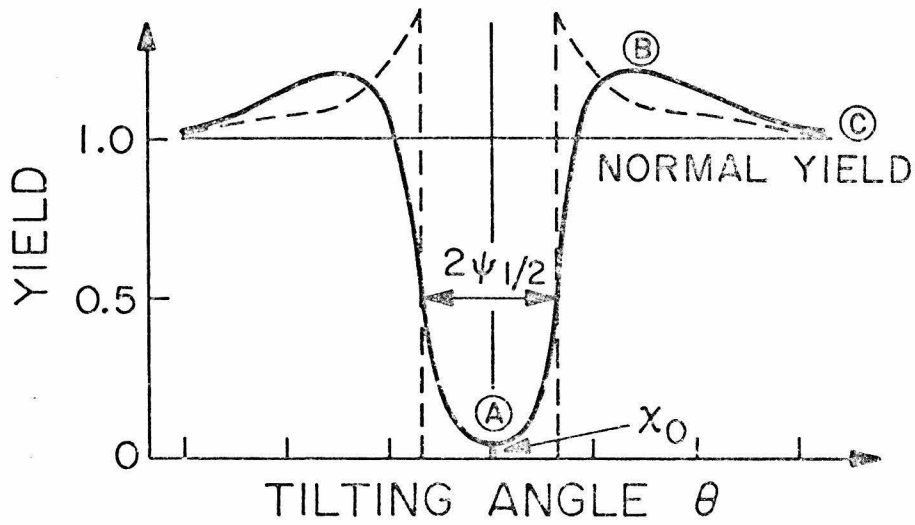
Figure 3

outside the critical angle $\psi_{\frac{1}{2}}$ (trajectory C), the particle has no "feeling" for the existence of a lattice and experiences a random trajectory and stopping. For angles of approach only slightly larger than the critical angle $\psi_{\frac{1}{2}}$, the particle actually has a somewhat higher probability of being close to atomic rows and experiences an abnormally high stopping. Such a trajectory is indicated by B. A channeled particle (trajectory A) will have an angle of approach, θ, that is smaller than $\psi_{\frac{1}{2}}$. The lower part of Fig. 3 shows a typical angular normalized yield curve (profile) for a close-encounter process taken just beneath the crystal surface. There is a striking attenuation in the yield when the angle of approach is close to zero. On the yield curve is shown the correlation with the trajectories A, B and C. The dotted curve indicates the shape one would expect for a perfect lattice with no thermal vibration. The lowest height of the yield curve corresponds to what is known as the 'minimum yield' designated χ_0. The minimum yield is defined as the ratio of the number of backscattered particles when the incident beam is aligned (channeled) with the crystal-symmetry direction of interest to the number with the beam far from any high-symmetry direction of the crystal (random direction). The minimum yield is a useful parameter to study experimentally since it provides a direct comparison with theory as will be described in Section III.

In planar channeling, an averaged sheet potential for the case of uniformly spaced planes is used and leads to a planar critical angle[28]

$$\psi_{\frac{1}{2}} = \beta\psi_1 \quad \text{for } (\psi_1 < 2Nd_p a_{TF}^2) \tag{8}$$

where

$$\psi_1 = \left[\frac{z_1 z_2 e^2 Nda_{TF}}{E} \right]^{\frac{1}{2}} \tag{9}$$

and N is atomic density, d_p is the spacing between planes, a_{TF} is the Thomas-Fermi screening distance and the factor of β is of the order of unity.

In this work we have used wide angle scattering process in investigating the channeling effect. Two typical energy spectra for 1.8-MeV He^+ backscattered from a silicon single crystal are shown in Fig. 4. The aligned spectrum or aligned yield refers to the backscattering spectrum in which the incident He^+ beam is aligned parallel to a low index Si crystal axis namely ⟨111⟩. The random yield or random spectrum refers to that in which the incident beam is far from any symmetry axis or plane, so that no steering of the incident particles occurs. The high energy edges of the spectra correspond to scattering near the surface. Lower energies correspond to particles scattered at increasing depths in the crystal.

Figure 4. Energy spectra for 1.8 MeV He$^+$ ions back-
scattered from uncovered Si crystal for random
($\bullet$) and <111>-aligned direction (Δ).

Figure 4

Energy spectra for 1.8-MeV He$^+$ backscattered from an uncovered silicon crystal tilted at various angles with respect to the <110> aligned direction are shown in Fig. 5. The yield near the surface has a dependence on crystal orientation similar to that shown in lower part of Fig. 3. The increase of the yield with depth (de-channeling rate) depends on the beam to substrate orien-tation. The dechanneling rate increases due to the change in transverse energy distribution (and thus angular dis-tribution) of the incident beam.

Channeling effect measurements with the backscat-tering technique can be used as a tool to investigate the small angle scattering events in amorphous layers. Further-more, this information can be used in extracting disorder distributions in crystalline materials. Figure 6 shows two angular yield profiles for 1.8-MeV He$^+$ impinging along the <110> direction of a silicon sample. These profiles correspond to yield of particles backscattered from just beneath the crystal surface as a function of tilt angle for uncovered Si and Si covered with 2130Å of Al. The shapes of these yield profiles differ between uncovered and covered Si not only for the minimum yield, but also for the value of the width, defined as the full width at a level midway between the random and aligned yield. This difference in yield between covered and uncovered Si arises from small angle scattering in the amorphous layer. This
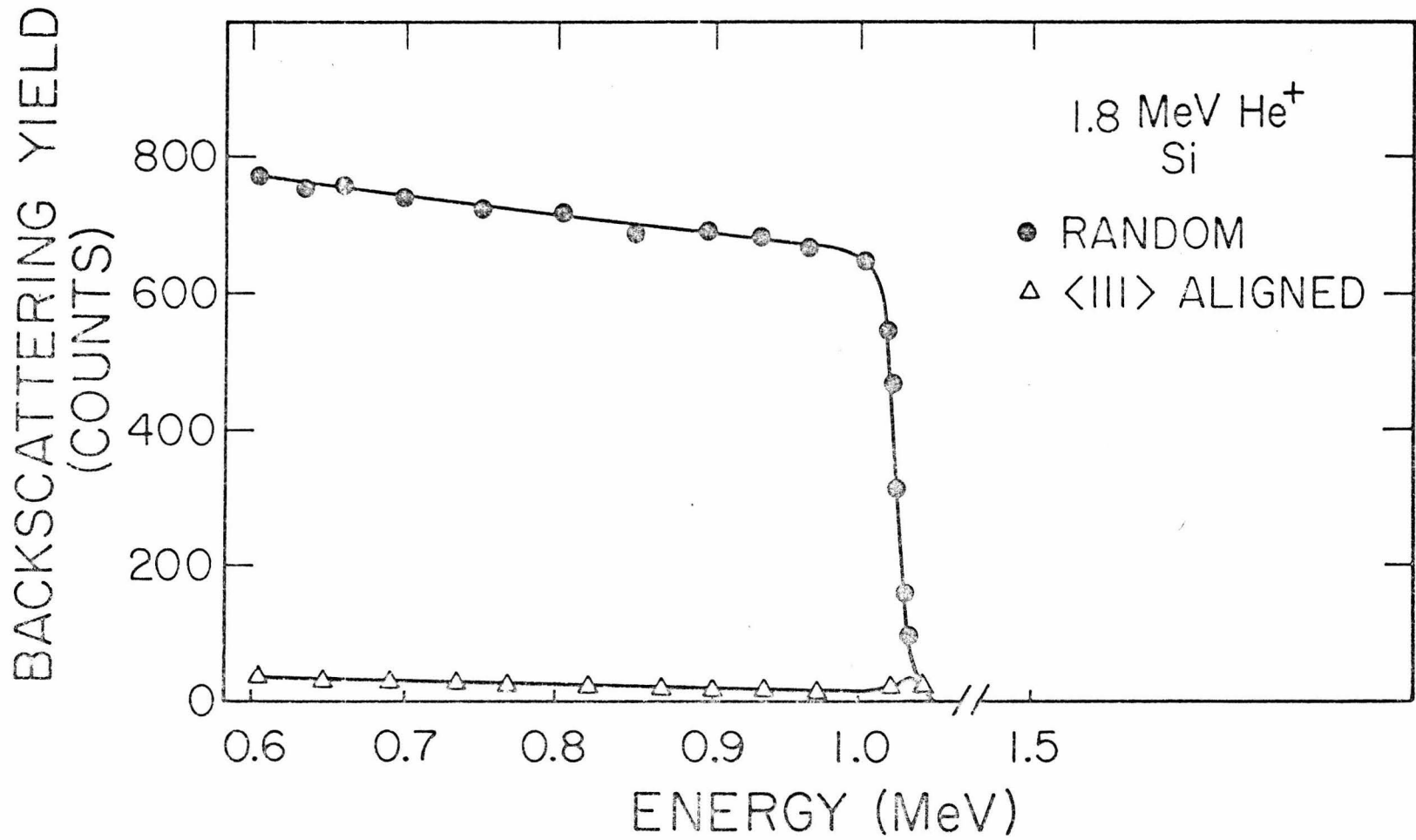
Figure 5. Energy spectra for 1.8 MeV He$^+$ ions back-
scattered from an uncovered silicon crystal
tilted at various angles with respect to the
aligned direction.
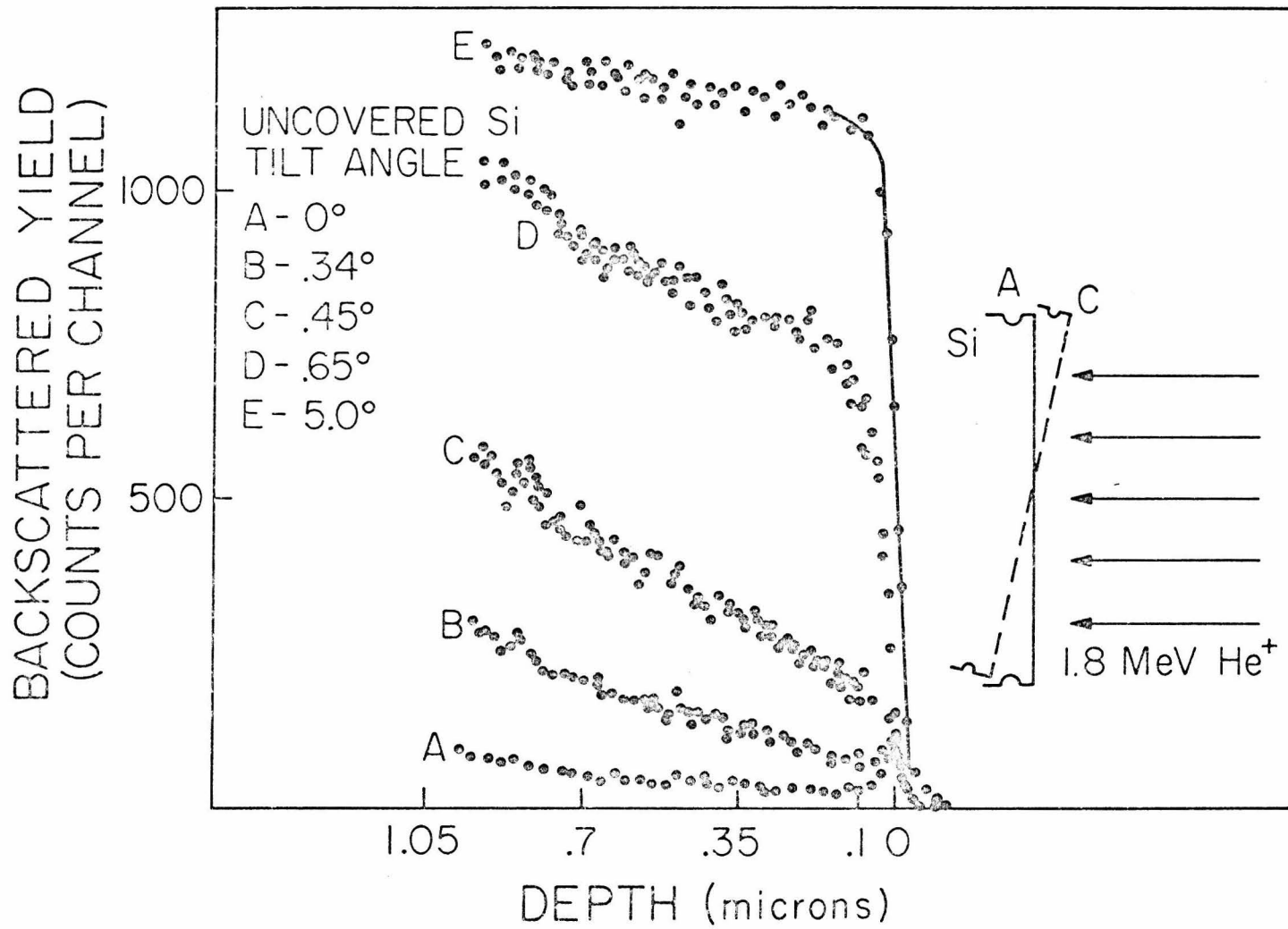
Figure 5

Figure 6. Normalized yield vs tilt angle for 1.8 MeV He$^+$ ions incident along the <110> direction of un-covered Si crystal (●) and Si covered with 2130Å of Al (▩). The yields were measured at depths about 0.1 μ below the surface and normalized to 2500 counts.
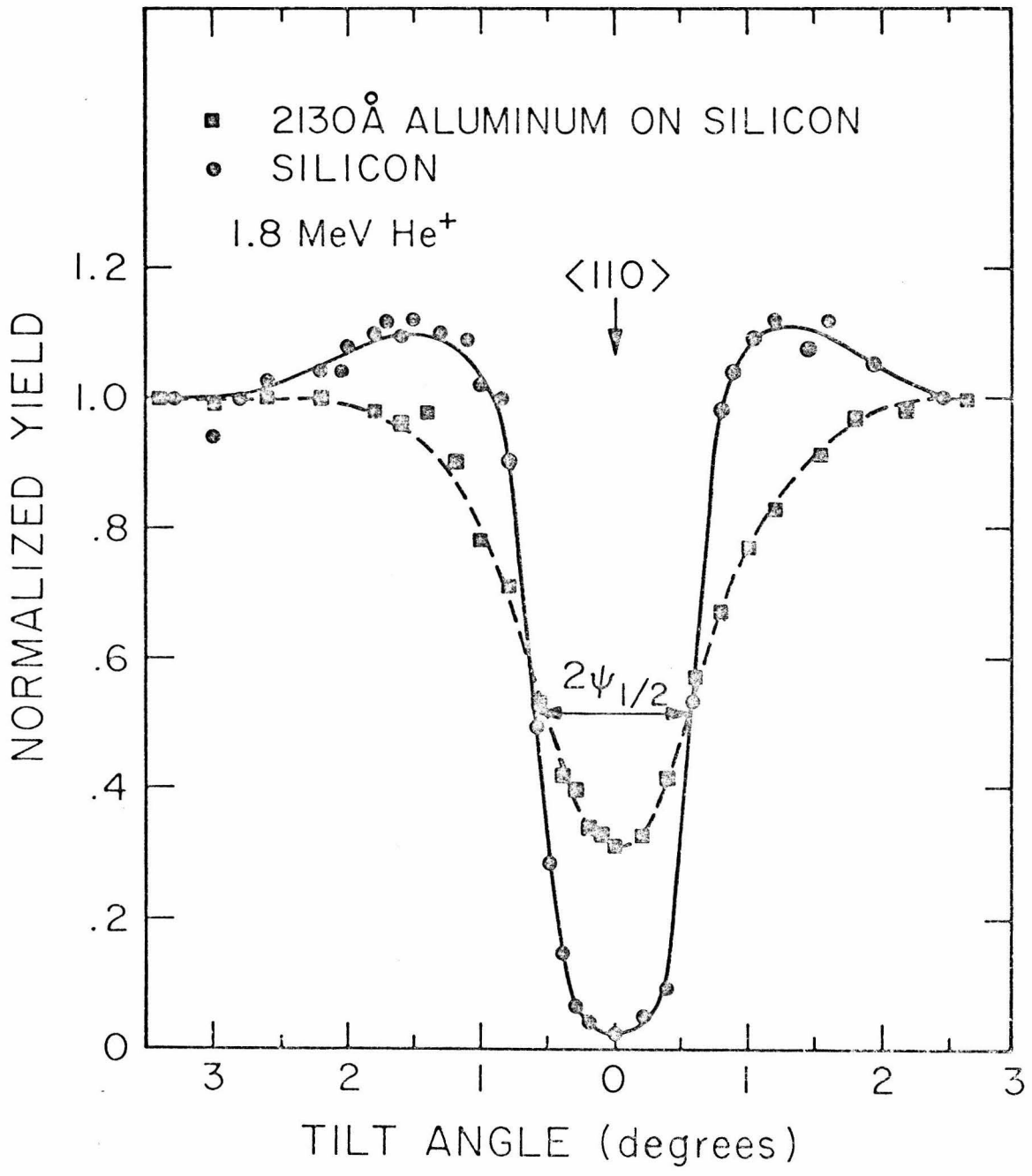
Figure 6

scattering introduces a broadening of angular distribution of the beam and consequently reduces the fraction of the beam along the aligned crystal direction.

The role played by the scattering in the amorphous layer on the angular yield profile is further demonstrated in Fig. 7. Here a planar scan is made across the ′{110} plane on uncovered Si and Si covered with 3090$\overset{\circ}{A}$ of Al. The minimum yield values and the width of the yield profile increase.

Figure 7. Normalized yield vs rotation angle for 1.8 MeV
He$^+$ ions impinging on the ´{110} plane of uncovered
Si crystal (●) and Si covered with 3090Å of Al
(▣).
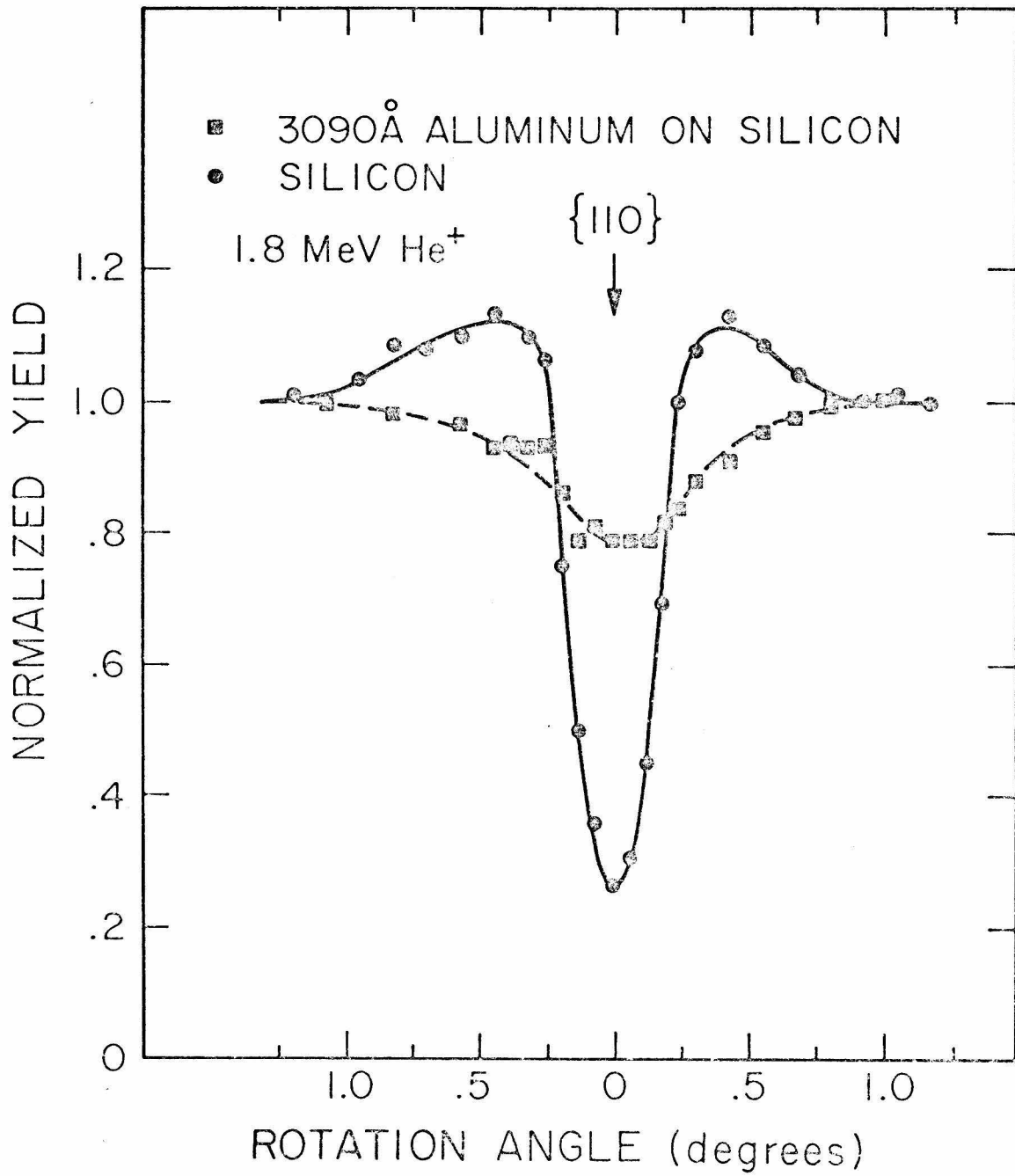
Figure 7

II. EXPERIMENTAL

A. Sample Preparation and Channeling Measurements

Gold films from 100 to 1000Å thick and aluminum films from 900 to 3000Å thick were vacuum deposited from a tungsten filament onto the <110> and <111> surfaces of silicon and germanium single crystals at room temperature. The evaporation of Al and Au was made on samples masked so that in the same sample there were portions of uncovered Si, Si plus Au and Si plus Al. The evaporations were made in a vacuum of about 5×10^{-7} Torr.

Channeling measurements were made using the backscattering technique.[1,10] Low-energy (400-keV) and high-energy (1.0 to 1.8 MeV) channeling experiments were done using accelerators at Rockwell International Science Center and Caltech, respectively. Collimated beams ($\sim$ 2mm beam diameter) of protons and helium ions were incident on samples mounted on a two-axis goniometer in a scattering chamber. A schematic sketch of the scattering chamber and electronics is shown in Fig. 8. The samples could be rotated and tilted with respect to the incident beam. The scattering chamber was evacuated to less than 10^{-5} Torr and secondary electrons were suppressed. The particles backscattered from the target through a laboratory angle θ = 164, i.e. θ' = 16 (see Fig. 8) were detected by a

Figure 8. Schematic diagram of experimental geometry of
backscattering analysis equipment. The incoming
beam strikes the sample at normal incidence and
particles scattered into an angle θ' are ana-
lyzed with a solid state silicon surface-barrier
detector. The output of the detector is amplified
and stored in a 400-channel pulse height analyzer.
The two-axis goniometer was used in channeling
experiments.
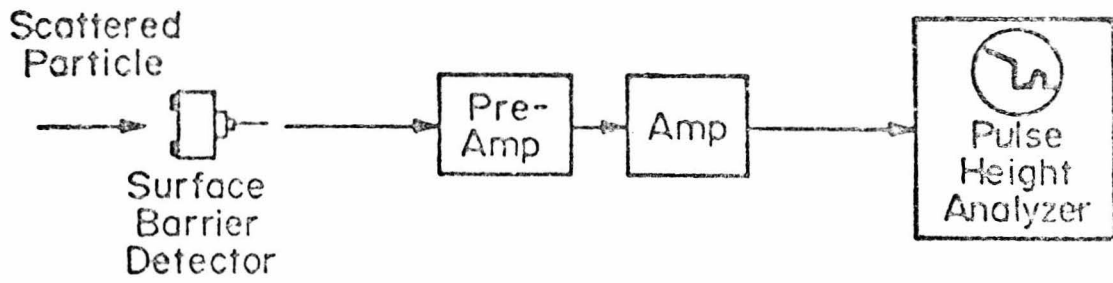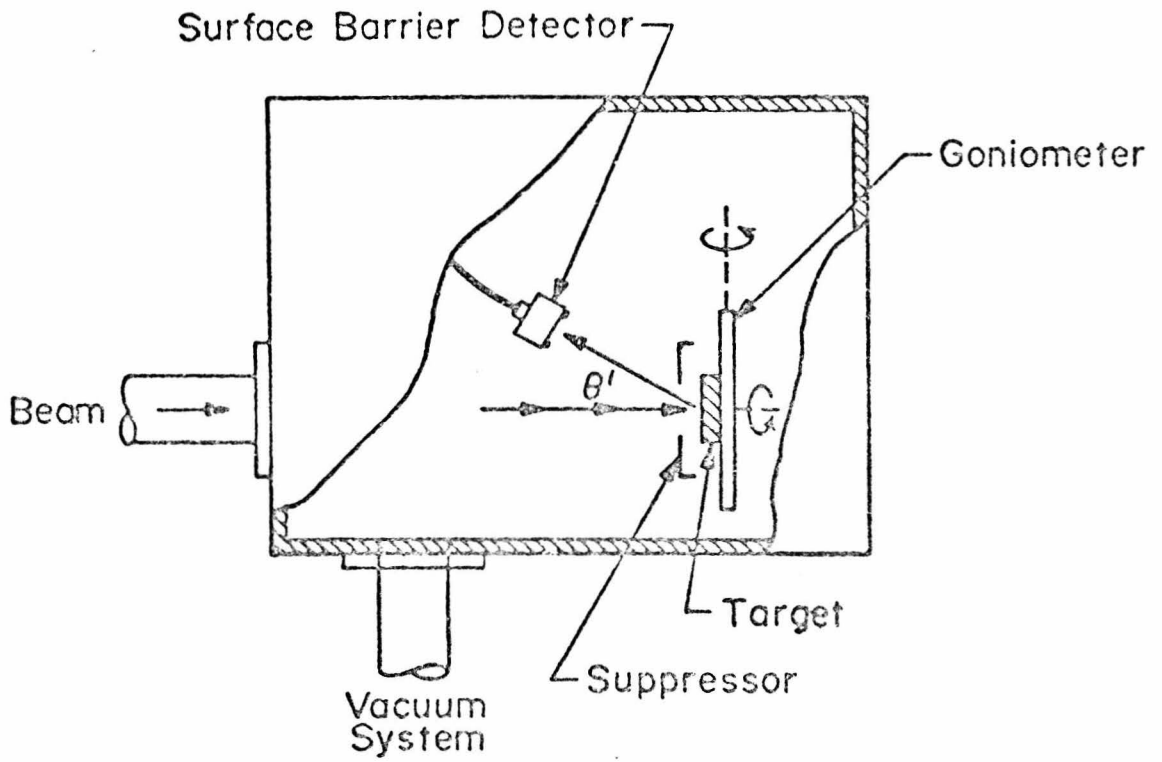
Figure 8

25 mm^2 solid-state silicon-surface-barrier detector placed 10 cm away from the target. The energy spectrum of these particles was obtained using standard electronics and a 400 channel pulse-height analyzer. The energy resolution of the detector was $\leq$ 15 keV FWHM for 1.8 MeV He ions.

B.   Backscattering Energy Spectra

Energy spectra of backscattering particles from an uncovered part of the Si sample were obtained using H and He ions (i) when a low-index direction (<111> or <110>) was well aligned with the incident-beam direction (aligned spectrum) and (ii) when the beam was incident in a random direction (random spectrum). The random spectra on the uncovered central portion of the samples were obtained by tilting the sample off a major axial direction by an angle greater than ten times the critical angle and continuously rotating the crystal about the beam direction.[30] The aligned and random spectra on covered portions of Si samples were obtained by alignment on the uncovered portion of the sample and then translating the beam to the covered portion. From our experimental geometry, translation of the beam by 2 mm causes a change of 0.3×10^{-3} rad in the angle of incidence (a value about 40 times smaller than $\psi_{\frac{1}{2}}$). Measurements on the uncovered sample showed that translation of the beam had no effect on the

aligned components of the spectra.

Figure 9a shows two energy spectra of backscattered 1.8 MeV He$^+$ beam from uncovered Si obtained for aligned and random incidence. Near the surface, the <111> aligned yield was ~ 3% of the random yield. The ratios of aligned to random yield for <111> and <110> orientations were found to be in agreement with previously measured values. [3]

The detailed shapes of the spectra shown above are determined by: (i) the elastic energy loss in the scattering process, (ii) the inelastic energy loss as the particle penetrates the crystal, and (iii) the energy dependence of the scattering cross section. The scattering cross section for incident charged particles in the laboratory system of coordinates (including target recoil) is given by [31,32]

$$\frac{d\sigma(E)}{d\Omega} = \left(\frac{Z_1 Z_2 e^2}{2E_0 \sin^2\theta}\right)^2 \frac{\left[\cos\theta + \sqrt{1-\left(\frac{M_1}{M_2}\sin\theta\right)^2}\right]^2}{\sqrt{1-\left(\frac{M_1}{M_2}\sin\theta\right)^2}} \quad (10)$$

where θ is the laboratory scattering angle, E_0 is the incident particle energy in the laboratory system, Z_1 and M_1 are the atomic number and mass of incident particle, (helium ions in this case) and Z_2 and M_2 are the corresponding values of the target material (Si in this case).

Because of the strong forward-peaking of the Rutherford scattering cross section, only a small fraction typically of the order of 10^{-5} of the helium beam is backscattered from the target. The energy E of the particles scattered at the outer surface of the target, is given by

$$E = K^2 E_o \tag{11}$$

where K^2 is the kinematic recoil factor expressed as[33]

$$K^2 = \left\{ \frac{M_1 \cos\theta}{M_1 + M_2} + \left[\left(\frac{M_1 \cos\theta}{M_1 + M_2} \right)^2 + \frac{M_2 - M_1}{M_1 + M_2} \right]^{\frac{1}{2}} \right\}^2 \tag{12}$$

The energy-to-depth conversion scale for silicon is obtained from stopping power[34] and experimental geometry following the usual procedure (Davies et al.[35]). Representative values for Si stopping power are 31.4, 29.5, 26.2 eV/Å for 0.5, 1.0 and 1.5 MeV He ions, respectively. The depth scale for random incidence is shown in Fig. 9a. For aligned incidence, the depth scale may differ by as much as 15% due to lower stopping power of well-channeled particles in the ingoing trajectory. However, the stopping power depends on the trajectory of the channeled particle and the exact value to be used cannot be specified in general. For dechanneling calculations, we assumed equal aligned and random stopping powers and ob-

tained a depth conversion near the surface of Si of 43.8 eV/$\mathring{A}$ for both random and aligned spectra for 1.8 MeV He$^+$. Recent investigations by Eisen and Bøttiger[36] indicate that this is a reasonable assumption.

Figures 9b and 9c show spectra of Si samples covered with 400$\mathring{A}$ of Au and 3400$\mathring{A}$ of Al, respectively. The presence of a metal film causes a shift in the Si signal to lower energy due to energy losses of the parti-cles as they traverse the film. The signal from Au (shaded portion, Fig. 9b) appears at high energies. The signal for Al (shaded portion, Fig. 9c) appears at lower energies and the trailing edge of the Al signal overlaps the leading edge of the Si signal by 21.6 keV producing an overlap peak.[10] The extraction of the aluminum signal from experimental spectra requires a more elaborate method[10] which has been adopted in the present work. The number of Au and Al atoms per cm^2 was determined by integrating the counts in the two signals; this number was used in comparison with theory, although for simplic-ity in presentation the film thickness is given in ang-stroms by using the conversion factors: 5.9×10^{17} Au atoms/cm^2 and 6.02×10^{17} Al atoms/cm^2 being equivalent to 1000$\mathring{A}$.

As an example, we discuss the energy loss in gold films. Representative values of the stopping cross section of Au for He$^+$ particles at 0.5, 1.0, 1.5 and

Figure 9. Energy spectra for 1.8 MeV He$^+$ backscattered; (a) from an uncovered silicon crystal for random (●) and <111> aligned direction (Δ), (b) from a silicon crystal covered with 400Å of Au for random (●) and <111> aligned direction (Δ). The bottom scale represents the energy (MeV) of the backscattered particles. The top scale in the three figures represents the depth inside the silicon crystal from which the particle has been scattered.
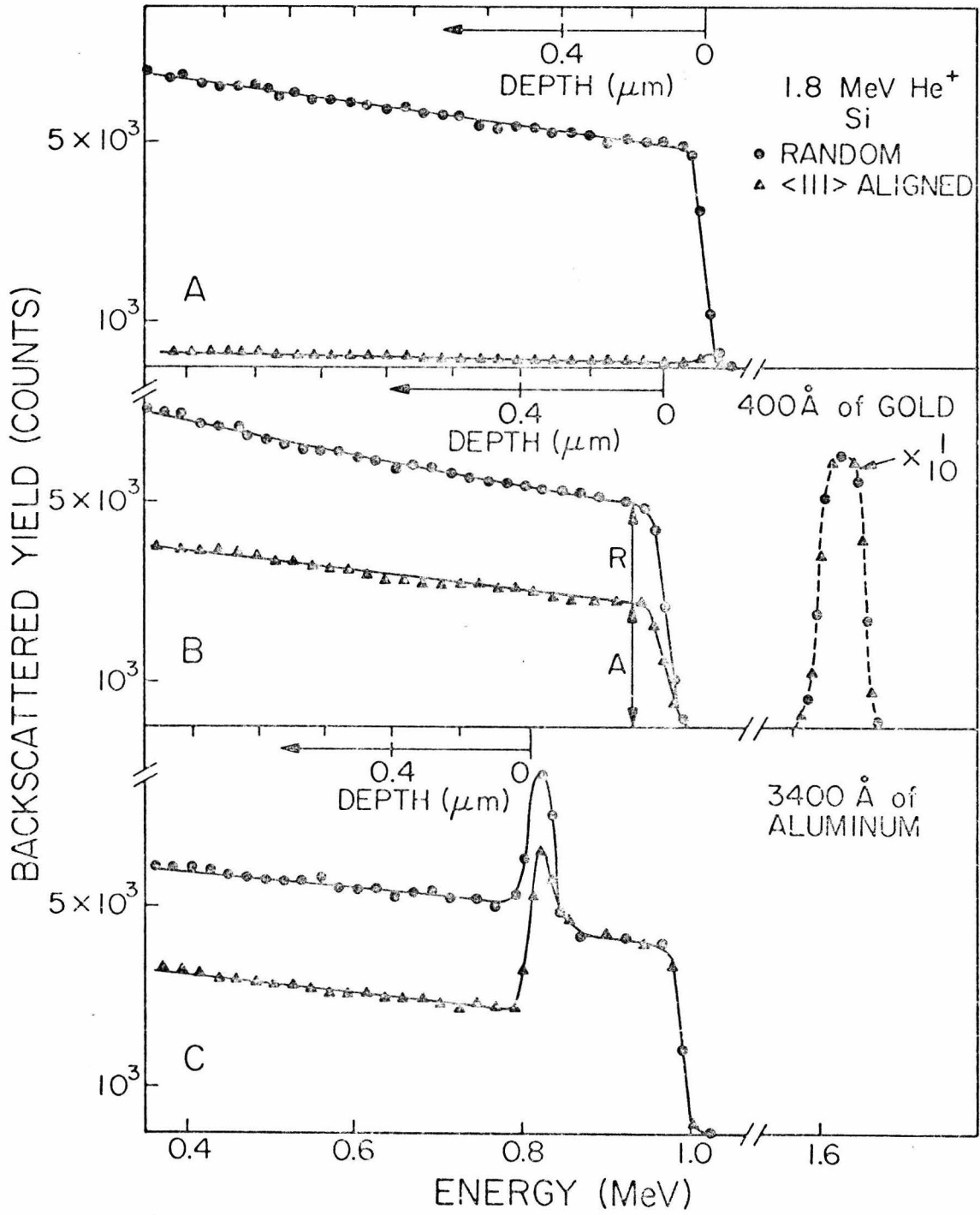
Figure 9

1.8 MeV are 112.0, 128.0, 122.0 and 116.0 x 10^{-5} eV cm^2, respectively. These values were obtained from tables by Ziegler and Chu.[34] The energy loss per angstrom for in and out trajectories of backscattered particles is calculated from the backscattering energy-loss parameter [S] given by[8]

$$[S] \approx K^2 \left.\frac{dE}{dx}\right|_{E_{in}} + \frac{1}{|\cos\theta|} \left.\frac{dE}{dx}\right|_{K^2 E_{in}} \tag{13}$$

Representative values for [S] in Au of bulk density $N_{Au} = 5.9$ x 10^{22} atoms/cm^3 are 140.0, 134.2 and 132.0 eV/Å at 1.5, 1.8 and 2.0 MeV He^+, respectively.

Backscattering measurements were also used to determine the uniformity nature of the film. The uniformity of the films was deduced from absence of any anomalous features in the trailing edge of Au spectra or in the Al-Si overlap peak for film thicknesses greater than 200Å of Au and 600Å of Al, respectively. However for Au films below 150Å thick, the spectra revealed that about 10% of the Si substrate was uncovered.

Channeling measurements were used to evaluate the amorphous nature of the films. When the beam was aligned with <111> or <110> axial directions, no change was found in either the Au or Al signals compared to that obtained with a random incidence. Also planar scans did not re-

veal any orientation effects. These facts indicate that if these films are polycrystalline, the crystallites are either very small or their orientation is sufficiently random to allow the treatment of these films as amorphous structures for channeling experiments.[12]

The minimum yield χ_o = A/R as shown in Fig. 9b was measured experimentally as a function of helium and proton beam energy and layer thickness. These measured minimum yield values were compared with those calculated from the Keil et al. and Meyer treatments of plural scattering.

C. Yield-Profile

Axial as well as planar angular-yield profiles were determined on both covered and uncovered portions of Si samples oriented along <110>, <111> axial directions and the $\{110\}$ planar direction for 1.8 MeV He$^+$ and 0.4 MeV H$^+$. The planar yield profile was obtained in the usual way by scanning across the $\{110\}$ plane (see Fig. 7). It should be stressed here that most of the investigations concerning yield profiles were made using axial yield-profiles. Hence, we describe in detail how the axial yield profiles were obtained.

Two different methods were applied in obtaining these axial-yield profiles. The first method followed the usual procedure of performing an axial scan[12,35]

where the beam is first aligned with either the <110> or
<111> axial directions. Then the normalized yield of
particles backscattered from just below the surface of Si
is obtained as a function of tilt angle. The direction
of the tilt is indicated by a dashed line in Fig. 10
which shows the measured coordinates of the planes and the
<110> axes. The normalization of the yield was made to
that of the random yield, (see Fig. 6). The accuracy of
the scan was checked by comparing both the minimum yield
and the critical-angle value with those obtained in the
previous measurements at 0.4 MeV H^+ and 1.8 MeV He^+.[3]

In the second method, the sample is rotated at
each tilt position thus giving an azimuthally averaged
yield profile. In this method the beam was first aligned
with the < 110> axial direction of an uncovered Si crystal.
Then the < 110> axial direction was made collinear with both
the goniometer axis of rotation and the incident beam dir-
ection using an alignment stage mounted on the goniometer.
This stage has two axes of rotation with respect to the
incident-beam direction. It could be tilted so that the
axial direction of the crystal resting on it could be
brought in line with the axis of rotation of the gonio-
meter. The normalized yield of the particles backscattered
from just below the surface of Si was obtained as a func-
tion of tilt angle by continuously rotating the Si crystal
about the beam direction (see Fig. 10). As before, the

Figure 10. Dashed line shows the tilt direction along which the normal axial angular-yield profile is obtained. The dash-dot lines represent the rotation direction along which an azimuthally averaged probability curve is obtained for various tilt angles. Solid lines are the Si crystallographic planes.
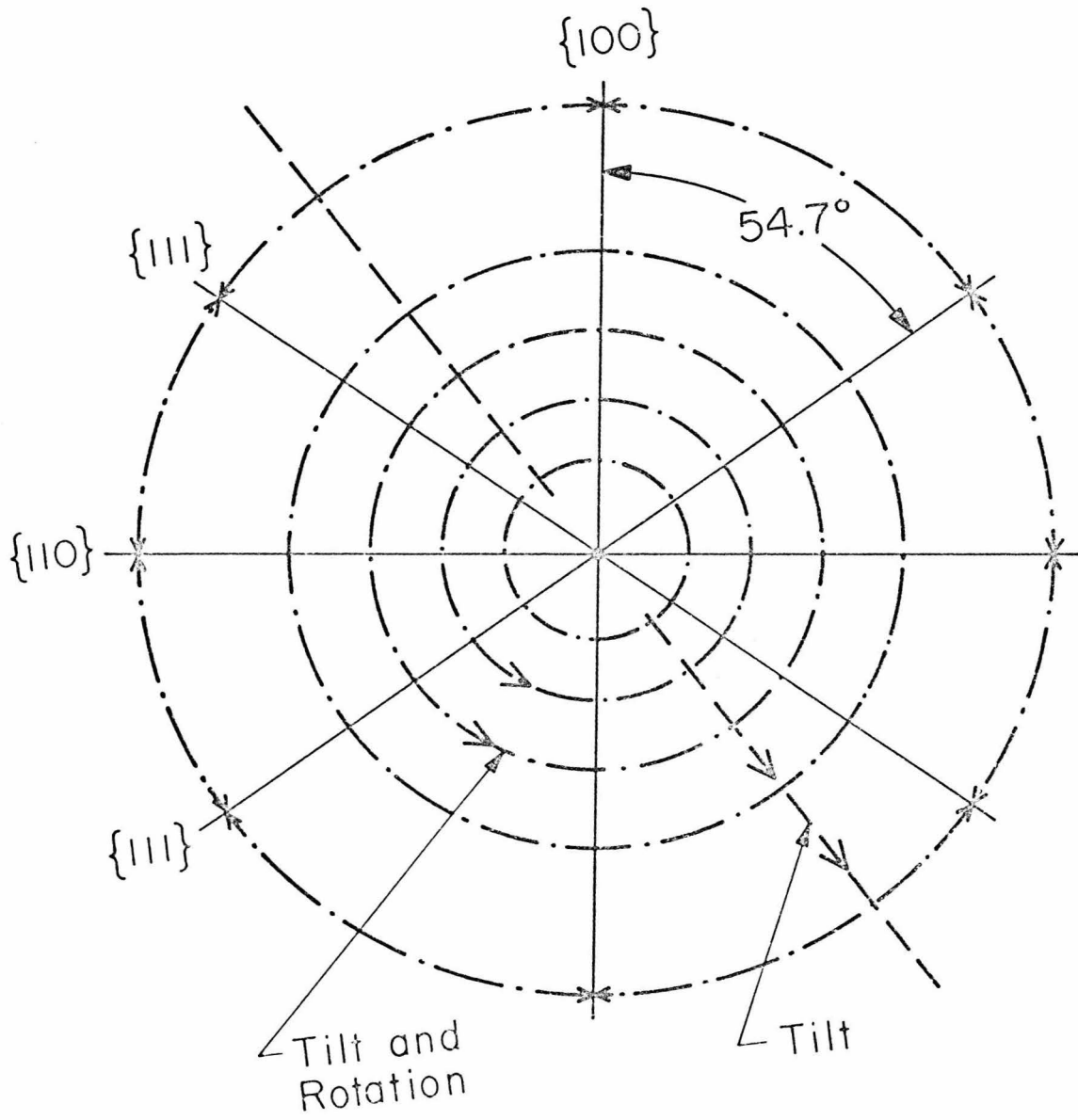
Figure 10

normalization of the backscattered yield was made to that of the random yield.

The scans obtained by those two above procedures (see Fig. 11), coincide for both zero- and large-tilt angles. However, for tilt-angles in between the critical angle $\psi_{\frac{1}{2}}$ and $\simeq 3\psi_{\frac{1}{2}}$, the angular-yield profile obtained in the second method is lower than that in the first procedure. This lower yield is due to the influence of planar channels during azimuthal averaging by rotation of the sample around the crystal axes. The influence of planar channels can be inferred from Fig. 12 which shows orientation dependence of characteristic X-rays produced in crystals by positive-ion bombardment. This figure furnished by J. Khan[37] shows contours of copper L-shell X-ray yields centered upon a [011] direction on bombardment with 70 KeV protons.

Figure 11. Upper: Number of particles per rad. scattered at an angle θ from the initial direction for 0.4 MeV H^+ and 1.8 MeV He^+ after traversing a reduced thickness m = 0.2 (100$\overset{o}{A}$ Au, H^+), m = 1.0 (500$\overset{o}{A}$ Au, H^+) (solid lines), and m = 0.6 (264$\overset{o}{A}$ Au, He^+), m = 2.5 (1100$\overset{o}{A}$ Au, He^+) (dashed lines) according to Meyer's theory.

Lower: Experimental axial scan obtained by "tilt" only (solid line) and azimuthally averaged experimental axial scan obtained by "tilt and rotation" (dotted line) for 1.8 MeV He^+ incident along <110> Si axis. Step-function approximation is shown as a vertical dashed line.
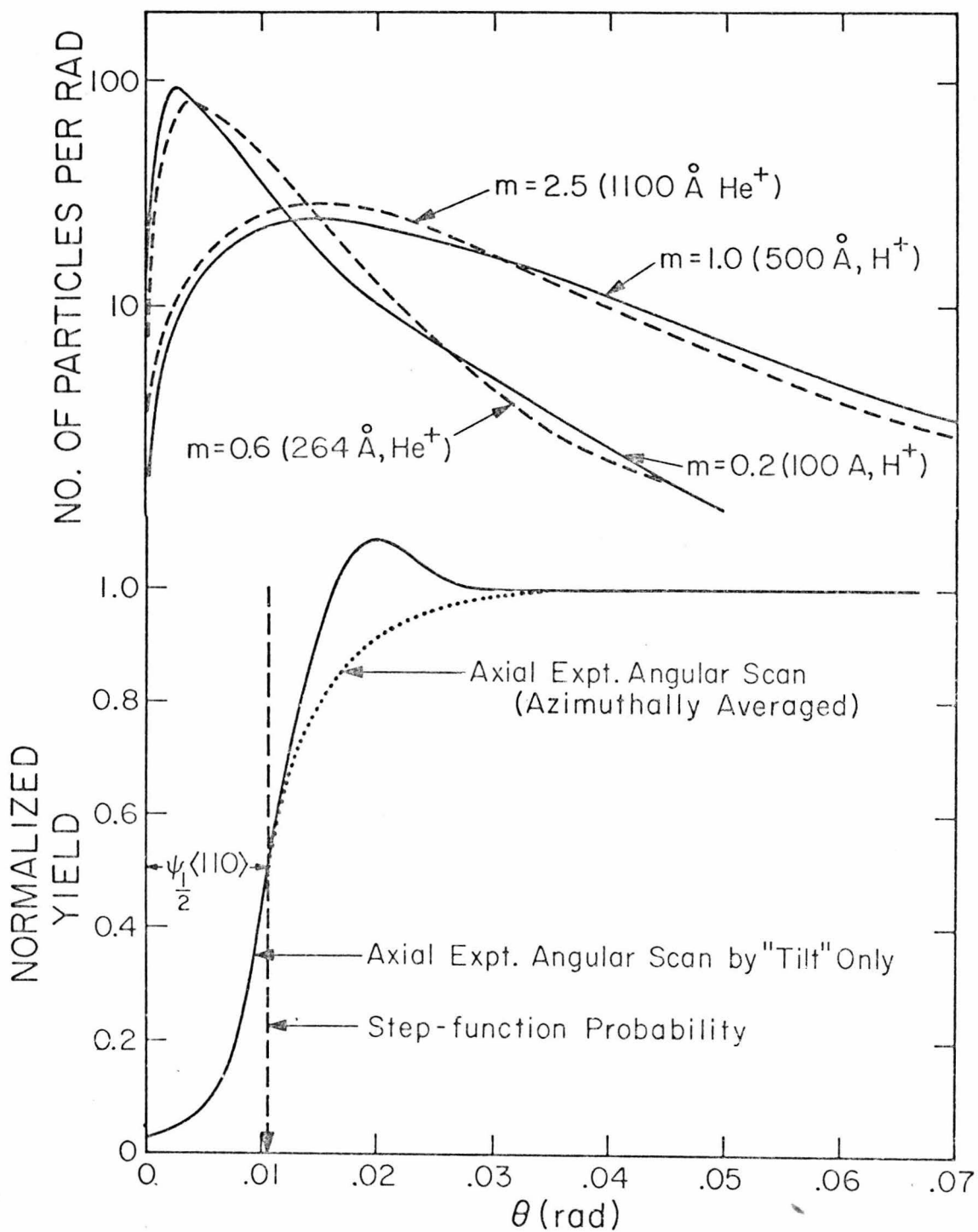
Figure 11

Figure 12. Copper L-shell X-ray yield contour in the region of the (011) direction showing intersecting planes, standard sweeps (dashed lines), and yield value extremes (starred points). The incident proton energy is 70 keV.
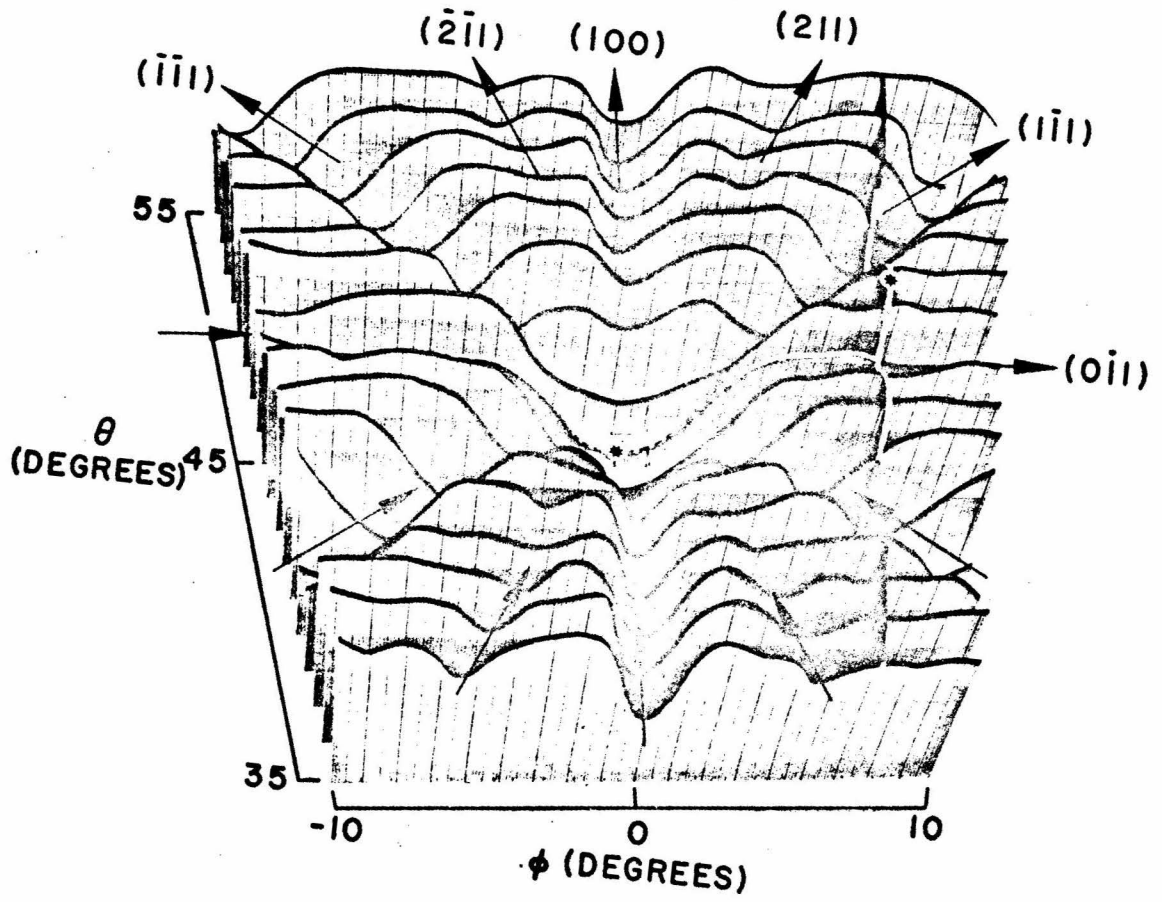
Figure 12

III.   CALCULATION PROCEDURE

In this work we have made channeling measurements by backscattering techniques with MeV He and H ions to determine minimum yields, angular-yield profiles, and aligned yields versus depth in silicon samples covered with Au and Al films. The approach was to use various film thicknesses and beam energy to investigate experimentally the scattering regime where both the Meyer and Keil et al., treatments of plural scattering gave comparable distributions and where the distributions differed. In this section we will indicate how the experimentally measured parameters furnish information on the scattering of particles in metal films. Further we give methods of estimating minimum yields from crystals overlaid with amorphous films.

An estimate for axial minimum yield for an un-covered crystal is given by

$$\chi_o = \pi (r_{min})^2 \, Nd \qquad (14)$$

In this formula we note that all the particles that strike within an area $\pi (r_{min})^2$ of each surface atom are to be associated with the random yield. Here r_{min} is the minimum impact parameter for a channeled particle with the row.

If we let N be the atomic density and d the lattice spacing along the direction of travel, then (Nd) is surface density of atoms along the direction of travel. Hence the surface area to be associated with the minimum yield is that given in Eq. 14. Normally the axial minimum yield for 2.0 MeV He^+ impinging on Si single crystal at room temperature is approximately 3% of the random yield.

The planar minimum yield is defined as[26]

$$(\chi_o)_p = \frac{2Y_{min}}{d_p} \tag{15}$$

where Y_{min} is the minimum impact parameter for a channeled particle with the plane, and d_p being the separation between neighboring planes. In the Lindhard's static lattice continuum string approximation for the crystal potential,[26] r_{min} in axial and Y_{min} in planar channeling are assigned a value equal to the Thomas-Fermi screening distance 'a_{TF}'.

The presence of an amorphous layer on a silicon crystal results in an increase in the aligned yield of energy spectra of backscattered particles. The computation of the increase in the aligned yield requires knowledge of the following:

1. The angular distribution $f(\theta)$ of the analyzing beam due to scattering experienced by particles traversing the layer.

2. The probability $P_z(\theta)$ that a particle entering with an angle θ with a given direction of the crystal moves in a random trajectory at a certain depth z (dechanneling probability).

3. The effect of the crystal potential on the angular dispersion of the beam (transmission factor).

The dechanneled fraction at a depth z is given by

$$\chi(z) = \int_0^\infty f(\theta) 2\pi\theta \, P_z(\theta) d\theta \tag{16}$$

where $f(\theta)$ is the differential distribution of the impinging particles after traversing the amorphous layer and the crystal surface.

1. Differential Distribution

The scattering-particle distribution in the amorphous layer was based on two treatments of plural scattering. The first treatment of plural scattering is that of Keil et al. This utilizes the Moliére cross section which is smaller than the Thomas-Fermi cross section and gives a strong forward-peaked distribution of the particles. As a result, a large fraction of the beam passes through the film undeflected particularly for low values of 'reduced thickness' m. In the small angle approximation the differential cross section based on the form of Moliére may

be represented by[16]

$$d\sigma = \left[\frac{2Z_1 Z_2 e^2}{pv}\right]^2 \frac{2\pi\theta \, d\theta}{(\theta^2 + \theta_a^2)^2} \tag{17}$$

where Z_2 is the atomic number of the scattering centers, Z_1, p and v being the atomic number, momentum and velocity respectively of the scattered particle in the center of mass system of coordinates. The screening angle θ_a describes the screening of the nuclear charge by the atomic electrons and is defined as[16]

$$\theta_a = \frac{\hbar}{pa_{TF}} \left[1.13 + 3.76 \left(\frac{Z_1 Z_2}{137\beta}\right)^2\right]^{\frac{1}{2}} \tag{18}$$

where $\beta = v/C$ with $C = 3 \times 10^{10}$ cm/sec. For 1.8 MeV He ions incident on Au and Al the values of θ_a are 8.7×10^{-2} and 8.5×10^{-2} respectively.

The scattered-particle angular distribution integrated from θ outwards for a reduced thickness m is given as $\hat{G}*(m,\theta)$. This gives the fraction of the particles scattered beyond θ from $\hat{G}*(m,\theta) = \int_\theta^\infty f^K(m,\theta)d\Omega$. Values of $\hat{G}*(m,\theta)$ are given in Table 2 of Keil et al.[15] Here, note that $f^K(m,\theta)$ corresponds to $G*(m,\theta)$ in Keil tables.

The second treatment of plural scattering is that

given by Meyer and this uses the Thomas-Fermi cross section. Meyer gives the scattered-particle distribution $F(m,\tilde{\theta})$ as a function of m and reduced angle $\tilde{\theta}$ defined as [17]

$$\tilde{\theta} = \frac{\varepsilon}{2} \left[\left(\frac{m_1 + m_2}{m_2} \right) \right] \theta \tag{19}$$

Here, ε is the reduced energy (a dimensionless unit) introduced by Lindhard et al. [26] A more elaborate description of Meyer's treatment of plural scattering and as applied to this work is presented in the Appendix.

Figure 11 shows the calculated differential-scattering distributions $2\pi\theta f(\theta)$ which give the number of particles scattered by an amorphous layer at an angle θ from the initial direction for He and H ions. These differential distributions are obtained from the angular distributions tabulated by Meyer* for:
$m = 0.6(264\overset{o}{A}$ Au, 1.8 MeV He[+]$)$, $m = 2.5(1100\overset{o}{A}$ Au, 1.8 MeV He[+]$)$, $m = 0.2(100\overset{o}{A}$ Au, 0.4 MeV H^{+}$)$ and $m = 1.0$ $(500\overset{o}{A}$ Au, 0.4 MeV He[+]$)$.

2. Dechanneling Probability

There are several methods of determining the probability $P(\theta)$ that a particle entering a crystal with an

---

*K.B. Winterbon has corrected in a private communication, most of the computational errors which appeared in Meyer's tables published (1971).

angle θ with a given crystallographic orientation moves in a random trajectory at a certain depth. The first method treats as dechanneled all particles which have an angle with the channel axis greater than $\psi_{\frac{1}{2}}$. This procedure, usually called the step-function approximation, assumes that a particle is in the random component of the beam (dechanneling probability equal to one) when its angle with the channel axis is greater than $\psi_{\frac{1}{2}}$, or equivalently when its transverse energy $E_\perp$ is greater than $E\psi_{\frac{1}{2}}^2$. A particle is in the aligned component (dechanneling probability equal to zero) when its angle with the channel axis is less than $\psi_{\frac{1}{2}}$, or equivalently when the transverse energy $E_\perp$ is less than $E\psi_{\frac{1}{2}}^2$. The step-function approximation is shown as a vertical dashed line in the lower part of Fig. 11.

By using the step-function approximation, the aligned yield near the crystal surface, i.e., the minimum yield χ_0, is given directly by the integral of the initial angular distribution $f(\theta)$ of the particles just beneath the crystal surface, for angle values greater than $\psi_{\frac{1}{2}}$. The minimum yield, χ_0 is given by:

$$\chi_0 = \int_0^\infty f(\theta) P(\theta) 2\pi\theta d\theta \simeq \int_{\psi_{\frac{1}{2}}}^\infty f(\theta) 2\pi\theta d\theta \qquad (20)$$

since the dechanneling probability $P(\theta)$ satisfies the

equality below:

$$P(\theta) = \begin{cases} 1 & \text{for} \quad \theta \geq \psi_{\frac{1}{2}} \\ 0 & \text{for} \quad \theta \leq \psi_{\frac{1}{2}} \end{cases}$$

It should be remarked here that both Keil and Meyer theories give data in reduced energies and angles. Therefore, it is necessary to define the reduced critical angles θ_K and $\tilde{\theta}_c$ by

$$\theta_K = \frac{\psi_{\frac{1}{2}}}{\theta_a} \tag{21}$$

where θ_a is the screening angle given by Eq. 18 and

$$\tilde{\theta}_c = N(E, Z_1, Z_2) \psi_{\frac{1}{2}} \tag{22}$$

where $N(E, Z_1, Z_2) = (a_{TF} E / 2 Z_1 Z_2 e^2)$ is a normalizing factor in Meyer's angular distributions. Equation 22 is derived in the Appendix. As a result the minimum yield from crystal overlaid with layers is given by:

$$(\chi_o)_{\text{Keil et al.}} = \hat{G}^*(m, \theta_K) = \int_{\theta_K}^{\infty} f^K(m, \theta) 2\pi\theta d\theta \tag{23}$$

and

$$(\chi_o)_{Meyer} = \int_{\tilde{\theta}_c}^{\infty} f(m,\tilde{\theta})\, 2\pi\tilde{\theta}d\tilde{\theta} \qquad (24)$$

The second method of finding the dechanneling prob-
ability $P(\theta)$ replaces the step-function approximation with
experimentally determined axial angular-yield profiles
on an uncovered Si crystal at different depths. We used
two different procedures to measure the angular yield
profiles: (a) axial scans, and (b) azimuthally-averaged
scans.

(a) The first procedure for determining one of the profiles
at a certain depth in Si followed the usual technique [35]
of performing an axial scan where the beam is first align-
ed with either <110> or <111> axial directions and then
the normalized yield of backscattered particles is ob-
tained as a function of tilt angle. The resulting yield
profile is shown in (solid line) in the lower part of
Fig. 11. This profile is taken as an experimental de-
channeling probability at a certain depth in the crystal.
Alternatively, a number of dechanneling probability curves
at different depths in the crystal have been obtained from
experimental energy spectra recorded for He and H ions at
different incident tilt angles, (see Fig. 5).

(b) The other procedure for determining an axial angular-
yield profile involved the rotation of the sample at each

tilt position thus giving an azimuthally-averaged angular-yield profile (described in Section II.C). The normalized yield of the backscattered particles from just below the surface of Si was obtained as a function of tilt angle by continuously rotating the Si crystal about the beam direction. The resulting azimuthally-averaged angular-yield profile is shown (dotted line) in the lower part of Fig. 11.

The two experimental axial angular-yield profiles discussed above were used in calculating the aligned yield from Si single crystal covered with metal layers. In particular, calculation of the minimum yield χ_o utilized both the experimental angular-yield profile obtained near the surface of the uncovered crystal and the calculated differential-scattering distribution of the particles in the film. In this method the minimum yield is obtained by convolution of the initial scattering distribution in the amorphous layer with the experimental normalized angular-yield profile; i.e. the yield profile is taken as a weighting function. This weighting function is first multiplied by the scattering distribution and then integrated over all angles to give the minimum yield χ_o. It must be pointed out here that since the experimental axial angular-yield profiles include the scattering through the crystal surface, then the particle-scattering distribution considered is that due only to amorphous layer.

3. Transmission Factor

The scattering in the first few crystal layers (transmission factor) always has the effect of increasing the particle transverse energy and hence its transverse momentum by an amount which depends on the point of entry of the particle. The change in transverse energy due to surface transmission is given by $U(r) - U(r_o)$ where $U(r)$ and $U(r_o)$ are row potentials[26] at distance r and in the middle of the channel respectively. In calculating axial minimum yield χ_o using the step-function approximation, we have as an approximation neglected the contribution of the transmission factor to the angular distributions of the particles.

To test the validity of this approximation, a numerical calculation has been carried out by E. Rimini[38] to determine the transmission factor contributions to the angular distributions of particles after traversing $88\overset{o}{A}$ of Au. Figure 13 shows the normalized integrated angular distribution for 1.8 MeV He[+] due to (1) angular spread of the beam, (2) the scattering due to the lattice potential (transmission factor), (3) the angular spreading produced by $88\overset{o}{A}$ Au layer on Si crystal using Meyer treatment and (4) the resulting distribution with (2) and (3) taken into account. The resulting integrated angular distribution differs by about 20% from that obtained with the layer

Figure 13. Normalized integrated angular distribution
for: (1) experimental angular spread of 1.8 MeV
He beam; (2) angular distribution due to scatter-
ing of the beam by lattice potential (transmission
factor); (3) angular distribution produced by
88Å of Au covering the Si crystal surface accord-
ing to Meyer's theory, and (4) particle distri-
bution including cases (2) and (3) above.
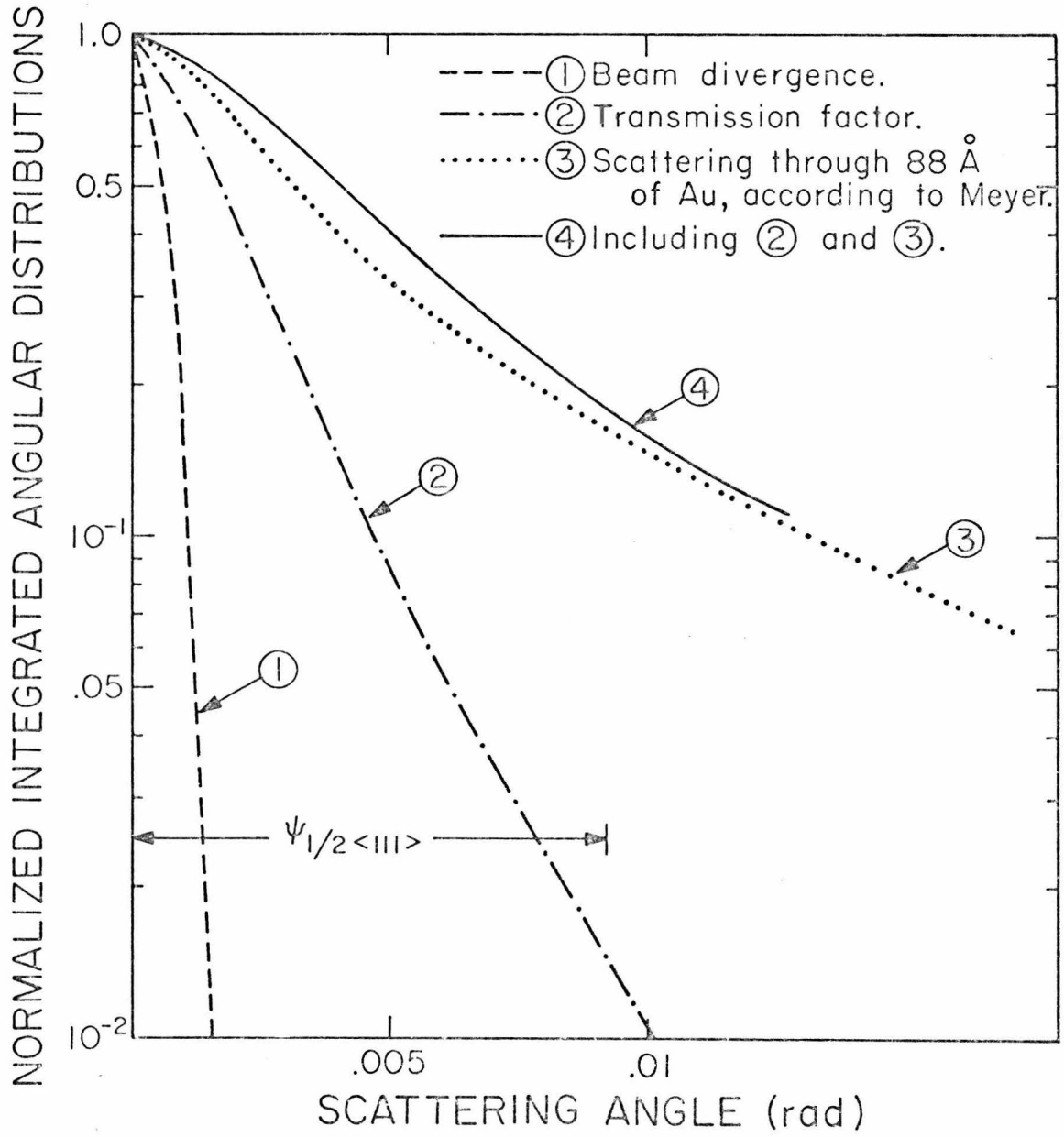
Figure 13

contribution alone for small angles of scattering ($\sim 1/10$ of $\psi_{\frac{1}{2}}$), while the two coincide within 5-10% for angles comparable or greater than $\psi_{\frac{1}{2}}$. Of course with increasing layer thickness the contribution of the transmission factor to the axial minimum yield becomes more and more negligible. As an example, at small scattering angle this contribution falls from 20% for 100$\overset{o}{A}$ to 5% for 600$\overset{o}{A}$ of Au respectively. It should be pointed out that in estimating the planar minimum yield values the transmission factor effects cannot be neglected, (see Fig. 7).

The computation of minimum yield χ_o using the convolution procedure takes the transmission factor contribution into account. The experimental angular-yield profiles whether azimuthally-averaged or not, obtained near the surface of the crystal include the scattering through the crystal surface. Thus the differential distributions required in calculating planar or axial minimum yields are those due only to amorphous layers.

IV. RESULTS AND DISCUSSION

A. Axial Minimum Yield

1. Step-Function Approximation

In this section experimental axial minimum yield values are compared to those calculated by applying the step-function approximation to the differential distributions based on Keil and Meyer treatments of plural scattering. The minimum yield values are presented as functions of film thickness and beam energy. By varying these experimental parameters, one explores the validity and range of applicability of these two theories of plural scattering. Also the corresponding changes in the minimum yield values furnish information on the channeling behavior of the analyzing beam in the crystal.

Using He^+ and H^+ ions we have investigated the dependence of minimum yield values on film thickness. Shown in Fig. 14 are the minimum yield values for 1.8 MeV He^+ incident on <111>- and <110>-oriented Si versus thickness of Au film calculated by integrating the differential distribution outwards from the critical angle $\psi_{\frac{1}{2}}$. In this step-function approximation approach the transmission factor is neglected. The solid lines in the figure represent the values calculated from Meyer and the dashed lines are the values from Keil treatment of plural scat-

Figure 14. Minimum yield χ_o at the silicon surface for 1.8 MeV He$^+$ impinging along the <110> (▲) and <111> (Δ) axes of Si covered with different thicknesses of Au. The lines show the calculated values using the step-function approximation, and the Meyer distribution (solid line), and Keil et al. distribution (dashed line).
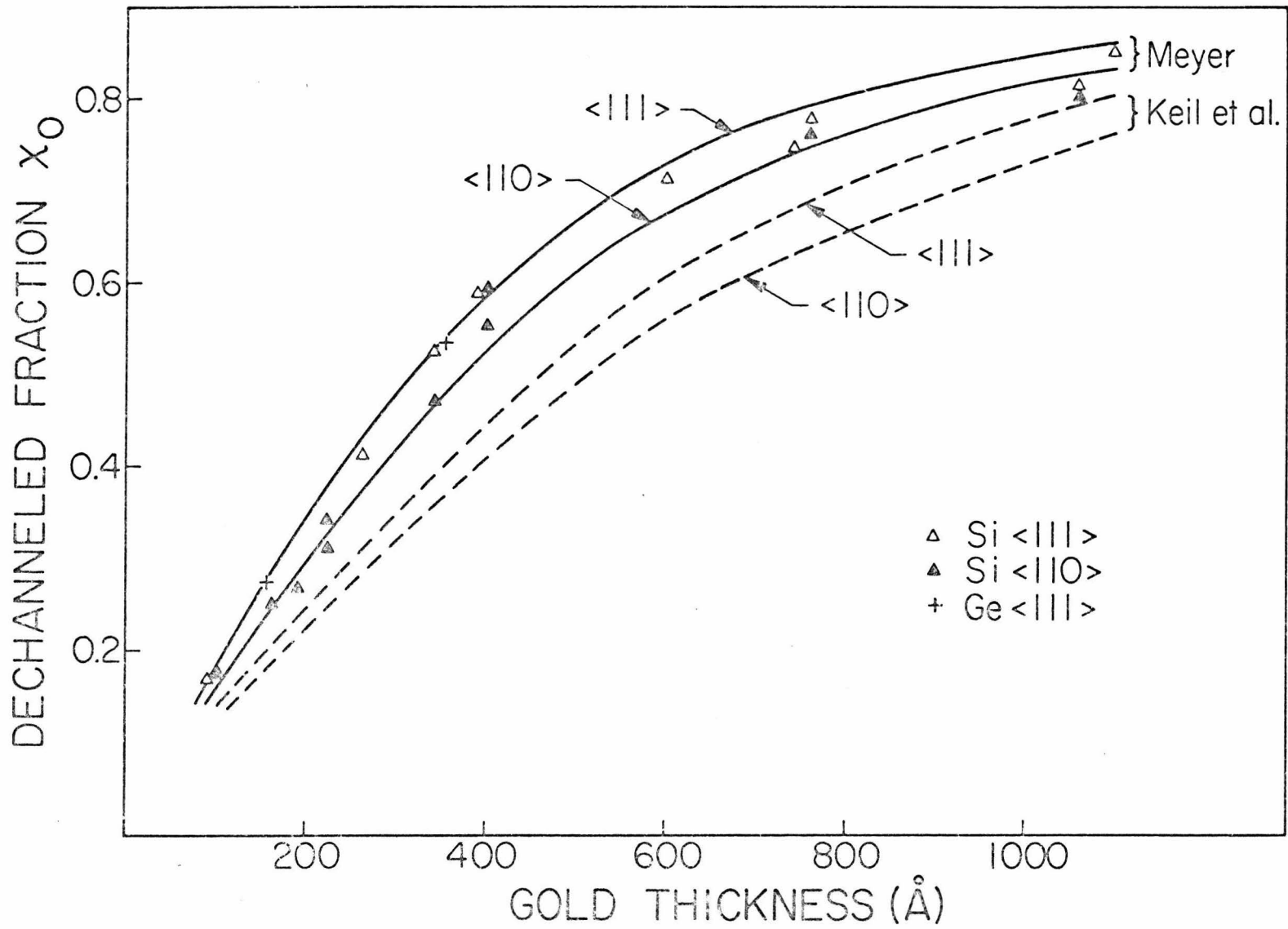
Figure 14

tering. In these calculations we used experimental values of $\psi_{\frac{1}{2}}$ for particle energies after traversing the film thickness. The experimental points follow the trend of both theories but agree in absolute magnitude more closely with Meyer treatment. Two points (+) for Ge <111> are included, since $\psi_{\frac{1}{2}}$ for this case lies between the Si <110> <111> values. These points are also closer to Meyer theory of plural scattering.

Minimum-yield values are shown in Fig. 15 as a function of Au film thickness for 400 keV He and H ions incident on <111>-oriented Si. For He ions, the reduced thickness m = 1.0 of Au corresponds to 440Å. The upper solid and dashed lines correspond to minimum yields calculated from Meyer distributions for He and H ions, respectively. The lower set of curves corresponds to those using Keil et al. distributions at the same energy. It is very evident that the experimental minimum yield values follow those calculated from the Meyer distributions very closely.

The minimum yield just beneath the silicon surface is explored further as a function of He^+ and H^+ beam energies. This investigation allows one to study the validity and consistency of the analytical procedure utilized over a wide range of energy. Figures 16a and 16b show the minimum yield dependence on energy for different gold film thicknesses. The solid curves are obtained by

Figure 15. Minimum yield χ_o at the Si surface for 0.4

MeV H^+ (●) and 0.4 MeV He^+ (Δ) incident along

<111> axis of Si covered with various m values

(the reduced gold thickness). The solid and

dashed lines are calculated by using step-function

approximation and the Meyer (upper) and Keil et al.
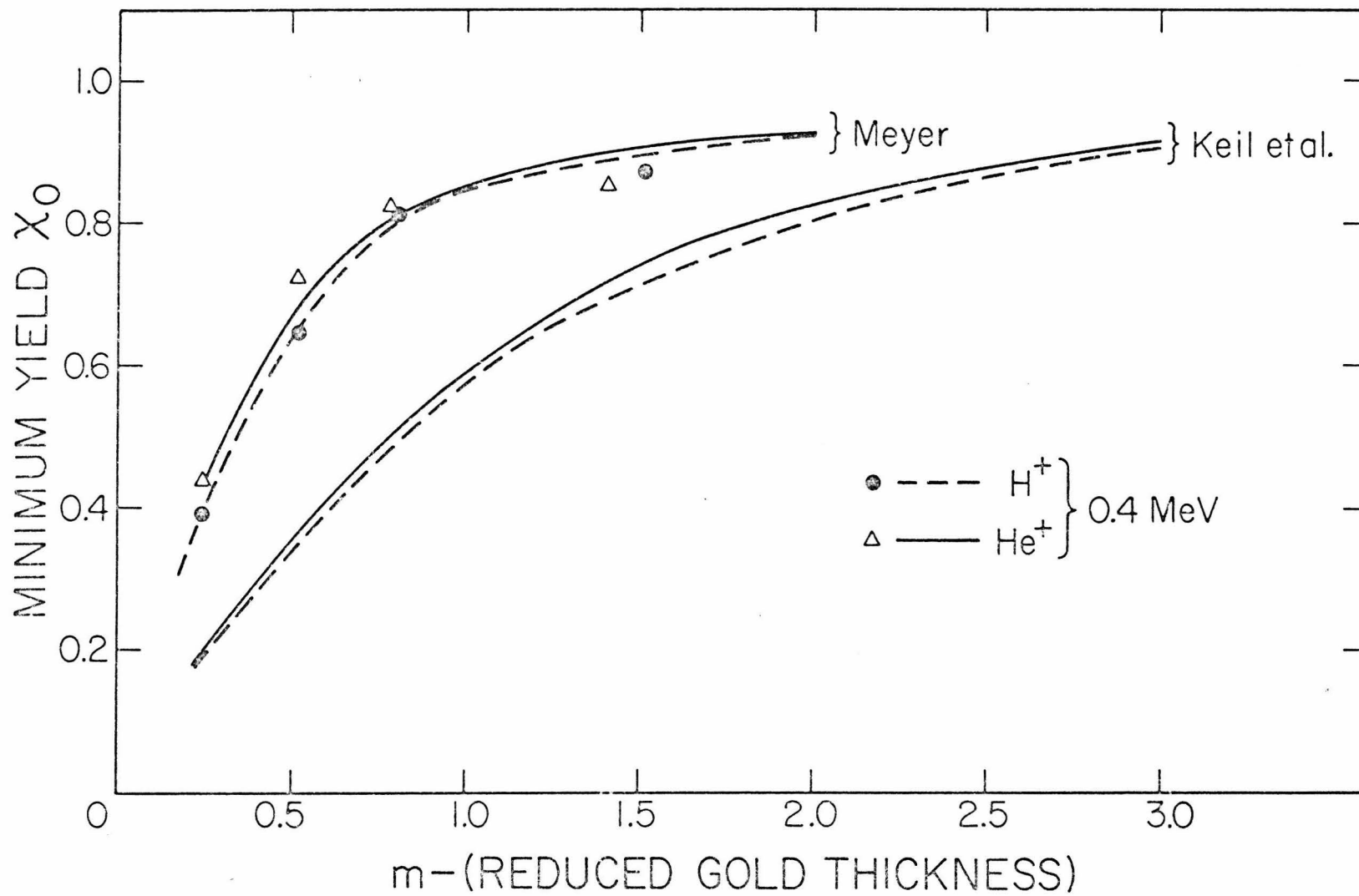
(lower) treatment of plural scattering.

Figure 15

Figure 16. Minimum yield χ_o at the silicon surface as a function of (a) He^+ energy and (b) H^+ energy incident along the <111> axis of Si covered with different thicknesses of Au. The lines are calculated by using Meyer distribution and step-function approximation.
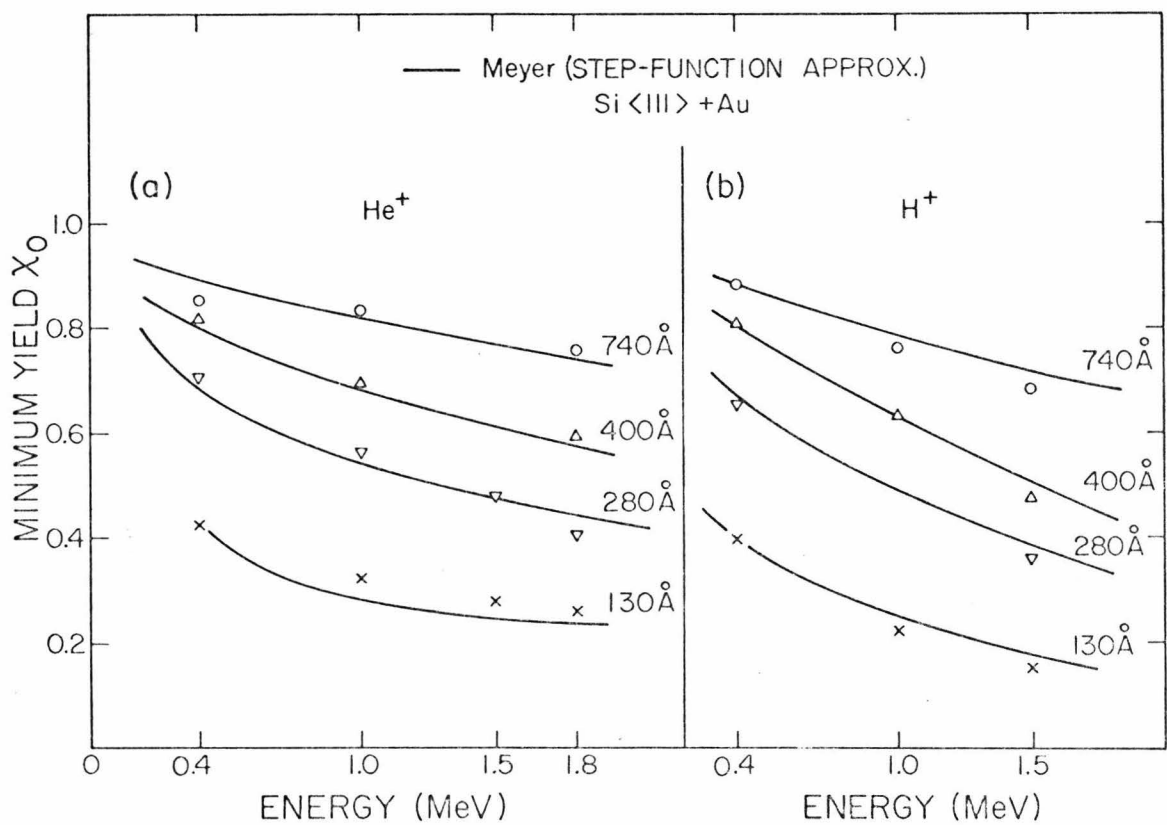
Figure 16

application of the step-function approximation to the scattering distribution in the Meyer theory. The decreases of the minimum yield with increasing energy can be explained on the basis of particle-scattering distribution in the film and the channeling mechanism (i.e. critical angle $\psi_{\frac{1}{2}}$). As the beam energy increases, the critical angle $\psi_{\frac{1}{2}}$ decreases[26] as $E^{-\frac{1}{2}}$ (see Eqs. 5 and 6). But in this case the angular width of the scattering profile bears an inverse relationship[17] with energy i.e., the scattered-particle distribution becomes narrower as the energy increases. This results in a decrease in minimum-yield value χ_O with energy. The experimental minimum-yield values (χ_O) are in accord with the theoretical prediction except for the thinnest gold films thickness. For 130$\overset{\circ}{A}$ Au films the experimental values for He^+ are slightly above the theoretical curve and below the theoretical curve for H^+. In any case, the difference between theory and experiment is within 5%.

Using 1.8 MeV He^+, we have also investigated the minimum yield dependence on aluminum film thickness. Shown in Fig. 17 are the experimental and calculated minimum yield values for <110> and <111> orientations versus Al thickness. The calculations utilize Meyer and Keil et al. angular distributions and the step-function approximation. The solid lines represent the values calculated from Meyer and the dashed lines the values from

Figure 17. Minimum yield χ_O for 1.8 MeV He[+] impinging along the <110> (■) and <111> (□) axes of Si crystals covered with different thickness of Al. The solid lines represent the values calculated from Meyer and the dashed lines, the values from Keil et al.
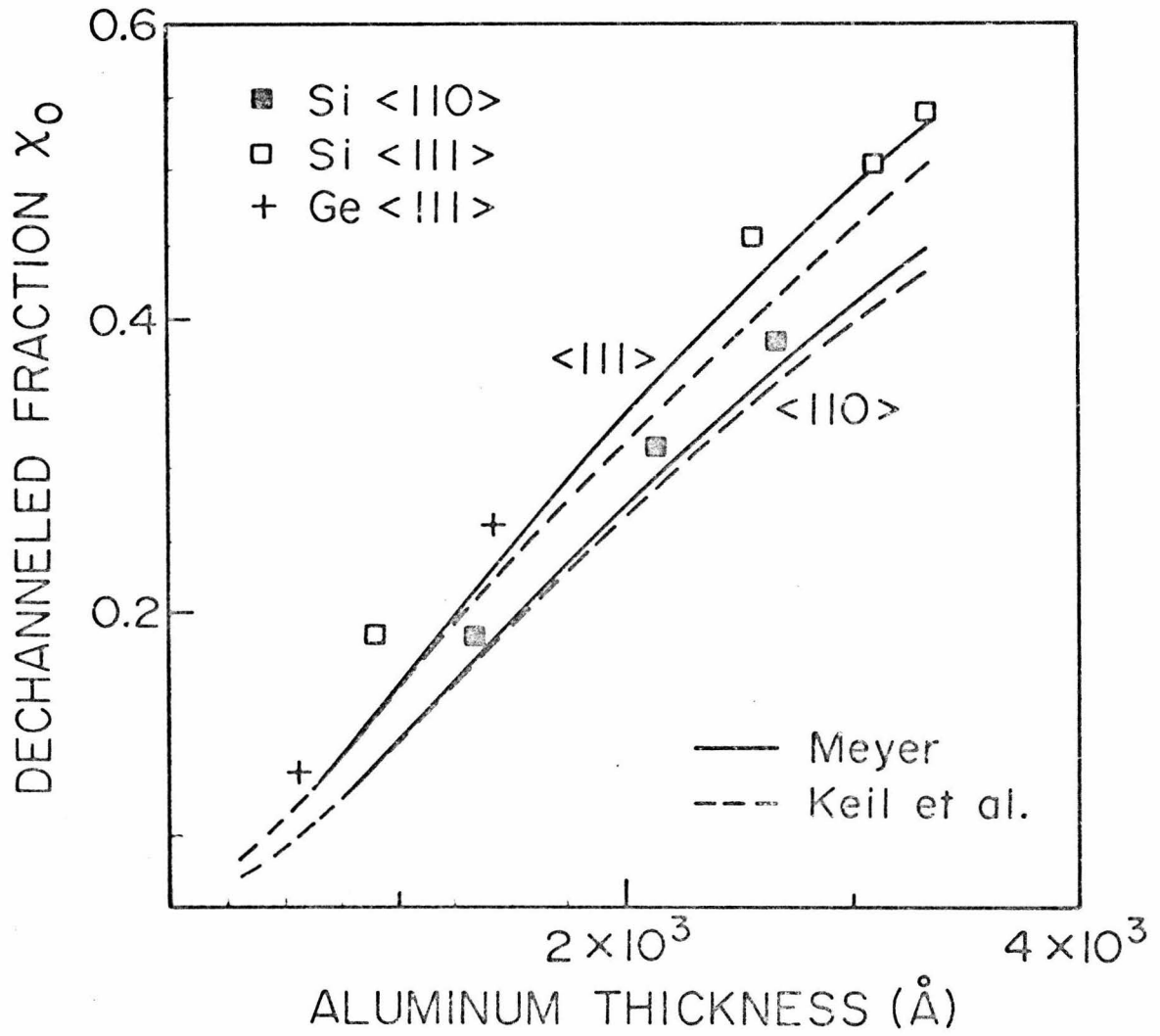
Figure 17

Keil et al. In this case, the difference in the two cal-
culations is not great. This is a consequence of the large
number of scattering centers (m > 10) in which the effect
of the differences in the potential is not felt. Hence
the two treatments yield nearly the same result. It is
interesting to note that the difference in the calculated
values of the minimum yield between <110> and <111>
orientations is much greater than the difference between
minimum yield values predicted by the two treatments.
The measured values agree within 10% with theory for both
crystal orientations and for film thicknesses greater
than 1000Å.

2. Azimuthally-Averaged Angular Yield Profile

It is interesting to test the sensitivity of the
calculated minimum yield values on the adopted dechannel-
ing criteria. Our investigation of minimum yield values
reveals that the Meyer treatment of plural scattering is
more appropriate than Keil's to describe the interaction
of incoming beam with the metal film. A comparison is
then made in this section between experimental minimum-
yield values with those calculated by applying different
dechanneling criteria namely (i) the step-function approxi-
mation, (ii) the axial angular-yield profile obtained by
tilt only, and (iii) the azimuthally averaged angular-
yield profile. These three criteria are illustrated in

the lower part of Fig. 11.

Figure 18 shows both experimental and calculated minimum yield values for <110>- and <111>-oriented Si at 1.8 MeV He$^+$ and 0.4 MeV H$^+$ respectively. The experimental values for Au films are shown as solid and open triangles and for Al films as (x). The minimum yield values obtained by convolution of the differential distributions of He and H ions in the Au film and the angular yield profiles obtained by tilt only for 1.8 MeV He$^+$ and 0.4 MeV H$^+$ on uncovered Si are shown in solid curves. For He ions, the calculated minimum yield values are about 5% higher than the experimental values for low and high m values. However, for intermediate m values, the minimum yield values lie about 10% higher than the experimental ones. In the case of 0.4 MeV H$^+$ the calculated yield values are higher than the experimental values by about 7% for the entire range of gold thicknesses.

On the other hand, when the azimuthally averaged angular-yield profile (shown in the dotted line in lower part of Fig. 11) is convoluted with the calculated differential-scattering distribution of He ions, the resulting minimum-yield values (shown by the dotted curves in Fig. 18) agree fairly well with the experimental data for the entire film thickness. This suggests that the most accurate angular yield profile to use in convolution procedure is the curve obtained by tilting and rotation. The curve

Figure 18. Minimum yield χ_o at the Si surface for 0.4
MeV H^+ and 1.8 MeV He^+ incident, respectively,
along the <111> (Δ) and <110> ($\blacktriangle$) axes of Si
covered with different thicknesses of Au. The
lines show the calculated values using the Meyer
distribution and (i) the step-function approxi-
mation (dashed line), (ii) the normal axial
angular-yield profile (solid line), and (iii)
the azimuthally averaged angular-yield profile
(dotted line). Shown in the insert is the
minimum yield χ_o at the Si surface for 1.8 MeV He^+
incident along the <111> axis (x) of Si covered
with different thicknesses of Al. The curves
carry the same meaning as in the case of Au above.
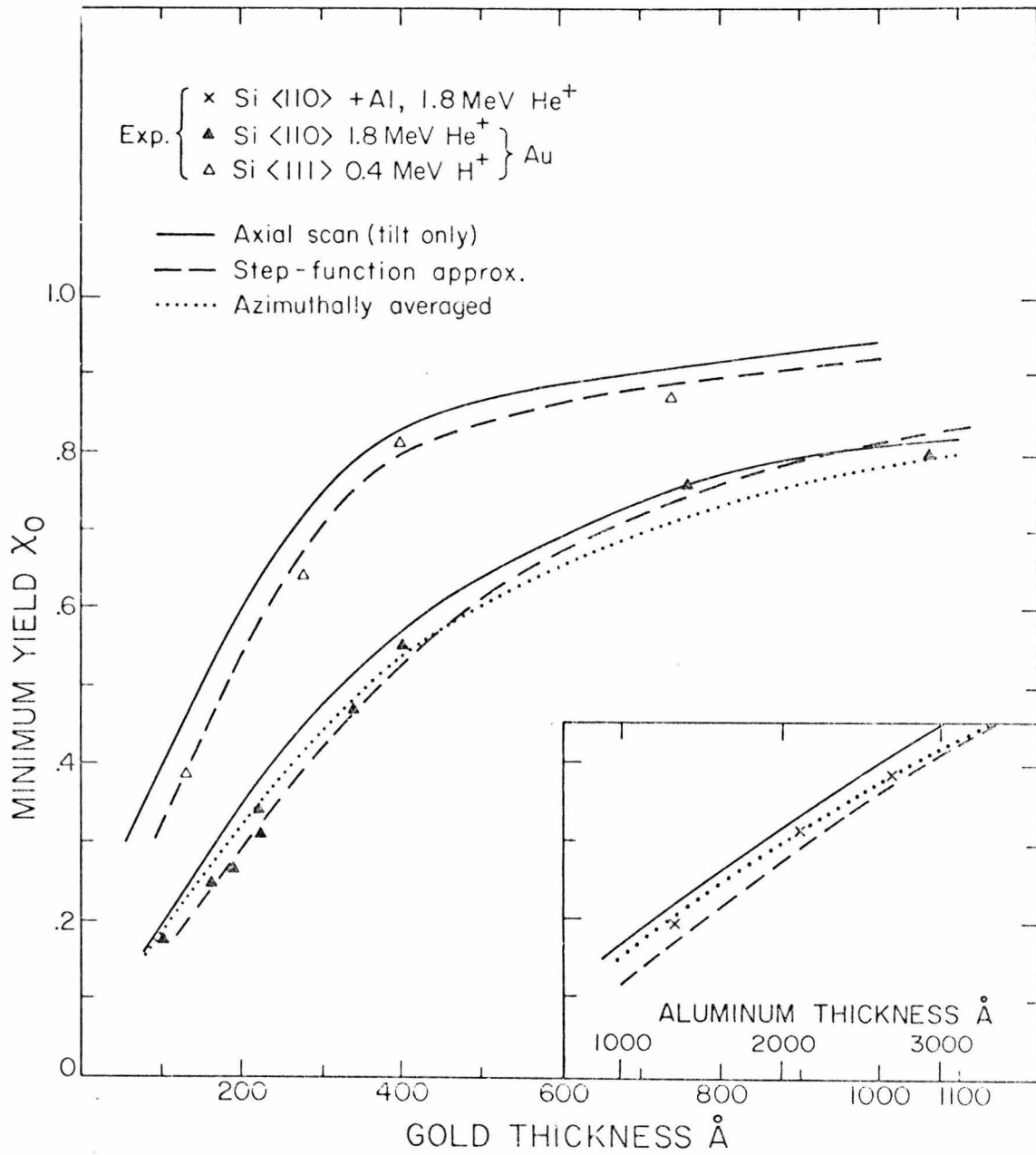
Figure 18

obtained in this fashion includes the effect of planar channels and hence gives a more representative average normalized yield.

For comparison, also shown in the dashed curves in Fig. 18 are the minimum yield values obtained by applying the step-function approximation to Meyer's theory of plural scattering. These minimum-yield values are in good agreement with experiment for nearly all m values for both He and H ions. In fact, these values nearly coincide with those obtained by convolution using an azimuthally-averaged angular-yield profile for gold thicknesses up to about 700Å. However, there is a systematic difference of about 3% for thicker films.

The insert in Fig. 18 shows a comparison of experimental Al minimum yield values with those obtained by applying the Meyer treatment of plural scattering and normalized yield curves determined from (a) the step-function approximation, (b) the axial angular-yield profile obtained by tilt only, and (c) the azimuthally averaged angular yield profile. The calculated minimum yield values from the azimuthally-averaged profile are in excellent agreement with experimental values. Also, in the first order approximation, there is adequate agreement with calculations based on step-function approximation.

B. Planar-Angular Yield Profiles

Another method of investigating the influence of amorphous layers is provided by measurements of the yield at the Si surface as a function of orientation between beam and crystal target. Such curves of the angular yield profiles are shown for uncovered Si and for Si covered with 2130Å Al in Fig. 6 (axial scan across the <110>) and Fig. 7 (planar scan across the {110}). The planar minimum yield for uncovered Si is larger than in the axial case due to the surface transmission factor. Even for the most favorable case, the {110}, the planar minimum yield is $\simeq 0.22$ for 1.8 MeV He ions yet it is only $\simeq 0.03$ for <110>. For covered Si, the full-width of the angular yield profile is broader than for uncovered samples.

The experimental planar minimum yield values and planar angular yield profiles on covered Si crystal have been compared with the predictions of plural scattering. The planar case has been investigated in more detail experimentally because the comparison with theory requires calculations which are more straightforward than those required in the axial case. Shown in Fig. 19 is a series of {110} planar angular normalized yield profiles for 1.8 MeV He$^+$ on Si, both uncovered and covered with different thicknesses of Al layers. The planar minimum yield increases with increasing film thicknesses, the shoulders

Figure 19. ´{110} planar-angular-normalized-yield profiles for 1.8 MeV He$^+$ on uncovered and covered silicon crystals with different thicknesses of Al films. The yields were measured at depths about 0.1 µm below the surface and normalized to 2500 counts.
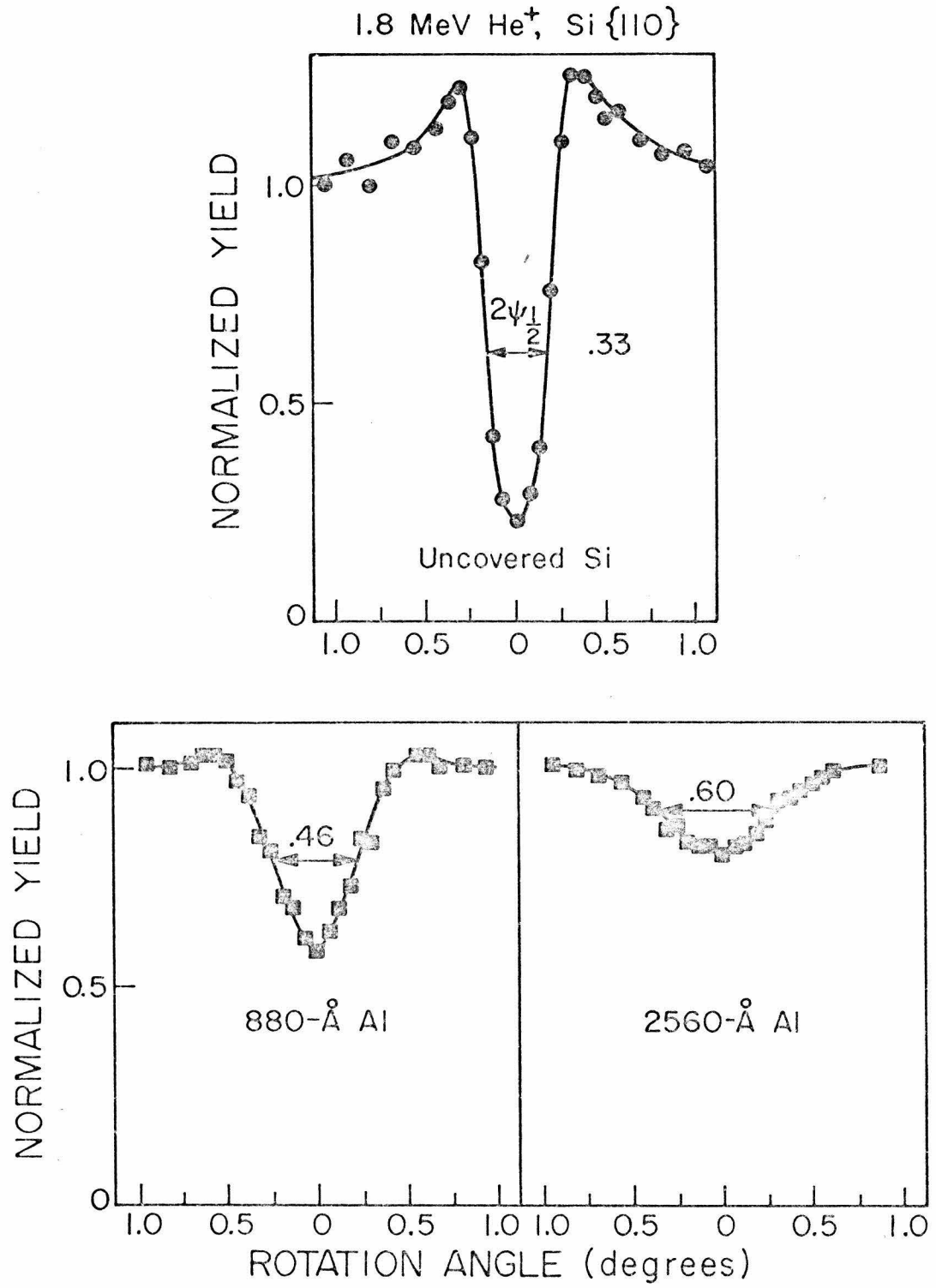
Figure 19

disappear and the full-width increases. These yield pro-
files were measured at depths about 0.1 μm below the sur-
face of the crystal.

To compare these experimental angular-yield pro-
files with plural scattering calculations, it is necessary
to determine the number of particles scattered through an
angle θ_p with respect to the plane, i.e., the projection
of the angle θ on a surface both normal to the plane and
parallel to the beam direction (see Eq. 2 and Fig. 2 in
Section I.B). The yield $Y_c(\theta')$ at any angle θ' of in-
cidence on covered Si is obtained by convolution of the
experimental planar scan on uncovered Si, taken as a prob-
ability function $P(\theta_p)$ with the projected-planar-distri-
bution function $f_p(\theta_p)$ displaced through the same angle θ',
i.e., $f_p(\theta_p - \theta')$. The yield is calculated from:

$$Y_c(\theta') = 2 \int_0^\infty P(\theta_p) f_p(\theta_p - \theta') d\theta_p \qquad (25)$$

Figure 20 shows the calculated and experimental planar
angular yield profiles for 1.8 MeV He$^+$ impinging along
{110} plane of Si crystal covered with 2560Å of Al. The
calculated profile using Meyer treatment of plural scat-
tering is in satisfactory agreement with the experimental
one.

Figure 20. Experimental and calculated normalized yield
as a function of rotational angle for 1.8 MeV He$^+$
impinging along the {110} plane of Si crystal
covered with 2560$\overset{\circ}{\text{A}}$ of Al.
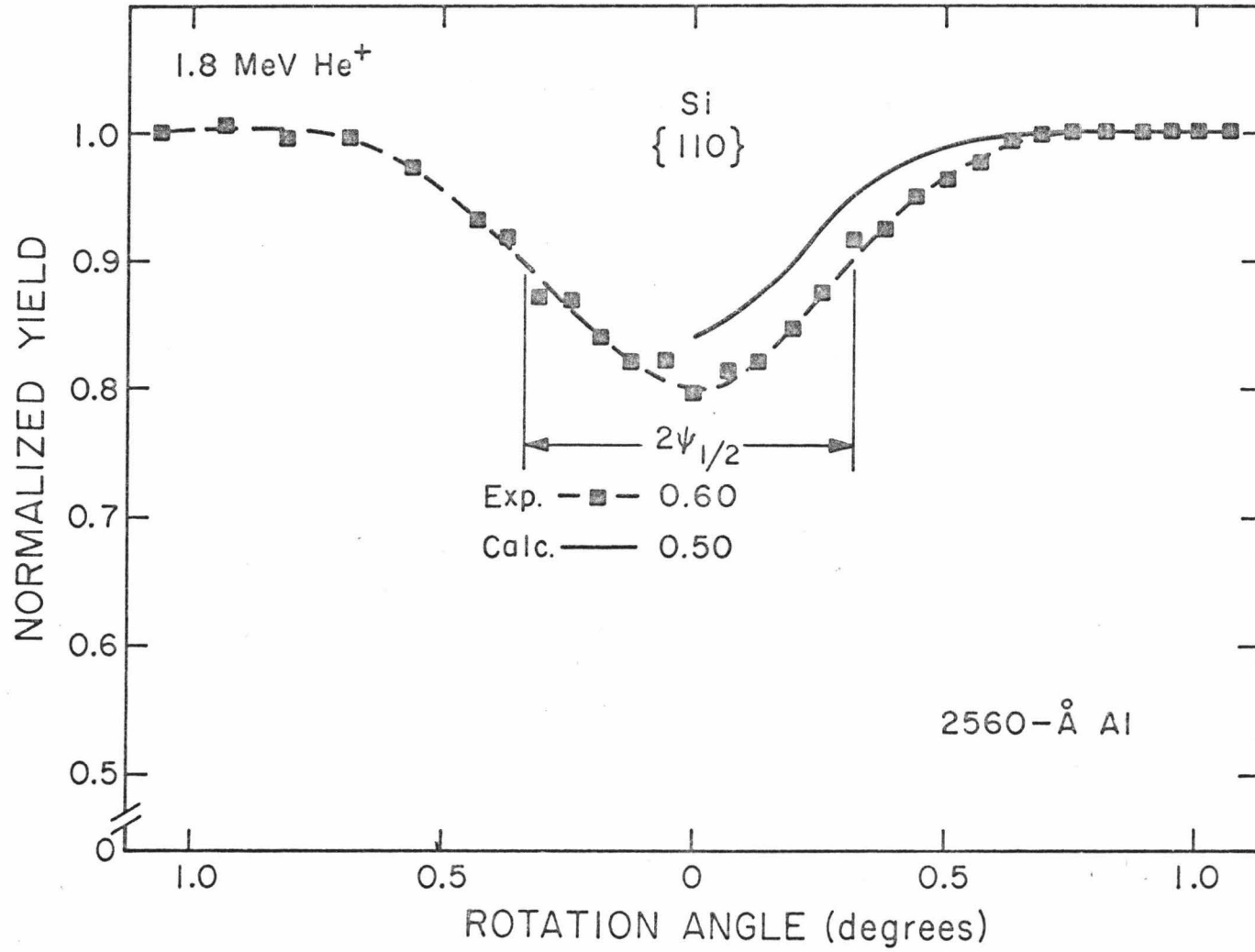
Figure 20

C. Dechanneling

The calculated axial minimum yield values discussed in the previous two sections gave information on the number of particles scattered beyond $\psi_{\frac{1}{2}}$ and the calculated planar-angular-yield profile utilized the entire scattering distribution. Another method of investigating the scattering distribution for angles less than $\psi_{\frac{1}{2}}$ is provided by the increase in minimum yield as a function of depth (dechanneling). We have calculated the dechanneling dependence on depth in two different ways: (a) utilization of dechanneling calculations based on the increase in transverse energy with depth, and (b) utilization of particle angle distribution in amorphous layer and the experimental angular yield profiles on uncovered crystal as a function of depth.

1. Transverse Energy

The incident angle θ of a particle traversing a film is related to its initial transverse energy $E_\perp$ inside the crystal, neglecting the deflection produced by the atomic row potential, by the relation $E_\perp = E\theta^2$, where E is the particle energy.

The transverse energy of a channeled particle is not conserved along its path inside the channel. It increases because of the scattering by target atoms and electrons of the crystal.[26] Transitions of particles

from the aligned to the random component of the beam are then possible as soon as the transverse energy reaches a critical value $E\psi_{\frac{1}{2}}^2$. As a consequence, an increase in the measured aligned yield with depth is observed. Foti et al.[38] have calculated the depth at which a particle of given initial transverse-energy reaches the critical value.

We have used their analytical procedure to calculate the depth at which a 1.8 MeV He ion with a given transverse energy will be dechanneled. This is shown as the lower solid curve in Fig. 21. This gives the depth at which a particle is dechanneled as a function of incident angle for the <111> direction in Si at room temperature.

Knowledge of the initial transverse-energy distribution allows calculation of the dechanneled fraction as a function of depth. The upper curve in Fig. 21 is the integral distribution (the number $F(\theta) = \int_{\theta}^{\infty} f(\theta)2\pi\theta d\theta$, where $F(\psi_{\frac{1}{2}}) = \chi_o$), obtained from Meyer treatment of plural scattering for m = 0.6 (264Å of Au). This gives the fraction of particles scattered beyond a given angle θ.

The two curves in Fig. 21 are used to determine the yield at any depth in the crystal. For instance, to determine the yield at a depth of 0.8 μ, one uses the lower curve to determine the maximum incident angle (transverse energy) for a particle to channel to a depth of 0.8 micron before dechanneling. Using this angle one

Figure 21. Upper: Integral distribution using the Meyer

treatment vs scattering angle for 1.8 MeV He$^+$

after traversing a reduced thickness m = 0.6

(264Å of Au).

Lower: The depth at which a particle with an

incident angle θ to the <111> direction reaches

the critical angle $\psi_{\frac{1}{2}}$ for dechanneling.
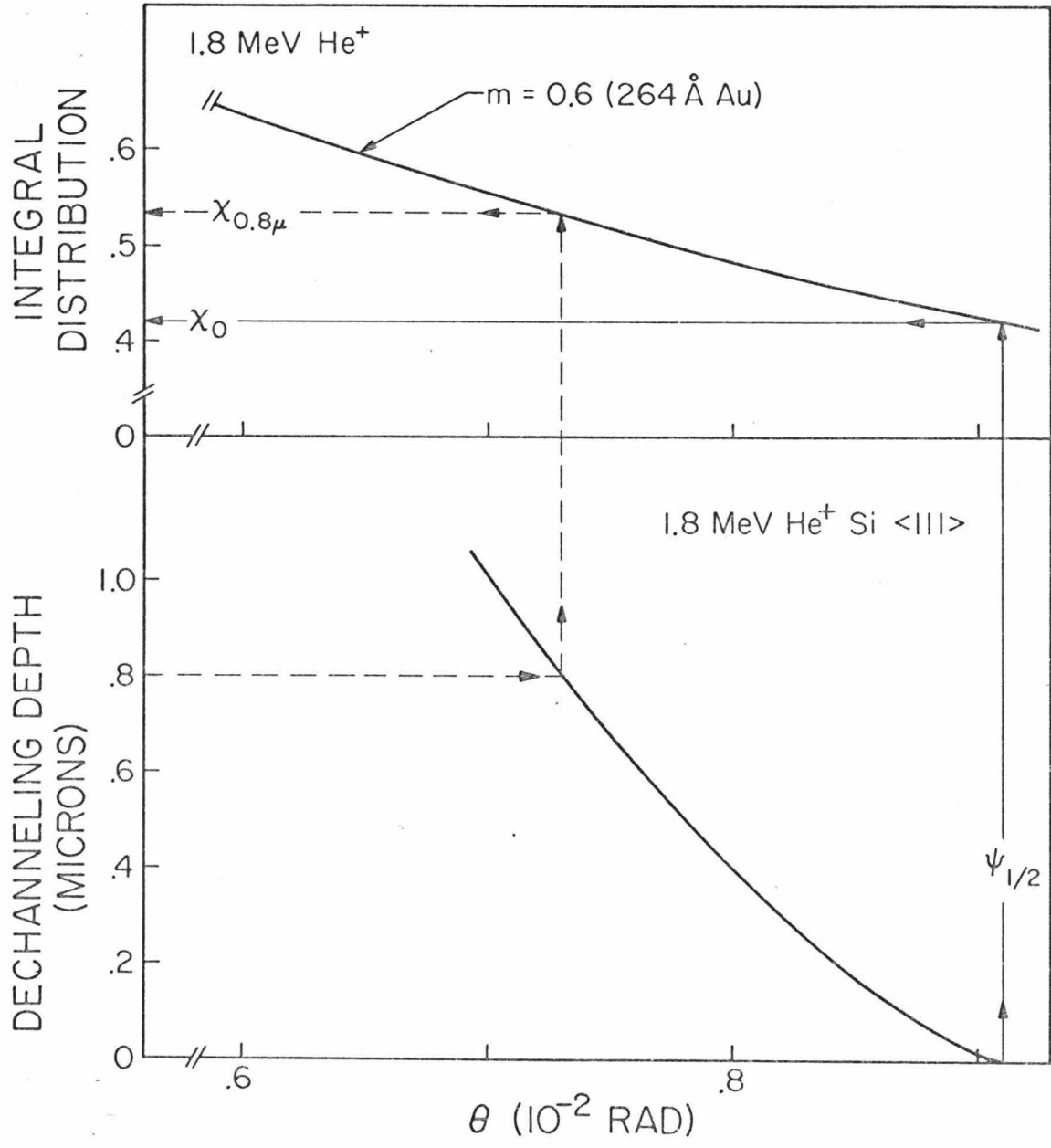
Figure 21

reads up to the integral distribution curve to find the dechanneled fraction, in this case $\chi = 0.54$. The minimum yield χ_0 at the surface is given by reading up from $\psi_{\frac{1}{2}}$ to the intersection with the integral distribution curve, and this gives $\chi_0 = 0.42$.

The results obtained with this procedure are shown in Fig. 22 for 1.8 MeV He$^+$ incident on <111> Si covered with 260Å of Au and 3090Å of Al. For the Al case, the calculated dechanneled fraction agrees well with experimental data. The results with Au indicate some departure at greater depths in the crystal between experimental and calculated curves.

2.   Angular-Yield Profile

Another procedure of computing the dechanneled fraction in covered Si single crystal utilizes both the experimental angular-yield profiles obtained at different depths inside the crystal and the calculated differential scattering distribution $2\pi\theta f(\theta)$. The angular-yield profiles shown in the lower part of Fig. 23 are treated as the experimental probability that a particle entering the crystal with an angle θ is dechanneled at a certain depth. Included in these curves are the transmission factor, the scattering in the channel and the dechanneling condition. The dechanneled fraction for a covered crystal at a given depth is obtained by convolution of the initial scatter-

Figure 22. Experimental and calculated-dechanneled frac-
tion χ vs depth for 1.8 MeV He$^+$ impinging along
the <111> direction of Si covered with (a) 260$\overset{o}{A}$
of Au (Δ); and (b) 3090$\overset{o}{A}$ of Al ($\square$). The de-
channeled fraction is calculated according to
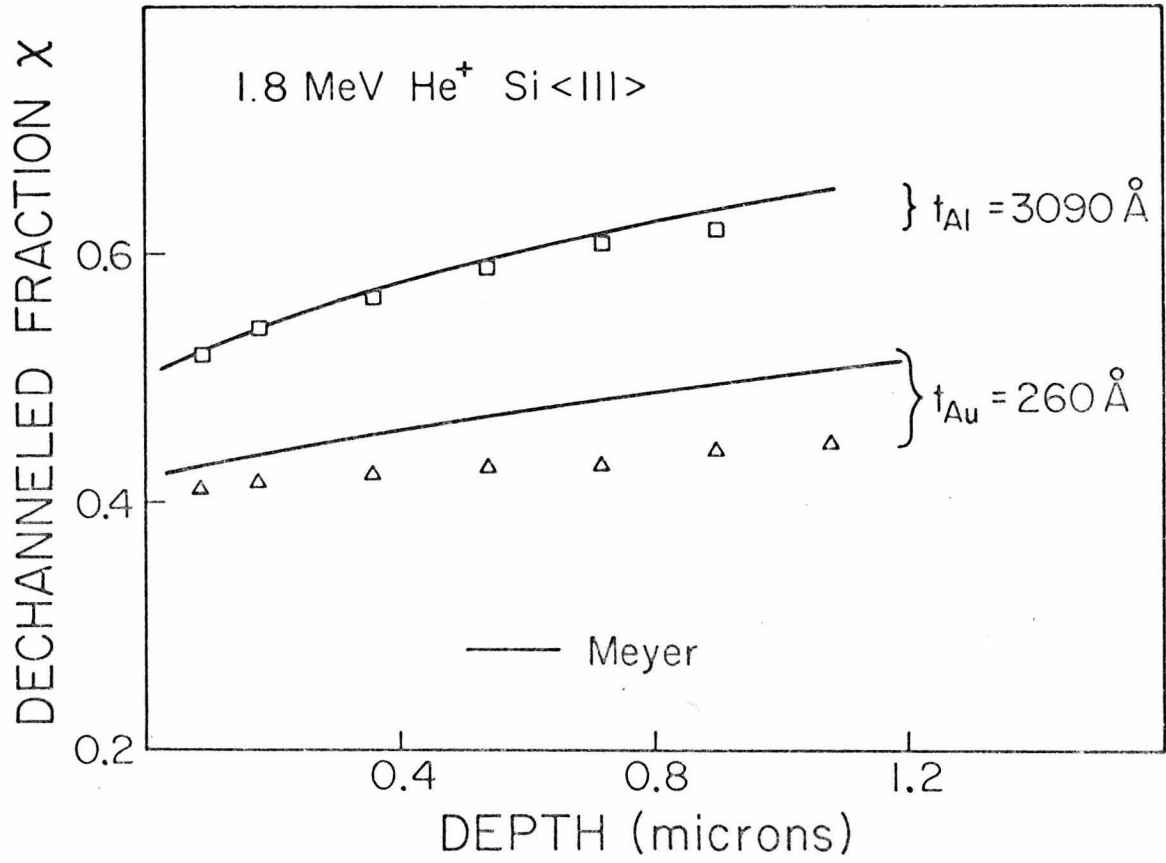Meyer treatment of plural scattering.

Figure 22

Figure 23. Lower: Normalized yield vs tilt angle obtained at three different depths for 1.8 MeV He$^+$ incident on uncovered Si.

Upper: Energy spectra for 1.8 MeV He$^+$ backscattered from uncovered silicon crystal tilted at various angles with respect to the aligned direction (this is also shown in Fig. 5).
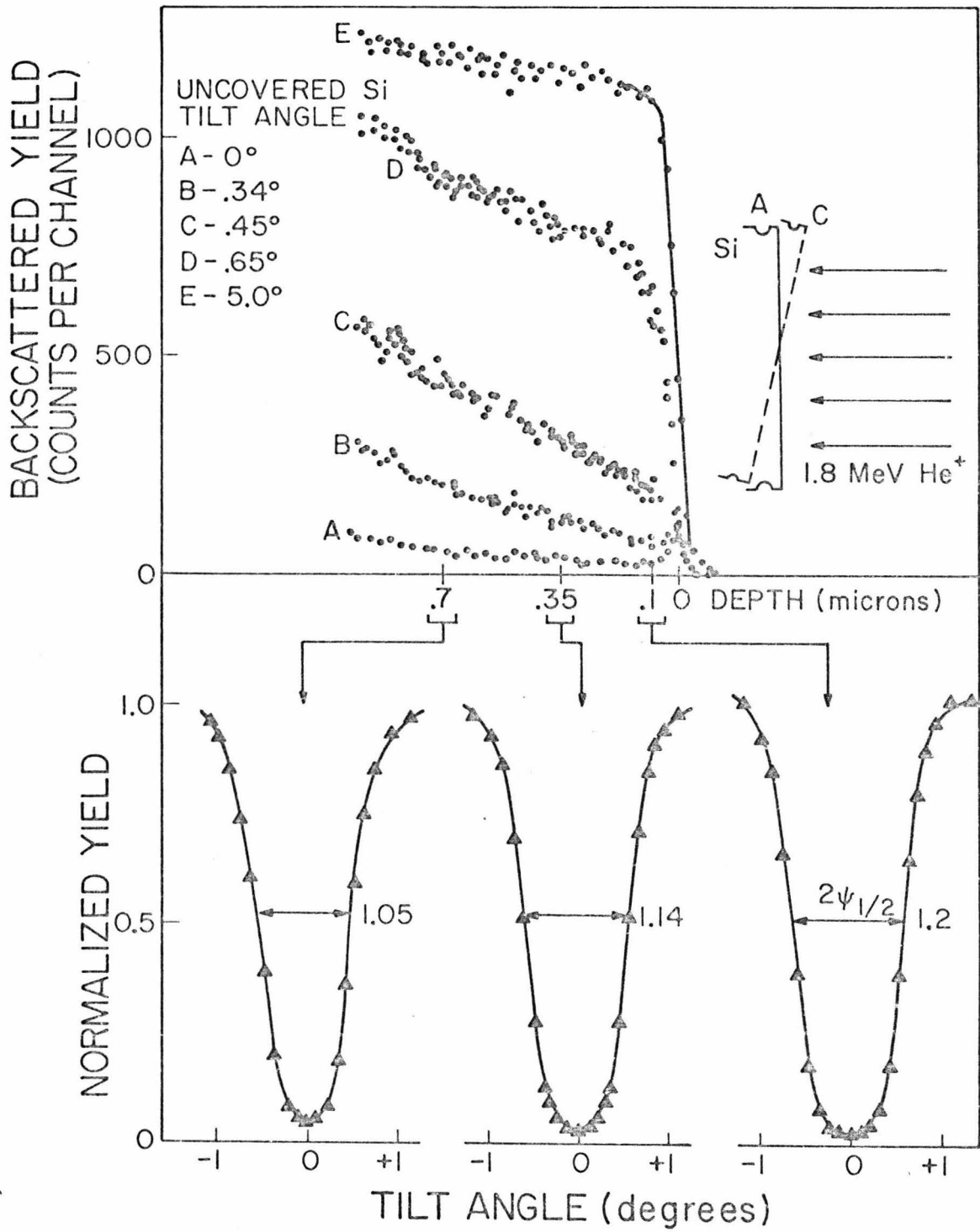
Figure 23

ing distribution in the amorphous film with the experimental angular profile at the given depth.

In Fig. 24 the dechanneled fractions calculated with the above procedure are compared with experimental values for 1.8 MeV He$^+$ impinging along the <110> direction of Si covered with 2130Å of Al and 190Å of Au. In both cases, the calculated increase in the dechanneled fraction with depth agree with experimental results. Again the calculated rate of dechanneling for Au films is somewhat greater than the measured rate.

In this latter procedure the differential distributions are calculated from Meyer's treatment of plural scattering and the yield profiles are the ordinary angular scans (not azimuthally-averaged). The experimental and the calculated data agree quite well for both absolute magnitude and rate of dechanneling. This method of utilizing the angular-yield profiles in determining the minimum-yield values and the dechanneling fractions in covered crystals is more accurate than the step-function approximation because it takes into account the transmission factor and the scattering in the channel. Perhaps, an even better agreement between experiment and theory could be obtained by utilizing the azimuthally-averaged angular-yield profiles rather than the tilt only axial scans.

Figure 24.   Dechanneled fraction χ vs penetration depth

for 1.8 MeV He$^+$ impinging along the <110> of Si

covered with 190Å Au (▲) and 2130Å Al (▩) layers.

The full lines represent the dechanneled fraction

calculated according to the method of using axial

angular yield profiles (shown in lower part of

Fig. 23).
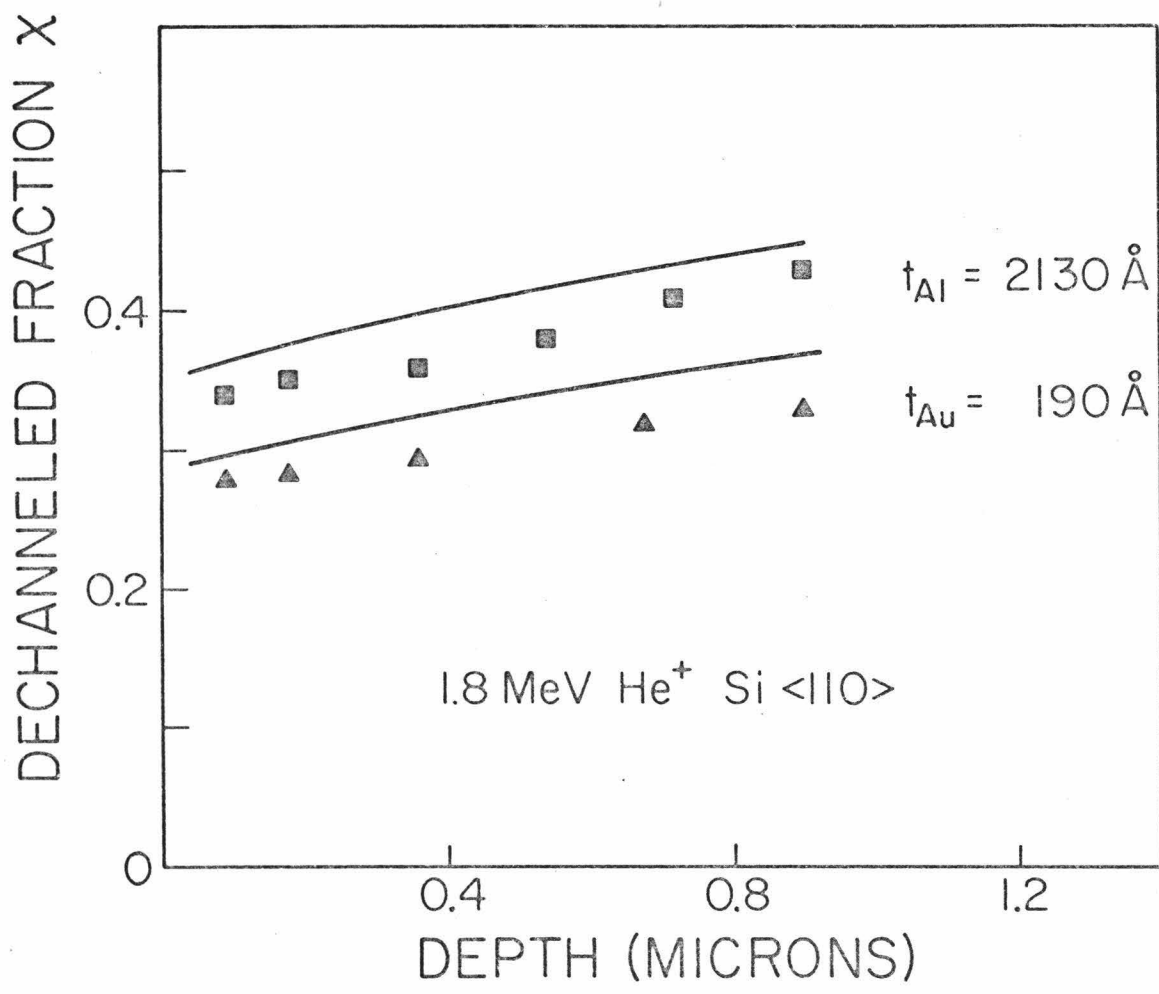
Figure 24

V. SUMMARY

Channeling-effect measurements have been used in investigating the minimum yield, the width of the angular-yield profile and the dechanneling dependence on depth $\chi(z)$ at different He^+ and H^+ energies for various Au and Al film thicknesses deposited on Si single crystals. These measurements indicate that the minimum yield, the angular yield profile as well as the dechanneling rate increase with increasing film thickness. From a qualitative standpoint, these results can be understood on the basis of scattering events within the metal films which cause an increase in beam divergence. However, in order to compare these results with the theoretical prediction, knowledge of the scattering in the film as well as the channeling behavior in the Si single crystal is necessary.

As far as characterizing the scattering in the film is concerned, Keil et al. and Meyer treatments of plural scattering were investigated. Minimum yield values obtained using both treatments were compared to the experimental values. We found that the experimental points followed the trend of both treatments but agreed in absolute magnitude more closely with Meyer treatment of plural scattering.

Subsequent applications and investigations of the

scattering in the film were based on the Meyer treatment of plural scattering. The channeling behavior in the Si single crystal was obtained by utilizing (a) step-function approximation, (b) two axial angular yield profiles and (c) the increase in transverse energy with depth. The assumption that the minimum yield χ_o at the surface of the crystal is determined by the number of particles incident with an angle greater than the critical angle $\psi_{\frac{1}{2}}$ (step-function approximation) was tested. The results indicated that this step-function approximation leads to a reasonable accurate determination of the axial minimum yield at the surface. For the planar case, it was found that surface transmission effects do not allow utilization of such a simple approximation. In this case, convolution techniques, as discussed below, should be applied.

Another procedure of investigating the channeling behavior is through convolution of the particle scattering distribution with experimental angular yield profiles on uncovered Si. Two different methods of determining such yield profiles were utilized. The first method which involves only tilting the sample is experimentally easier to carry out but yielded higher (by about 10%) axial minimum-yield values than the experimental data. These higher values are a consequence of the fact that the angular-yield profile is obtained by tilting the sample in a manner that avoids planar channels. Some small fraction

of the particles scattered in the amorphous film will be incident on the crystal with directions aligned with planar channels.

The second method of obtaining an angular-yield profile involves tilt and rotation and hence provides an azimuthal average which includes the effect of planar channels. The angular-yield profiles obtained in this fashion give a more representative average normalized yield. The calculated minimum-yield values obtained from these angular-yield functions and Meyer differential-scattering distributions are in good agreement with experimental values for Si covered with Au and Al films.

The azimuthally averaged yield functions are difficult to obtain experimentally as the procedure requires that the crystallographic axis of the sample be aligned with the axis of rotation of the goniometer to better than one-quarter of the critical angle. A simpler analytical procedure is to use the step-function approximation. The results are in agreement with experimental values to within a few percent. This suggests that in a first order approximation the step-function approximation generally is adequate for use in investigations of disorder in crystals by channeling effect measurements. For disorder analysis, we have established universal curves from which minimum-yield values can be obtained for various disordered depths.

Our technique of evaluating minimum yield and de-
channeling was further tested by measuring angular yield
profiles for planar scans and axial dechanneling rates.
These measured values were then compared with calculations
based on Meyer treatment of plural scattering. For planar
scans the convolution techniques were used to obtain the
yield as a function of angle of incidence; for Al covered
samples, the experimental and calculated results were in
agreement. Axial dechanneling rates were calculated on
the basis of (i) axial angular yield profile, and (ii) a
procedure based on the increase of transverse energy with
depth. For Al covered samples the calculated and experi-
mental values were in agreement.

APPENDIX

This appendix gives a method of calculating the minimum yield from a crystal overlaid with an amorphous crystal film by applying the step-function approximation and the distribution of the scattered particles given by Meyer.[17] Figure 25 shows a plot of the minimum yield $Y(\tilde{\theta}_c)$ as a function of the reduced critical angle $\tilde{\theta}_c$ for various reduced film thicknesses m (see Eq. A17). The reduced critical angle is given by $\tilde{\theta}_c = N\psi_{\frac{1}{2}}$, where $\psi_{\frac{1}{2}}$ is the critical angle for channeling and $N = a_{TF}E/2Z_1Z_2e^2$ (Eq. A22). For example, for 1.8 MeV He$^+$ incident on 440Å of Au on <110>-oriented Si, m = 1.0 and N = 41.6. The critical angle $\psi_{\frac{1}{2}} = 0.01$ rad. and hence $\tilde{\theta}_c = 0.42$ rad. The minimum-yield values taken from Fig. 23 is $Y(\theta_c = 0.42) = 0.57$. For 1550Å of Al, m = 10 and N = 420, the minimum yield values is $Y(\theta_c = 4.2) = 0.20$. The details of the calculation are given below.

A classical calculation of differential cross section for scattering is valid when: (a) the de Broglie wavelength λ of the incident particle is negligible compared with any significant dimension of the scattering center, and when (b) the collision is well defined within the limitations of the uncertainty principle.[39]

The differential cross section for scattering from

Figure 25. Solid lines represent the normalized inte-
        grated differential distributions using the Meyer
        treatment vs reduced critical angle for various
        m values (the reduced thickness of amorphous
        layers). Minimum yield χ_0 is obtained from these
        curves by the relation $\chi_0 = Y(\tilde{\theta}_c)$.
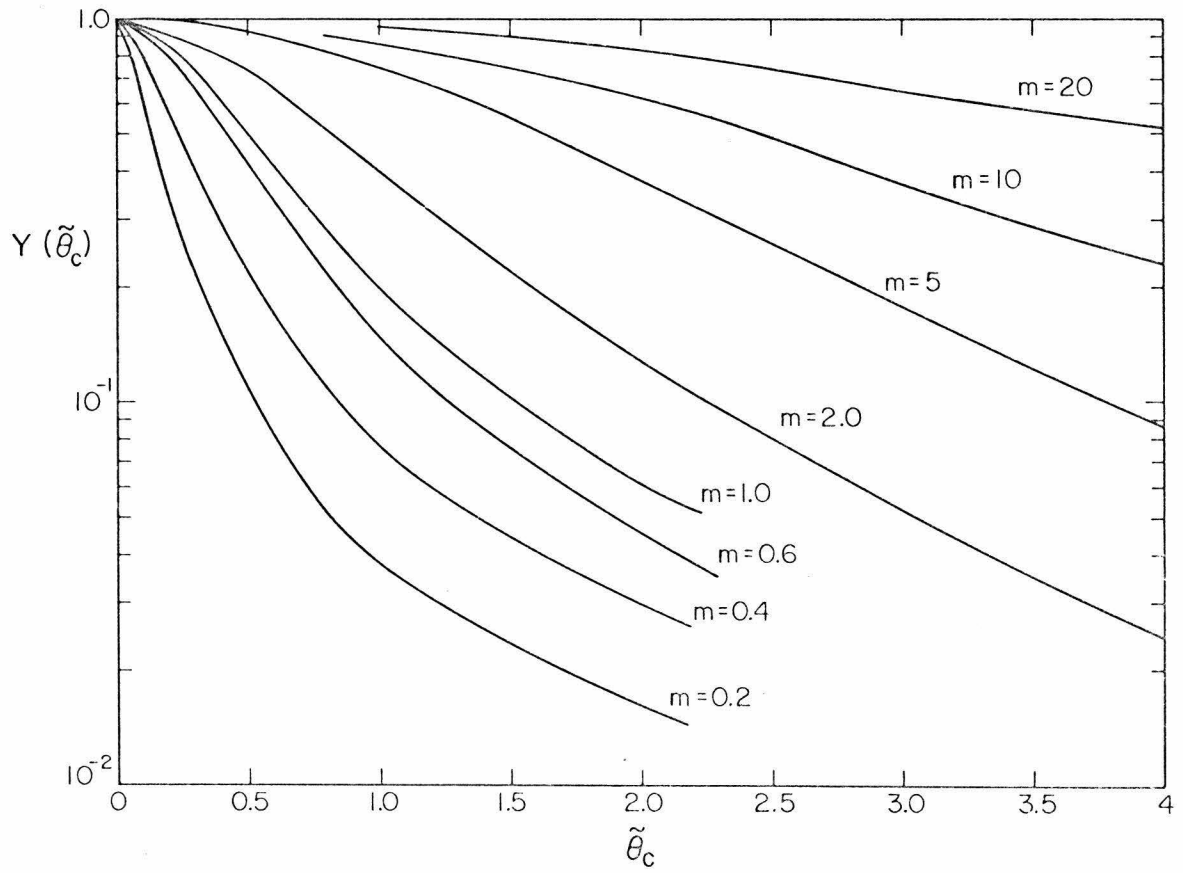
Figure 25

an arbitrary potential energy function $V(r)$ is calculated classically from[40]

$$\sigma(\theta) = - b db / \sin\theta \, d\theta, \tag{A1}$$

where

$$\theta = \pi - 2 \int_{r_o}^{\infty} [r f(r)]^{-1} dr, \tag{A2}$$

$$f(r) = [r^2/b^2 - 1 - r^2 V(r)/(\tfrac{1}{2}\mu v^2 b^2)]^{\frac{1}{2}}, \tag{A3}$$

and r_o is the distance of closest approach of the particles, defined by

$$f(r_o) = 0 \, . \tag{A4}$$

Here b is the impact parameter of collision and is defined by

$$b = z_1 z_2 \, e^2 / (\tfrac{1}{2}\mu v^2) \, . \tag{A5}$$

In this expression z_1 and z_2 are the atomic numbers of the incident and target atoms respectively. μ is the reduced mass of the system and v is the relative velocity of the collision. All angles θ are in center of mass system.

The calculations of the differential cross section

are based on the potential energy function

$$V(r) = \frac{z_1 z_2 e^2}{r} \phi\left(\frac{r}{a_{TF}}\right) \tag{A6}$$

where the screening function $\phi(r/a_{TF})$ is assumed to be the Thomas-Fermi function. The screening parameter or radius a_{TF} characterizes the screening of the nuclear charges Ze by the electronic shells, and may be computed approximately from

$$a_{TF} = a_o[0.885/(z_1^{2/3} + z_2^{2/3})^{1/2}] \tag{A7}$$

From the above equations one derives a differential scattering cross section which is a function of the scattering angle θ and reduced energy

$$\varepsilon = a_{TF}/b \tag{A8}$$

Lindhard et al.[41] introduced this parameter ε and also showed that the dependence of the cross section $\sigma(\theta,\varepsilon)$ on two variables θ and ε could be reduced to a dependence on only one quantity by introducing a parameter

$$\eta = \varepsilon \sin\theta/2 \tag{A9}$$

The resulting differential cross section is

$$\sigma(\eta) = \pi (a_{TF})^2 \frac{f(\eta)}{\eta^2} \qquad (A10)$$

and the function $f(\eta)$ is tabulated in Ref. 17.

Meyer, using a scattering cross section given in (A10), presents calculations on small-angle multiple scattering of low-energy heavy particles in solid layers. He gives the following angular distributions of particles of mass m_1 scattered in thin layers of mass m_2 by[17]

$$F(m,\tilde{\theta}) = \frac{1}{2\pi} \frac{\varepsilon^2}{4} \left(\frac{m_1 + m_2}{m_2}\right)^2 f_1(m,\tilde{\theta}) - \pi (a_{TF})^2 N^{2/3} f_2(m,\tilde{\theta}) , \qquad (A11)$$

where

$$f_1(m,\tilde{\theta}) = \int_O^\infty e^{-m\Delta(z)} J_O(\tilde{\theta}z) z \, dz \qquad (A12)$$

$$f_2(m,\tilde{\theta}) = \frac{1}{2}m \int_O^\infty e^{-m\Delta(z)} J_O(\tilde{\theta}z) \Delta^2(z) z \, dz \qquad (A13)$$

and

$$\Delta(z) = \frac{1}{4} \int_O^\infty f(y)' \{1 - J_O[z(y/2)]\} \, dy \qquad (A14)$$

m is a parameter defined in Eq. (A17), J_O is the zeroth-order Bessel function of the first kind and f is a scaling function given for different potentials in the work of

Lindhard, Nielsen and Scharff.[41]

The term $(a_{TF})^2 N^{2/3} f_2(m,\tilde{\theta})$ in Eq. (A11) is usually only a small correction to $f_1(m,\tilde{\theta})$ and can be omitted.[42] So

$$F(m,\tilde{\theta})\,d\omega = \frac{1}{2\pi}\,d\omega\,\frac{\epsilon^2}{4}\left(\frac{m_1 + m_2}{m_2}\right)^2 f_1(m,\tilde{\theta}) \qquad (A15)$$

gives the distribution of particles being scattered into solid angle $d\omega$ around the reduced scattering angle $\tilde{\theta}$.

Two parameters, a reduced angle and thickness $\tilde{\theta}$ and m, are introduced by Meyer and are defined by

$$\tilde{\theta} = \frac{1}{2}\,\epsilon[(m_1 + m_2)/m_2]\theta \qquad (A16)$$

and

$$m = \pi(a_{TF})^2\,Nt \quad, \qquad (A17)$$

where θ is the total scattering angle and N and t are the atom density and thickness of the target, respectively.

By substituting Eq. (A16) in (A15) and noting that we are dealing with small angle scattering,

$$F(m,\tilde{\theta})\,d\omega = \frac{1}{2\pi}\,[f_1(m,\tilde{\theta})\,2\pi\tilde{\theta}d\tilde{\theta}] \quad . \qquad (A18)$$

We now define a function $Y(\tilde{\theta}_c)$ as the integrated normalized differential distribution of the particles scattered beyond angle $\tilde{\theta}_c$ namely,

$$Y(\tilde{\theta}_c) = \int_{\tilde{\theta}_c}^{\infty} f_1(m,\tilde{\theta}) 2\pi\tilde{\theta} \; d\tilde{\theta} \qquad\qquad (A19)$$

and $Y(o) = 1$.

Application of the step-function approximation to the differential distribution of the particles in order to find the minimum yield assumes that a particle is in the random component of the beam (dechanneling probability equal to unity) when its angle with the channel axis is greater than $\tilde{\theta}_c$, the reduced critical angle for channeling. From Eq. (A19) we identify minimum yield χ_o for a particular reduced film thickness m as

$$\chi_o = Y(\tilde{\theta}_c) \; . \qquad\qquad (A20)$$

Determination of $\tilde{\theta}_c$: Substituting Eqs. (A5) and (A8) in (A16) yields

$$\tilde{\theta} = (a_{TF} \; E/2Z_1 Z_2 e^2)\theta = N(E,Z_1,Z_2)\theta \qquad (A21)$$

where $E = (mv^2)/2$ is the energy of incident ions, and

$$N(E,Z_1,Z_2) = a_{TF} \; E/2Z_1 Z_2 e^2 \; . \qquad\qquad (A22)$$

For crystals overlaid with metal films, the reduced
critical angle $\tilde{\theta}_c$ is given by

$$\tilde{\theta}_c = N(E, Z_1, Z_2) \psi_{\frac{1}{2}} \qquad (A23)$$

where $\psi_{\frac{1}{2}}$ is the usual critical angle for channeling on
uncovered crystals and $N(E, Z_1, Z_2)$ is a normalizing factor.

In conclusion, we remark that the introduction of
reduced parameters such as scattering angles and energy by
Meyer in the treatment of plural scattering has useful
consequences. One of them being that the form of the
scattering distribution is independent of the energy of
the incident ions, if measured in reduced scattering angle.

PART II

LOW-TEMPERATURE MIGRATION OF SILICON

THROUGH METAL FILMS

I.   INTRODUCTION

Until recently, a large part of the information on metal-semiconductor structures was obtained from studies of their electrical properties.[43]   Investigations on rectifying properties, barrier heights, Schottky barriers and formation of contacts in these metal-semiconductor systems have received great attention.   In particular, studies on the formation of contacts have been carried on using techniques such as (i) the photoelectric method, (2) extrapolation of the inverse square capacitance of the Schottky junction versus voltage plot, and (3) the study of the conduction across the contact in the forward as well as the reverse directions.[44]

However, with the advent of integrated circuit technology it became necessary to study, using as many techniques as possible, some silicon-metal systems as a first step towards establishing some criteria for good electrical contacts.   Conventionally, contacts to Si are formed when a particular metal is deposited on Si and then the system heat treated at a certain temperature.   The success of the formation of these electrical contacts relies on a detailed study of a number of silicon-metal systems.

Our studies started with investigations of Si-Au

and Si-Ag systems at temperatures well below those at which any liquid phase exists. Ion backscattering spectrometry was used as the analytical tool. When this investigation was started about three years ago, very little was known about these systems at temperatures in the range of 100-300°C. We found that silicon migrated through metal films to the front surface of the metal after heat treatment at surprisingly low temperatures.[45]

The migration of Si through metal layers to the surface of the metal layers was detected by the formation of a silicon oxide layer. We observed in our work that a thick silicon oxide layer could readily be grown on top of evaporated gold layer on a silicon substrate by heat treatment in an oxidizing ambient. At temperatures well below the Si-Au eutectic point (375°C), Si migrated through the gold film and accumulated at its front surface. These silicon atoms were then oxidized and formed an oxide layer. The presence of this layer could even be detected from the color of the sample surface.[46,47]

In the Si-Ag system, Si migration was observed at about 400°C well below the Si-Ag eutectic point (830°C). In this case, Si migration began at higher temperatures than that in the Si-Au case.[45]

A study of the limiting factors in these low-temperature processes was made by investigating the effect of the interface and of different ambients. The factors

governing the growth of the oxide layer which is a by-product of silicon migration were investigated. We found that the presence of an oxide layer between the Si surface and evaporated metal layer tends to suppress significantly the growth of the oxide layer on top of the Au or Ag layer.[47]

Recently a number of other silicon-metal systems have been studied at low temperatures. These studies have concentrated on the formation of various phases of metal silicides. In particular, Pd-Si, Cr-Si, Ti-Si, Mo-Si, Hf-Si and V-Si have been well covered.[48-54] Migration of Si and Ge in Al films has also been studied.[55-57] The general result pertinent to these systems is the low-temperature migration of Si and Ge in metal films. In general it has been found that the temperature at which Si or Ge is observed to migrate is about one-third the melting point (in ^{O}K) of the system.

In retrospect, the existence of low temperature migration of semiconductors through thin evaporated metal films is now an established phenomenon. When we started our studies three years ago with the Si-Au system, the results seemed unique to this particular system. However, it is no longer an isolated entity but applies to a general class of semiconductor-metal combinations. This concept has led to an understanding of a wide range of problems such as dissolution and transportation of Ge through Al

and subsequent epitaxial regrowth of Ge.[55]

II. EXPERIMENTAL PROCEDURES

The silicon substrates used in this work were single crystal with <110>- and <111>-orientations. These wafers which were of both n- and p-type had a resistivity of 4-6 ohm-cm. Prior to deposition of metal films, the wafers were cleaned in hot nitric acid and then kept in a dilute hydrofluoric acid (HF) solution to avoid surface oxidation. The wafers were later rinsed in distilled deionized water as a final step just before evaporation. The evaporations were made in a system which was evacuated to about 5×10^{-7} Torr. The thickness of Au deposited ranged from 200 to 4000Å and that of Ag from 200 to 800Å.

Immediately after evaporation, the adherence of the evaporated gold and silver films to the silicon substrate was tested using Scotch tape. In some cases the films showed bad adherence and these specimens were not used for further experiments. It is known that dipping a single crystal silicon substrate into either hot nitric acid (HNO_3) or boiling water introduces a thin oxide layer (30-100A°) on the substrate. In particular, gold films deposited on these slightly oxidized substrates did not show any adherence. This suggests the absence of a significant oxide layer on samples which exhibited good adherence. These samples which showed good adherence were

kept in a dessicator awaiting heat treatment.

Heat treatments of the specimens were made in quartz tube furnace under several different conditions (temperature, treatment time, oxidizing and nonoxidizing atmospheres). The oxidation procedure involved the use of three different oxidizing atmospheres (air, dry pure oxygen and steam) all at atmospheric pressure. Steam was obtained by boiling deionized distilled water. The non-oxidizing atmosphere was forming gas (a mixture of nitrogen and hydrogen). The appropriate atmosphere was directed into a 25 mm ID quartz tube contained in a three-zone furnace.

These heat-treated specimens and also "as evaporated" specimens were exposed to 2 MeV He^+ ions to obtain backscattering spectra. Backscattering measurements were performed using a 2 MV accelerator at the Kellogg Radiation Laboratory of Caltech. The apparatus is shown schematically in Fig. 8 of Part I of this work. A monoenergetic, collimated beam of helium ions produced by the accelerator impinges onto samples mounted on a goniometer in an evacuated scattering chamber. A few of these helium ions scatter back into the solid state surface barrier detector. The detector and a preamplifier-amplifier system produce voltage pulses whose amplitudes are proportional to the energy of each backscattered particle within field of view of the detector. These pulses are sorted according to

amplitude and stored by the multi-channel analyzer to pro-
duce a spectrum which displays the number of helium parti-
cles in a given channel (energy interval) against their
energy. The energy-to channel-number conversion, typically
between 2 and 5 keV per channel, was calibrated by scatter-
ing from Si, Cu, Ag and Au targets.

III.   ANALYSIS: PRINCIPLE OF BACKSCATTERING TECHNIQUE

Energy analysis of backscattered particles pro-
vides[58-61] ability to distinguish (i) atomic masses of
the elements; (ii) the depth distribution of the atoms
present in the target, and (iii) the crystalline nature of
the target.

A.   Mass Determination of Elements in the Target

When a flux of monoenergetic helium ions impinges
upon the target, most of the ions will penetrate a few
layers of the target. A very few helium ions will collide
with the surface atoms and will be elastically scattered
back by the Coulomb repulsion of the atomic nuclei. The
energy E' of the helium particle after such an elastic
scattering is smaller than its initial energy E_o (see Fig.
1a). From the energy E', one can determine the mass M_2 of
the target atom. This energy E' depends on the incident
energy E_o, mass M_1 of the incident particle, mass M_2 of
the target atom and a backscattering angle θ (which is
fixed by the detector geometry in the laboratory system
of coordinates), and is given by

$$E' = K^2 E_o$$

Figure 1. Schematic scattering geometry (a) and back-
scattering energy spectra generated from targets
of (b) silicon substrates under the metal films,
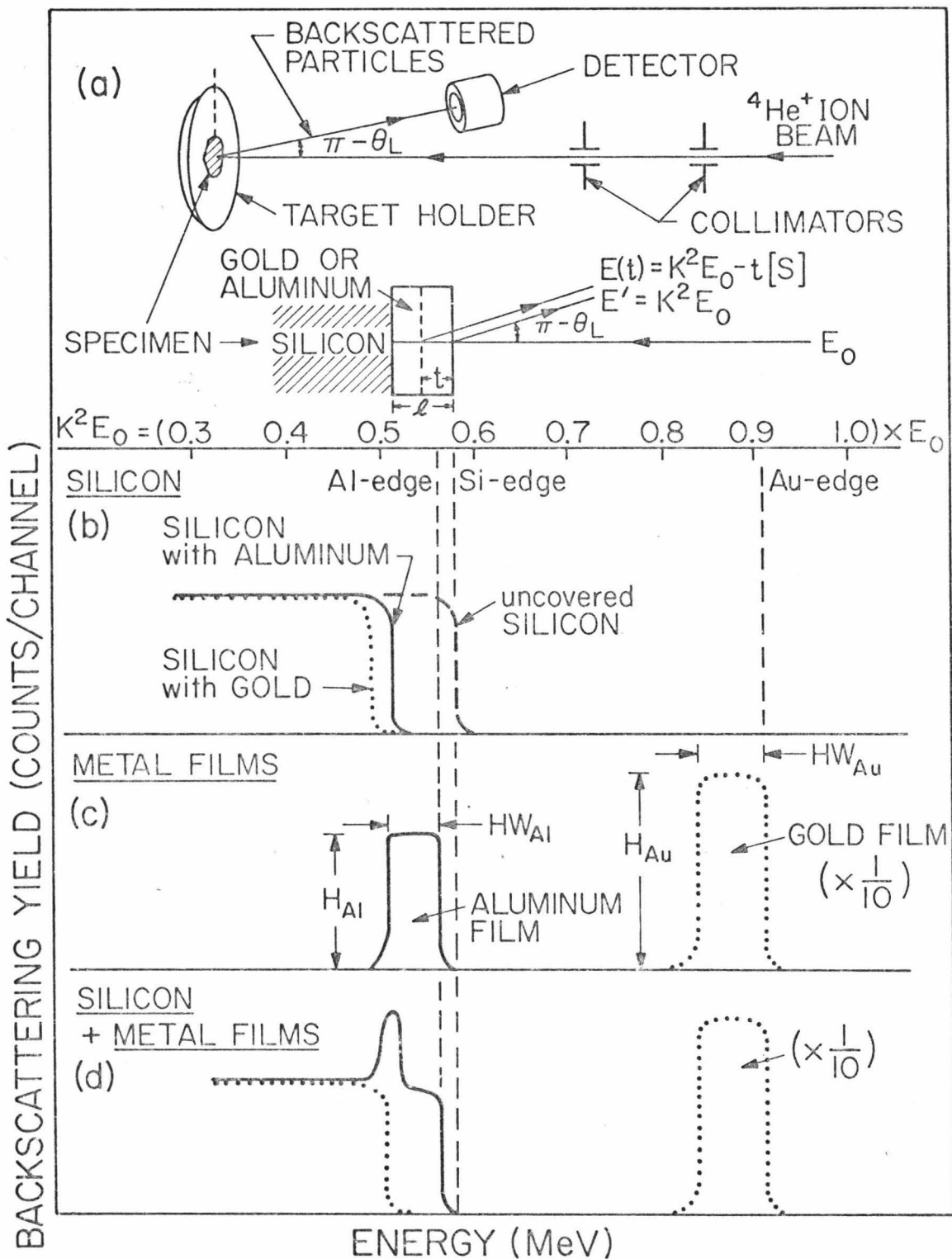(c) metal films, and (d) metal films overlying
silicon.

Figure 1

where the kinematic recoil factor K^2 is given by Eq. 12 (Part I). For $\theta = 170^{\circ}$, the values of K^2 for helium incident on Si, Ag and Au is 0.556, 0.863 and 0.925 respectively, ($M_1 = 4$, $M_{Si} = 28$, $M_{Ag} = 108$ and $M_{Au} = 197$).

B.   Depth Distribution of Atoms

In addition to elastic recoil at large angles from collisions with the atoms on the surface of the substrate, the incident helium particle suffers numerous small-angle deflections as it penetrates the target. The measured energy of He^+ particles backscattered at a depth t below the surface is lower than that from atoms on the target surface. This is due to the energy loss of the particle in penetrating the target to depth t and in exiting. The energy loss per unit distance traversed in the crystal is calculated from the data on stopping power. Then it is possible to convert backscattering spectra from energy to depth scales to obtain the depth distribution of atoms.

To illustrate the above mentioned features, a schematic representation of backscattering spectra of two silicon wafers covered with either aluminum or gold films with the same thickness ℓ are shown in Fig. 1. Particles are scattered from atoms of Al or Au on surface with energy $E(o) = K^2 E_o$, while the particles scattered from atoms at depth t below the surface have energy $E(t) = K^2 E_o - t[S]$. Here $[S]$ is the backscattering energy-loss

parameter which relates energy to the depth scale and is given by Eq. 13 of Part I of this thesis. Representative values for [S] at 2.0 MeV He$^+$ for Al, Ag and Au are 46.2, 104.5 and 134.0 eV/$\overset{\circ}{A}$ respectively.

Shown in Fig. 1b are the leading edges of spectra from uncovered silicon (dashed line), Si covered with Al (solid lines) and Si covered with Au (dotted line). The covered spectra appear at lower energies from that of uncovered silicon. In particular, the larger shift of the spectrum of Si covered with Au comes from the large stopping power of Au, and hence larger energy loss of He$^+$ particles in traversing the gold film. Figure 1c shows spectra from self-supporting films of Al and Au. The Au spectrum appears at high energy because of its larger kinematic recoil factor (K^2). The superposition of Fig. 1b with 1c gives the actual spectra 1d of the specimens: solid line for Si-Al and dotted line for Si-Au. In contrast with Si-Au case whose resultant spectrum is simple, the spectrum of Si-Al is characterized by a sharp peak which is due to particles scattered by Si and Al in the interface. A similar case of overlapping spectra will be discussed later for the Si-Au-Ag system.

The investigation of stoichiometry as well as the uniformity of thin films can also be accomplished using the backscattering technique. Figure 2a shows schematically the energy distribution of 2 MeV He ions

Figure 2. Schematic spectra for 2 MeV ^{4}He ions scatter-
ing from (a) Si substrate covered with a uniform
layer of evaporated Au, (b) a similar sample like
(a) with a uniform layer of 1000Å thick SiO_2, and
(c) a sample with a nonuniform layer of SiO_2.
In these spectra the yield from the Au layer is
reduced by a factor of 10. The shading in the
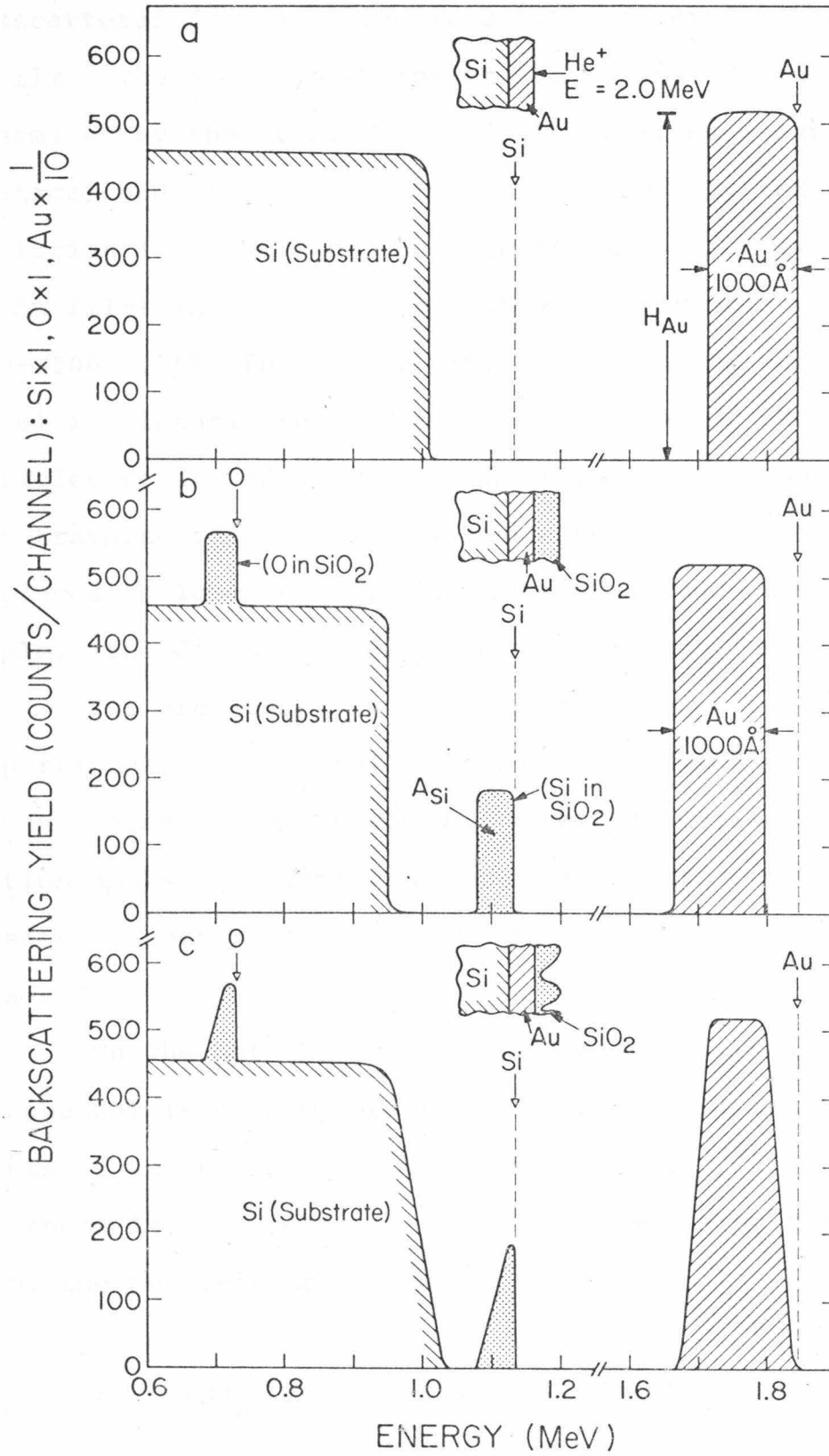sample configurations corresponds to the shading
in the backscattering spectra.

Figure 2

backscattered from a silicon substrate covered with 1000Å
Au film. The energy position of the Au leading edge is
determined by the atomic mass of the Au atoms (scattering
kinetics) and the slope of the leading edge by the energy
resolution ($\simeq$ 15 keV) of the detector-amplifier system.
For Au films in the thickness range used in this work
(400-3000Å), the full-width at half-maximum of the Au
signal is linearly related to the thickness of the Au film.
Particles scattered from the underlying silicon substrate
must traverse the Au film and hence the Si spectrum is
displaced to lower energy than that of an uncovered Si
sample, (the Si edge is denoted by a broken line).

The area under each of the spectra in Fig. 2 is
proportional to the total number of corresponding atoms
per unit area. From knowledge of the scattering cross
section and stopping power of the target atom, the con-
version of scattering yield to atomic concentration is
obtained.

The height H_{Au} of the gold signal given in counts
per channel is determined by the number of scattering
events in an incremental gold thickness Δt.[62] The
thickness is related to the width of one energy channel
δE of the multi-channel analyzer by

$$\delta E = [S]_{Au} \, \Delta t \qquad\qquad (4)$$

Here δE is fixed by the gain of the electronic system and is typically 2 to 5 keV. So the height H_{Au} of the gold signal is given by

$$H_{Au} \text{(counts/channel)} = Q(\delta\Omega) \left(\frac{d\sigma}{d\Omega}\right)_{Au} N_{Au} \Delta t \quad (5)$$

Putting Eqs. 4 in 5 yields

$$H_{Au} \text{(counts/channel)} = Q(\delta\Omega) \left(\frac{d\sigma}{d\Omega}\right)_{Au} \left(N_{Au} \frac{\delta E}{[S]_{Au}}\right) \quad (6)$$

where Q is the integrated charge of incoming He^+, $\delta\Omega$ is the solid angle subtended by the detector, $(d\sigma/d\Omega)_{Au}$ is the scattering differential cross section of gold and N_{Au} the atomic (Au) concentration per unit volume.

Using Eq. 6 we calculate the number of counts per channel for 2.0 MeV He^+ scattering from a layer of Au at $\theta = 170^{\circ}$. Here a typical integrated charge Q corresponds to 3.75×10^{13} particles (6 μC or 10 nA for 10 min) and the solid angle $\delta\Omega$ is 2.5 msterad (25 mm^2 detector at 10 cm distant). The energy δE of one channel width is taken as 3.0 keV. The gold backscattering loss parameter $[S]_{Au}$ is 134.0 eV/Å, and gold bulk density $N_{Au} = 5.9 \times 10^{22}$ atoms/cm^3. The differential cross section $(d\sigma/d\Omega)_{Au}$ is 8.1×10^{-24} cm^2/Sr. Substituting these values into Eq. 6 gives a height of gold H_{Au} of 10^4 counts per channel.

Spectra Fig. 2b for Si-Au samples covered with a

thin uniform layer of SiO_2 exhibit more detail. The con-
tributions from both Au and Si substrates are displaced
to lower energies by amounts proportional to the thickness
of the SiO_2 layer. The contribution to the spectrum from
the silicon and oxygen in SiO_2 has two components, the
leading edges of which are determined by scattering kine-
tics (the oxygen signal appears at lower energy because of
its lower mass). The heights of the Si (in SiO_2) signal is
lower than that from uncovered Si because of the smaller
number of Si atoms per unit energy loss in the oxide as
compared to those in the Si substrate. The composition of
the oxide layer is found from the ratio of the integrated
areas of the oxygen and silicon signals corrected by the
ratio of the scattering cross sections of the two elements
$[(d\sigma/d\Omega)_{Si}/(d\sigma/d\Omega)_O]$ i.e.

$$\frac{N_{Si}}{N_O} = \frac{A_{Si}/\left(\frac{d\sigma}{d\Omega}\right)_{Si}}{A_O/\left(\frac{d\sigma}{d\Omega}\right)_O} \tag{8}$$

Alternatively the number of silicon atoms/cm^2 in
the oxide layer can be determined from comparison of the
integrated silicon signal A_{Si} to the height of the Au
signal H_{Au} (a similar procedure is used in analysis[7] of
the number per cm^2 of dopant ions implanted in silicon).

The total area A_{Si} in counts under the Si in SiO_2 is given by

$$A_{Si} = Q(\delta\Omega) \left(\frac{d\sigma}{d\Omega}\right)_{Si} (Nt)_{Si} \qquad (9)$$

where $(Nt)_{Si}$ is the number of silicon atoms/cm^2. From Eqs. 6 and 9 we have

$$(Nt)_{Si} = \frac{A_{Si}}{H_{Au}} \frac{\left(\frac{d\sigma}{d\Omega}\right)_{Au}}{\left(\frac{d\sigma}{d\Omega}\right)_{Si}} \left(N_{Au} \frac{\delta E}{[S]_{Au}}\right) \qquad (10)$$

Using Eq. 10 we calculate the number of silicon atoms/cm^2. The total area A_{Si} in counts under the Si in SiO_2 is taken as 800 and the differential cross section $(d\sigma/d\Omega)_{Si} = .25 \times 10^{-24}$ cm^2/Sr for 2.0 MeV He^+ (scattering angle of 170°). From Eq. 7, $H_{Au} = 10^4$ counts per channel. The gold concentration N_{Au}, the energy loss parameter $[S]_{Au}$ and energy per channel δE, all retain their previous values presented in a discussion leading to Eq. 7. Hence

$$(Nt)_{Si} = \frac{800}{10^4} \frac{\left(\frac{d\sigma}{d\Omega}\right)_{Au}}{\left(\frac{d\sigma}{d\Omega}\right)_{Si}} \left(N_{Au} \frac{\delta E}{[S]_{Au}}\right) = 3.1 \times 10^{16} \text{ atoms/}cm^2 \qquad (11)$$

This is equivalent to an SiO_2 thickness of about 1000Å.

In film analysis experiments, the spectra represent averages of the film composition over the width of the analysis beam spot, typically 1-2 mm. If film non-uniformities in thickness or composition occur over these dimensions, the resultant spectrum can exhibit leading and trailing edges with slopes greater than those normally encountered; i.e. greater than the energy resolution of the system $\simeq$ (15 keV) or the energy spread due to straggling effects.[63] Figure 2c shows schematically the influence of a nonuniform oxide-layer thickness. The high-energy (leading) edges of the Au- and Si-substrate signals both reflect the thickness variation in the oxide layer (0-1000Å) as does the slope of the Au trailing edge. Because the oxide layer is outermost, the leading edges of the Si (oxide) and oxygen signals are sharp while the trailing edges are indicative of the nonuniformity of the oxide layer.

IV.   RESULTS AND DISCUSSION

A.   Low-Temperature Migration

Figure 3 shows backscattering spectra obtained with 2 MeV He$^+$ on films of gold (upper part of figure) and silver (lower part of figure) deposited on freshly prepared <110> surfaces of silicon. The spectrum of the silicon substrate in these untreated (as evaporated) samples is shifted below the silicon edge at 1.14 MeV by the energy lost in the overlaying metal films. An anneal of the system for 10 min in air induces silicon migration through the film to the metal surface in both the gold and the silver films. This migration, however, begins at a lower temperature for gold than for silver, and is already well developed at 200°C for gold and at 400°C for silver.

The low-temperature migration of silicon through evaporated metal layers is not an isolated phenomenon but rather seems to be a property shared by a class of metals. In this connection, it is noteworthy that silver and gold both form a eutectic with silicon, and that the eutectic point of Si-Ag (830°C) is also higher than that of Si-Au (375°C). [64]

Another difference between these two cases lies in the distribution of silicon both in the bulk and at the surface of the metal film after anneal. In the Si-Au

Figure 3. Energy spectra obtained with 2 MeV ^{4}He ions back-
scattered from a randomly positioned silicon single
crystal covered with a thin layer of gold (900Å)
(upper part) or silver (800Å) (lower part). The
shift of the silicon signal in the "as evaporated"
spectra (x) is due to the overlying metal film.
After an anneal of 10 min in air (●), silicon
migrated through the film to the metal surfaces.
The signal of the oxygen in the layer is located
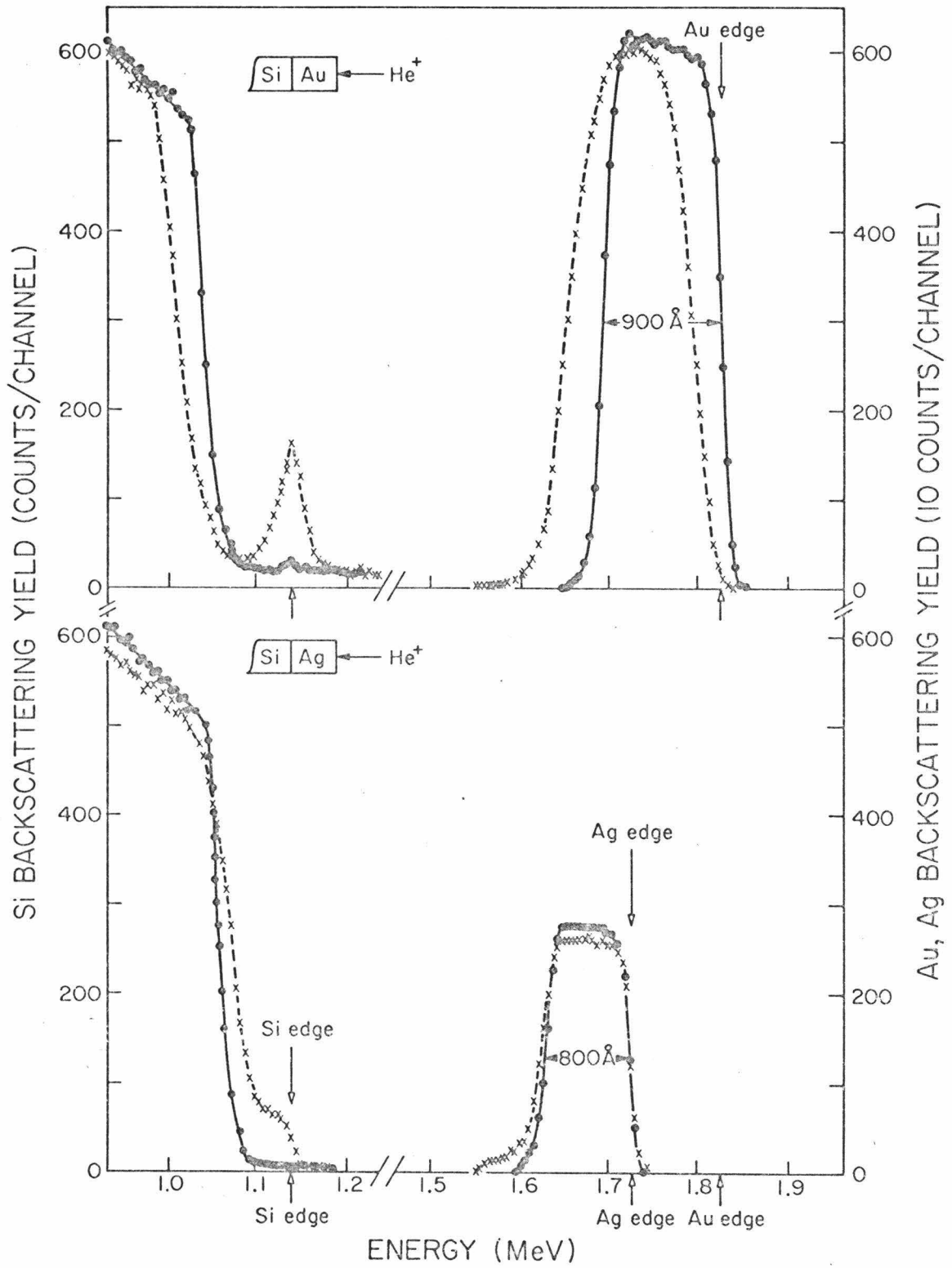at 0.47 MeV and is not shown in this figure.

Figure 3

system, the distribution is mostly confined to the metal surface as indicated in the figure by the peak located at the silicon edge of the spectrum. These silicon atoms form a closed SiO_2-like layer and cause a slight shift of the whole spectrum towards lower energy. Much less silicon accumulates on the gold surface when the ambient contains only little oxygen during the anneal.[48] On the other hand, the Si-Ag system does not show SiO_2 formation on the silver surface. No peak develops at the silicon edge and the silver spectrum does not shift. The distribution of Si in the Si-Ag system seems to be in the bulk of the metal film.

To clarify the process of low-temperature migration and the above mentioned differences between Si-Au and Si-Ag systems, it is important to establish whether this migration is limited by the silicon dislodgement at the silicon-metal interface or the silicon transport through the metal layer.

B. Importance of Silicon-Metal Interface

Samples were prepared with successively evaporated films of both gold (500Å) and silver (550Å) overlaid on silicon in both sequences. The results of backscattering analyses of such samples before and after anneal at 200 and 350°C in air for 20 min are shown in Figs. 4 and 5, respectively. When the gold lies under the silver, the

Figure 4.   Energy spectra obtained with 1.5 MeV ^{4}He ions

backscattered from a randomly positioned silicon

single crystal covered with thin layers of gold

(500Å) and silver (550Å) evaporated in succession

on'{110} surface.   Top: Spectrum after evaporation;

Bottom: Spectrum after 20 min anneal at 200°C

in air;   Right: decomposition (or unfolding) of

the gold and silver signals in step spectra where

dashed lines represent the original spectra before

anneal.

Figure 4

Figure 5. Energy spectra obtained with 2 MeV ^{4}He ions
backscattered from a randomly position silicon
single crystal covered with thin layers of silver
(550Å) and gold (500Å) evaporated in succession
on {110} surface. Top: Spectrum after evaporation;
Bottom: spectrum after 20 min anneal at 350°C in
air: Right: decomposition (or unfolding) of the
gold and silver signals in step spectra where
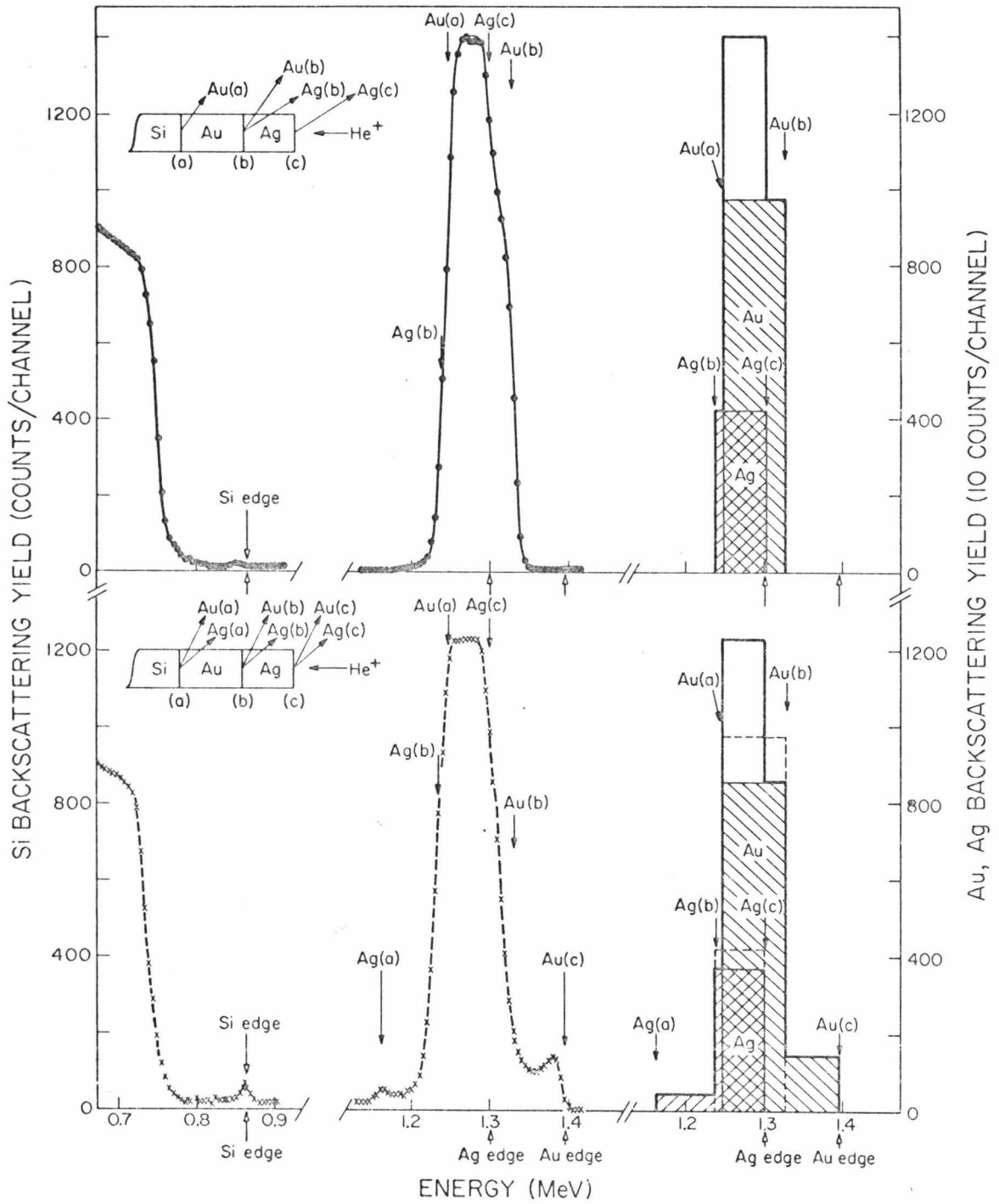dashed lines represent the original spectra before
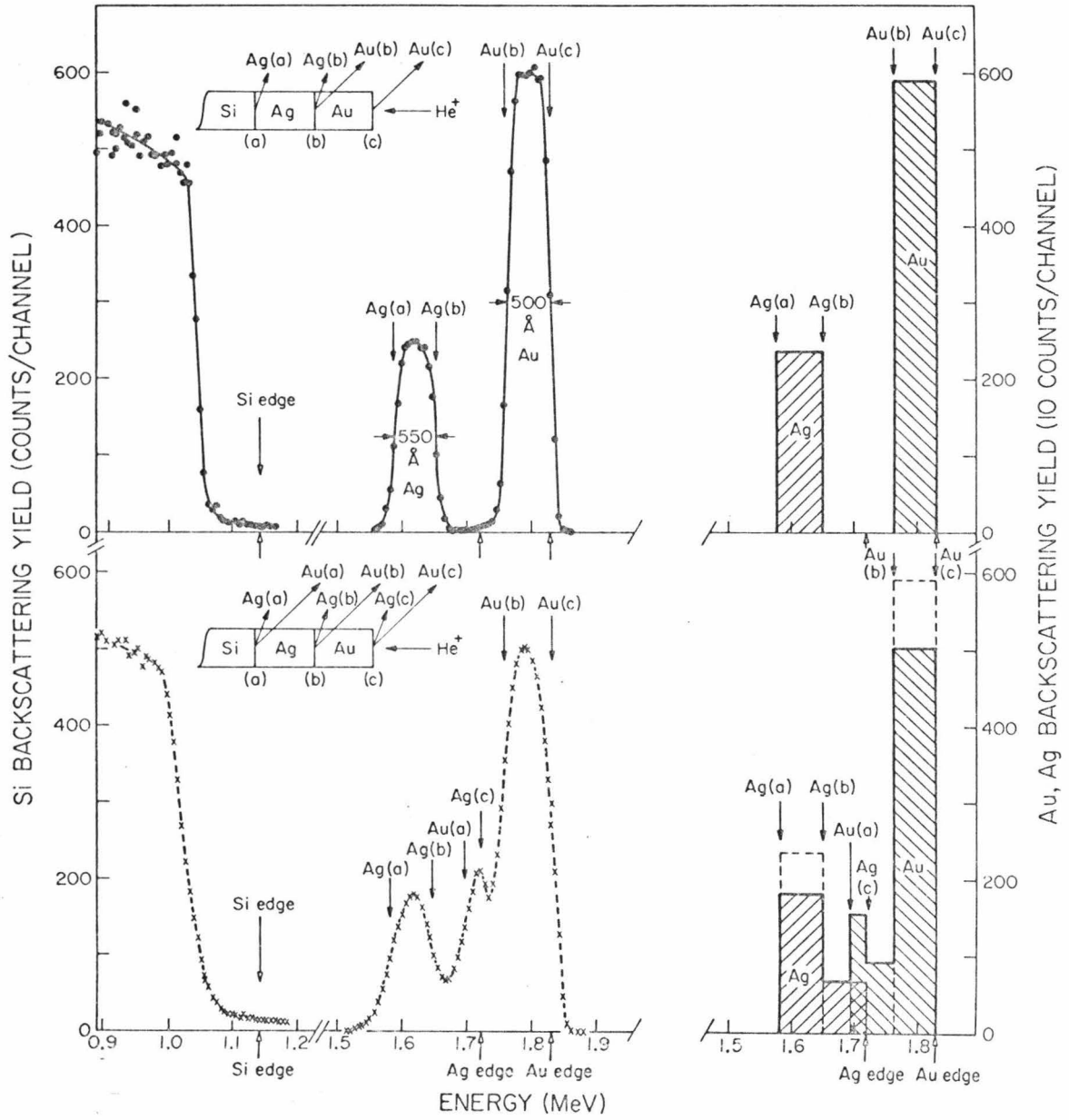anneal.

Figure 5

two signals overlap (Fig. 4) because the energy losses of the helium particles in the overlaying silver film shift the gold signal to lower energies. The combined silver-gold spectrum has been unfolded (or decomposed) by assuming simple step spectra for the individual components, and by using known values of energy loss (dE/dx) for gold and silver.[34] Similar decompositions (or unfoldings) are performed also for the spectra after anneal by assuming additionally that the thickness of every film and the total mass of each metal is conserved.* The results are shown to the right of each spectrum in Figs. 4 and 5.

When the gold film is covered with silver and the system annealed at $200^{O}C$ for 20 min. in air (lower part of Fig. 4), there is an accumulation of silicon on the silver surface. On the contrary, no trace of silicon is observed at the surface in the reverse case when the silver film is covered with gold (Fig. 5), and annealed at $350^{O}C$ in air for 20 min. This is in general agreement with the results obtained in the Si-Ag system (Fig. 1) in which the surface silicon does not appear even after annealing up to $300^{O}C$.

It seems very possible that the interaction of

---

*The mixing of the gold and silver films also changes (dE/dx) in each film. For mixtures of 10 at.% or less these changes are small and have been neglected. Of course, metal mass is not conserved at higher temperatures where significant indiffusion of metal into silicon occurs.

Si and Ag at the Si-Ag interface plays a major role in these low-temperature migration studies.

This statement is somewhat weakened by the fact that silver and gold are already slightly mixed after both anneals of Figs. 4 and 5. If that mixing were suffi-ciently inhomogeneous to provide gold-rich paths of high permeability, the presence of surface silicon in Si-Au-Ag system (Fig. 4) could possibly be explained without assum-ing an actual migration of silicon through silver. But the same paths should then occur in the inverse arrange-ment of Si-Ag-Au system (Fig. 5). However, no surface silicon is observed in this system. This again would point to the role played by the (now slightly gold-con-taining) Si-Ag interface in limiting the Si migration to the surface of the system.

The significance of the silicon-metal interface is further stressed by the following two observations. A normally prepared silicon wafer is lightly oxidized in hot nitric acid before the vacuum evaporation of a gold film. Samples thus prepared exhibit no silicon migration through the gold film at anneal temperatures as high as $300^{\circ}C$ and durations as long as one hour. A very thin oxide layer at the Si-Au interface thus suffices to sup-press silicon migration.

The second observation is that in subsequent studies of silicide formation in silicon-metal systems

(i.e. Si-Pt, Si-Pd and Si-Cr), the presence of an oxide layer at the interface could retard or even suppress the formation of the silicide phase.[46,50]

The state of silicon substrate surface strongly influences the results in these low-temperature migration studies. It is very likely that silicon surfaces sub-jected to different cleaning methods would yield varying results. Although the surface of silicon is always covered with an oxide layer, it is very important to develop a consistent procedure for cleaning the surface before these low-temperature studies are made.

C. Growth of Oxide Layer on <110>-Si

The migration of silicon atoms through metal layers with subsequent formation of oxide was investigated as a function of anneal temperature, anneal time, ambient and substrate orientation.

Figure 6 shows backscattering spectra (2 MeV He$^+$ beam) from three different samples obtained from Au-eva-porated on <110> silicon wafer after (i) two-week storage in room ambient, (ii) 20 min anneal at 150°C in air, and (iii) 20 min anneal at 200°C in air. The dotted curve is the yield obtained from a Si wafer without a gold layer. After heat treatment there is an accumulation of both Si and oxygen on the surface of Si-Au system. The position of the leading edges of the Si and oxygen and the energy

Figure 6. Backscattering spectra (2 MeV ^{4}He ions) from

samples obtained from a 900Å Au film on <110>

Si after (●) two-week storage in room ambient,

(o) 20 min anneal at 150°C in air, and (x) 20 min

anneal at 200°C in air. Energies corresponding to

scattering from surface atoms of O, Si and Au are

indicated by arrows. The dotted line indicates

the yield from an uncovered Si sample. The yield

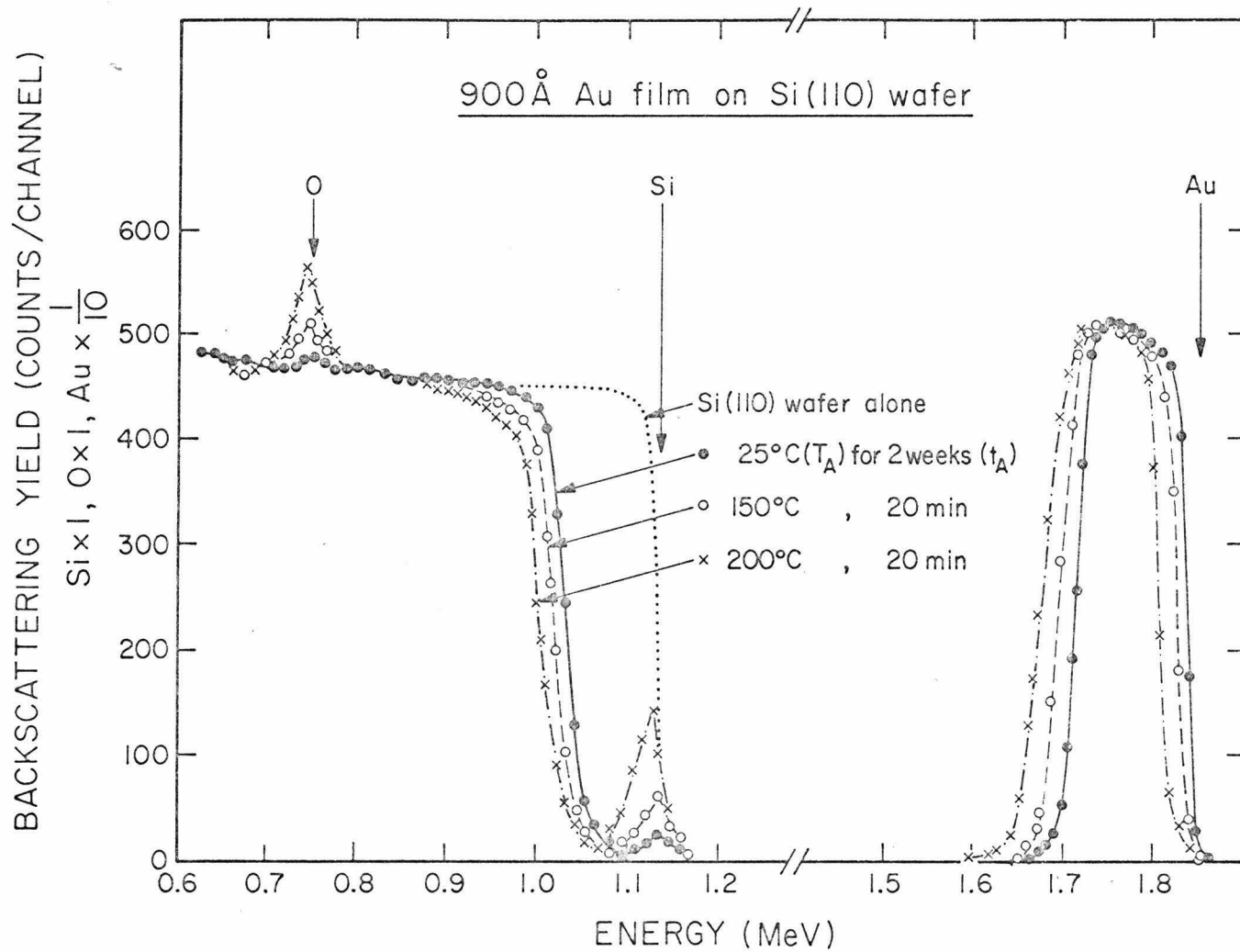from the Au layer is reduced by a factor of 10.

Figure 6

shifts of the Au- and Si-substrate signals show that the silicon-oxide layer is formed on top of the Au. The areas under the silicon and oxygen signals correspond within statistics to a composition of SiO_2 (see Eqs. 8 and 10). For the sample heated at 200^OC, the slopes of the Au leading edge and Si (oxide layer) trailing edge indicate that the oxide-layer thickness is nonuniform. This nonuniformity is more evident for thicker films and for films grown in steam ambient.

Shown in Fig. 7 are the Si and oxygen contributions for a <110> silicon sample with a 2100Å Au layer after initial Au deposition and after heat treatment for 10 and 60 min at 200^OC in air. The increased width of the surface oxide layer is responsible for the broadening of the Si and oxygen peaks. The ratio of the Si to the oxygen signals indicate a composition of SiO_2, (see Eq. 8) and the areas of the silicon peaks correspond to an average oxide-layer thickness of 360 and 1000Å for 10 and 60 min treatments, respectively. However, the slopes of the trailing edge of the Si (oxide layer) and leading edge of the contribution of the Si substrate indicate film nonuniformity for the sample annealed for 60 min.

The plateau in background yield centered around 1.0 MeV is primarily due to background counts extending from the Au peak down to low energies. Its height, although less than 1% of the height of the Au peak, is

Figure 7. Silicon and oxygen spectra for 2 MeV ^{4}He ions
backscattered from a <110> oriented Si sample
covered with 2100$\mathring{A}$ of Au (x) and heated at 200°C
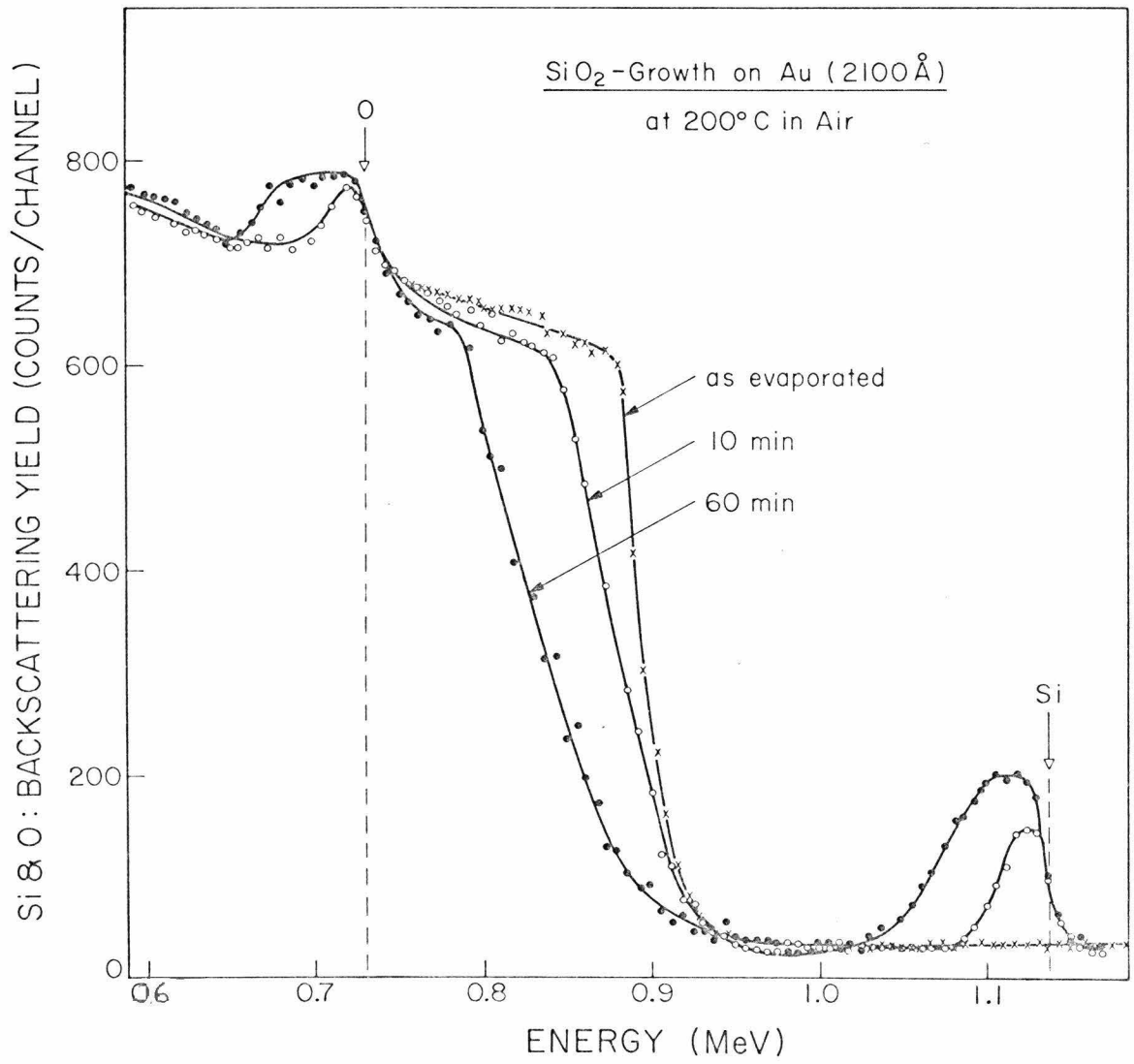in air for 10 min (o) and 60 min (⊕).

Figure 7

sufficient to mask any contribution from Si dissolved in the Au at concentrations of 5 at. % or less.

The transport of silicon through an evaporated Au layer can be demonstrated by use of silicon on sapphire samples. A 2000Å Au film was evaporated over part of a 2000Å Si film epitaxially deposited on a sapphire substrate. The sample was then heated at 200°C in air for 16 h and dipped in HF to remove the oxide layer over the Au. The samples were then exposed to KI + I_2 solution to remove both free Au and any Au-Si mixture. Backscattering spectra indicated that the Si was completely removed from the originally Au-covered portion. But there was no removal of Si from the portion originally uncovered with Au. This shows that in the originally Au-covered portion, Si moved into the Au film on heat treatment.

D. Effect of Ambient and Substrate Orientation

When silicon wafers covered with different thicknesses of gold layers were heated in a stream of forming gas (a mixture of nitrogen and hydrogen) at temperatures as high as 200 and 300°C, no significant oxide layer was detected. In fact, backscattering spectra showed no appreciable change in the silicon and gold signals from as-evaporated samples.

A gold layer 2100Å thick was evaporated onto several <110>-oriented silicon wafers and then heat

treated in air, pure O_2-gas and steam. As seen from Fig.
8, if the heat treatment is done in steam (of 1 atm.
pressure) even at 100°C the growth of the oxide layer
exceeds that for pure O_2-gas (1 atm. pressure) treatments
at temperatures as high as 300°C. The oxide growth kinet-
ics in air lie between both cases. These statements are
of a qualitative nature because the nonuniformity of the
oxide layer, especially for the steam case or for long
heat-treatment times, does not allow strong quantitative
comparisons. At these low temperatures ($100-300^{\circ}$C) the
presence of H_2O molecules leads to more rapid oxide growth
than that for oxygen molecules. This is in agreement with
the ambient effects for SiO_2 obtained in high-temperature
(above 600°C) experiments.[65,66] The growth rate in
air suggests that the moisture in the air is playing the
dominant role in the oxidation process. This implies that
the oxide-growth rate is smaller in air than in steam
owing to the smaller concentration of H_2O molecules in the
air ambient.

An effect on the orientation of the silicon sub-
strate on the oxide layer thickness is also observed.
Onto <111> and <110> Si-oriented substrates, 1800Å of gold
were evaporated simultaneously. Heat treatment of both
samples under the same condition (200°C, in air) indicated,
as seen in Fig. 9, that the growth of the oxide layer is
more rapid (about 5 times) with a <110> orientation than

Figure 8. Effects of ambient on the amount of oxide vs heat treatment time for a <110> oriented Si sample covered with 1700$\overset{\circ}{A}$ of Au. The equivalent silicon oxide layer thickness is about 800$\overset{\circ}{A}$ for 200°C treatment for 20 min in air.
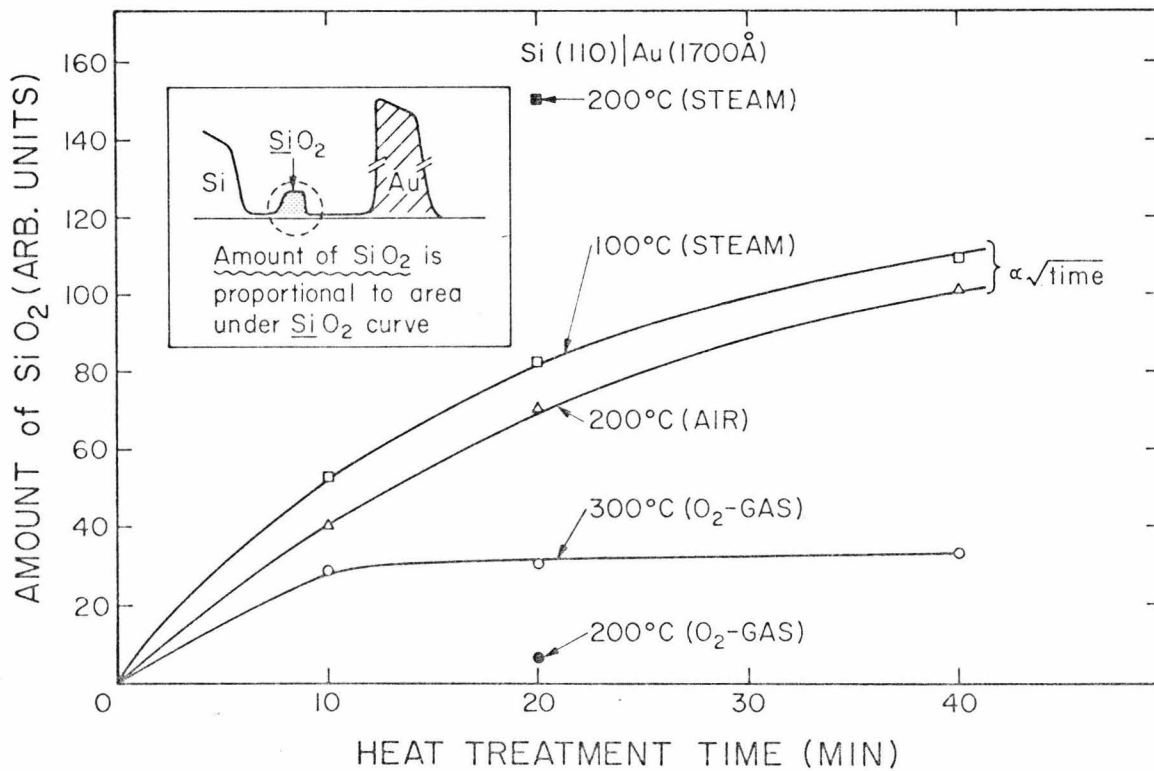
Figure 8

Figure 9. Effect of orientation on the amount of oxide
vs (heat treatment time)$^{\frac{1}{2}}$ for <110> and <111>
oriented Si samples covered with 1600$\overset{o}{\text{A}}$ of Au and
heated at 200°C in air.

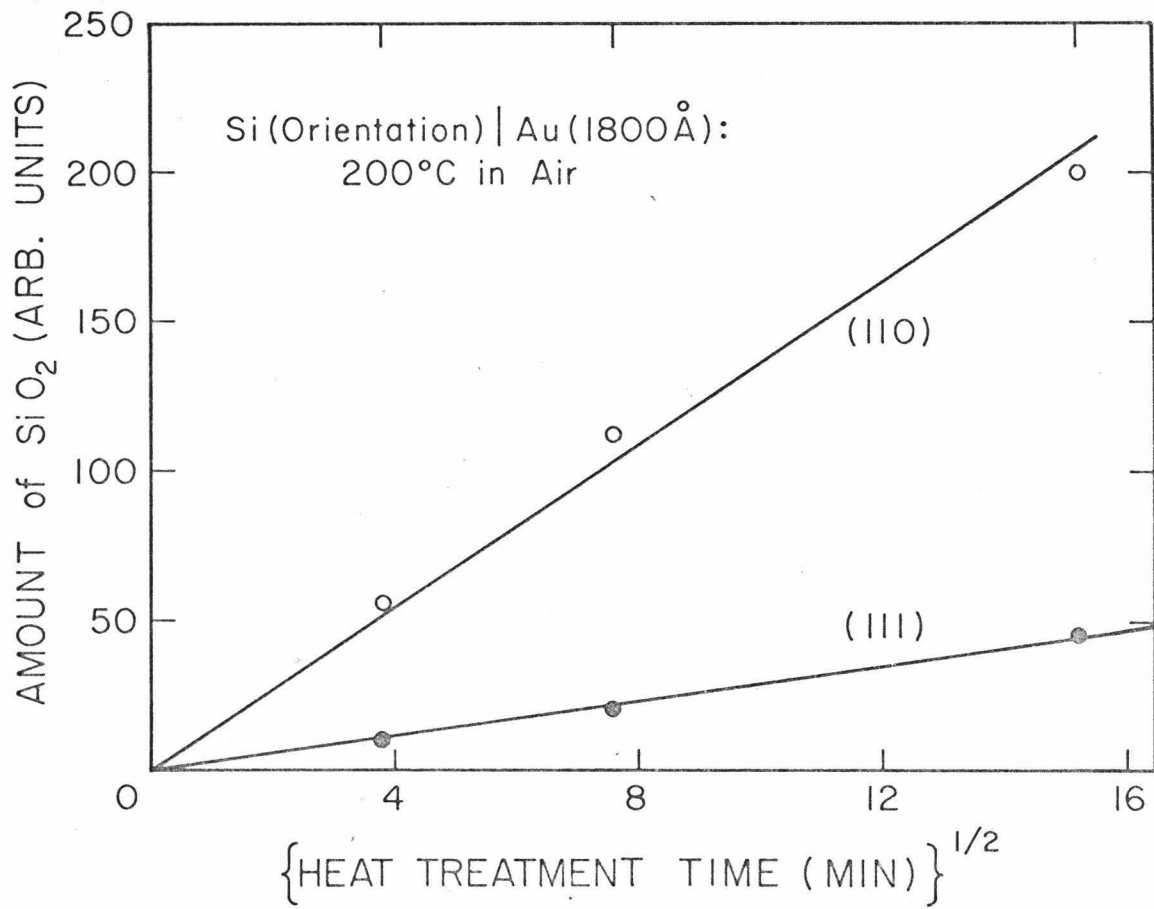Figure 9

with a <lll>. For 60 min process times, the layer thick-
nesses were 1100 and 200Å, respectively. This is even
visibly distinguishable from the obvious difference in
color changes on the surface. Similar, but not as pro-
nounced, orientation effects have been found in thermal
oxidation of silicon.[67]

    E.   Effects of Thickness of Evaporated Gold Layer

        Since the low-temperature migration effect of
silicon originated in the presence of gold on the silicon
substrate, it is interesting to investigate the effect of
gold thickness on the growth of SiO_2.

        Gold films of two different thicknesses, 400 and
1500Å, were evaporated, respectively, onto Si <110> sub-
strates. These specimens were then heated at 200°C in
air and the amount of silicon in the oxide layer as a
function of heat-treatment time was measured (Fig. 10).
Although the specimens with the thinner gold film showed
a slightly larger growth of oxide than that for thick
films for the first 10 min of heat treatment, the growth
stopped at a certain final SiO_2 thickness. For 40 min
treatment, the oxide layer was ≃ 1000Å for both samples.
For the thicker film, the growth of the oxide layer did
not saturate for times up to 640 min. Experiments with
intermediate thicknesses of Au films indicated that the
final (or saturated) oxide layer thicknesses are almost

Figure 10. Effect of Au thickness of the amount of oxide
vs heat treatment time for <110> oriented Si
samples covered with 1500Å (●) and 400Å (o) of
Au and heated at 200°C in air. The oxide layer
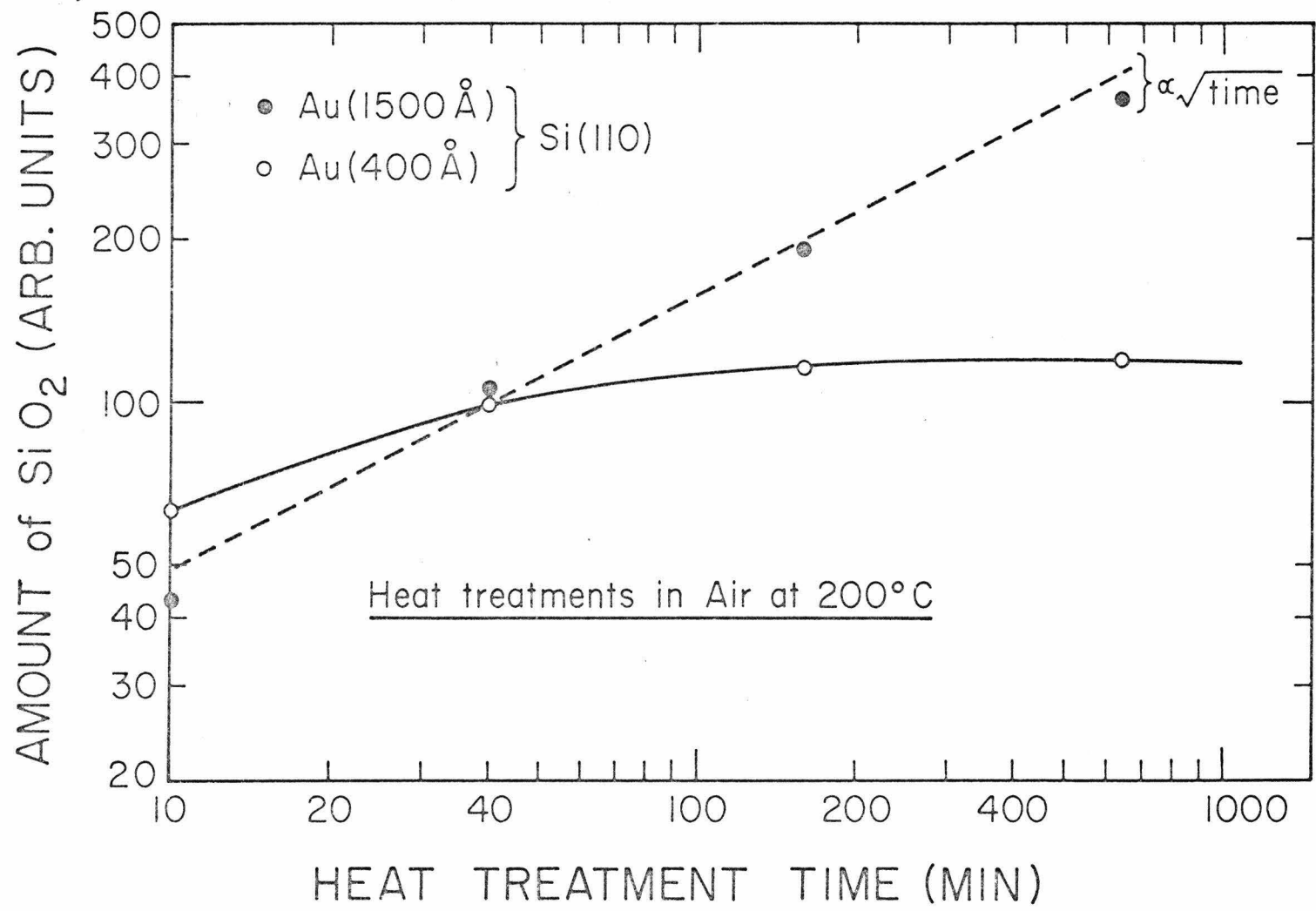was about 1000Å for 40 min heat treatment.

Figure 10

proportional to (nearly twice) that of the original
gold film.

The above effect was examined in more detail. Two
specimens with original gold layers of 400$\overset{o}{A}$ and 1500$\overset{o}{A}$ were
pre-heated at 200°C in air for 160 min to induce an oxide
layer. These oxide layers were then dissolved by dilute
HF solution and the samples were heated again at 200°C in
air for 160 min. After this treatment, the specimen with
400$\overset{o}{A}$ Au thickness produced a barely detectable oxide layer,
while the specimen with 1500$\overset{o}{A}$ gold layer was found to have
an observable oxide layer. Further experiments with
shorter time preheat treatments of 40 min produced basi-
cally the same results after the second heating: a barely
detectable oxide layer on the 400$\overset{o}{A}$ Au film and an appre-
ciable amount of SiO_2 on the 1500$\overset{o}{A}$ Au film.

Other experiments indicated that the amount of
oxide found after the second heat treatment depends on the
thickness of the oxide layer after preheat. For example,
for the sample with 1500$\overset{o}{A}$ Au film, the oxide layer follow-
ing the second treatment was somewhat thicker for the
40 min preheat case than that for the 160 min preheat.
Also, in other samples, no further oxide growth was ob-
served after removal of a "saturated" oxide thickness
formed in the initial treatment.

The dependence of the oxide thickness on original
evaporated gold film thickness, and the saturation effect

of the oxide after heat treatment led to an investigation of the Si-Au interface. A comparison of backscattering spectra of the heated Si-Au samples after removal of oxide layer with those of alloyed Si-Au samples was made.

The Si-Au alloyed samples were prepared by heating a silicon wafer covered with 1500$\overset{\circ}{A}$ Au layer in forming gas (a non-oxidizing ambient) for 30 min at a temperature of 415°C (above the Si-Au eutectic point). These samples were then heated in air for 160 min. No oxide layer was detected on these alloyed samples either visually or from analysis of backscattering data (Fig. 11b). Figure 11a shows backscattering spectrum of an unalloyed sample of Si with 1500$\overset{\circ}{A}$ Au after heat treatment at 200°C in air for 640 min and then removing the SiO$_2$ layer by dipping in HF. The two spectra (a and b) are quite similar with the broad tail on the Au signal and a reduced contribution from Si near the surface. This again leads to the conclusion that there is appreciable interaction of Si and Au at the Si-Au interface.

F.   Discussion and Model

The formation of the oxide layer is initiated by the release of the silicon atoms from the single-crystal substrate and the subsequent migration of the atoms through the Au layer. This is indicated schematically in Fig. 12. At the interface, the silicon atoms react with oxygen to

Figure 11. Spectra from 2 MeV ^{4}He ions backscattered from

two Si samples covered with a 1500$\overset{\text{o}}{\text{A}}$ Au layer and

treated separately: (a) for 640 min at 200$^\text{o}$C in

air and then dipped in HF to remove the oxide

layer, (b) for 30 min at 415$^\text{o}$C in forming gas. In

case (b) the sample was not exposed to HF. The

dashed curve in (a) represents the spectra taken

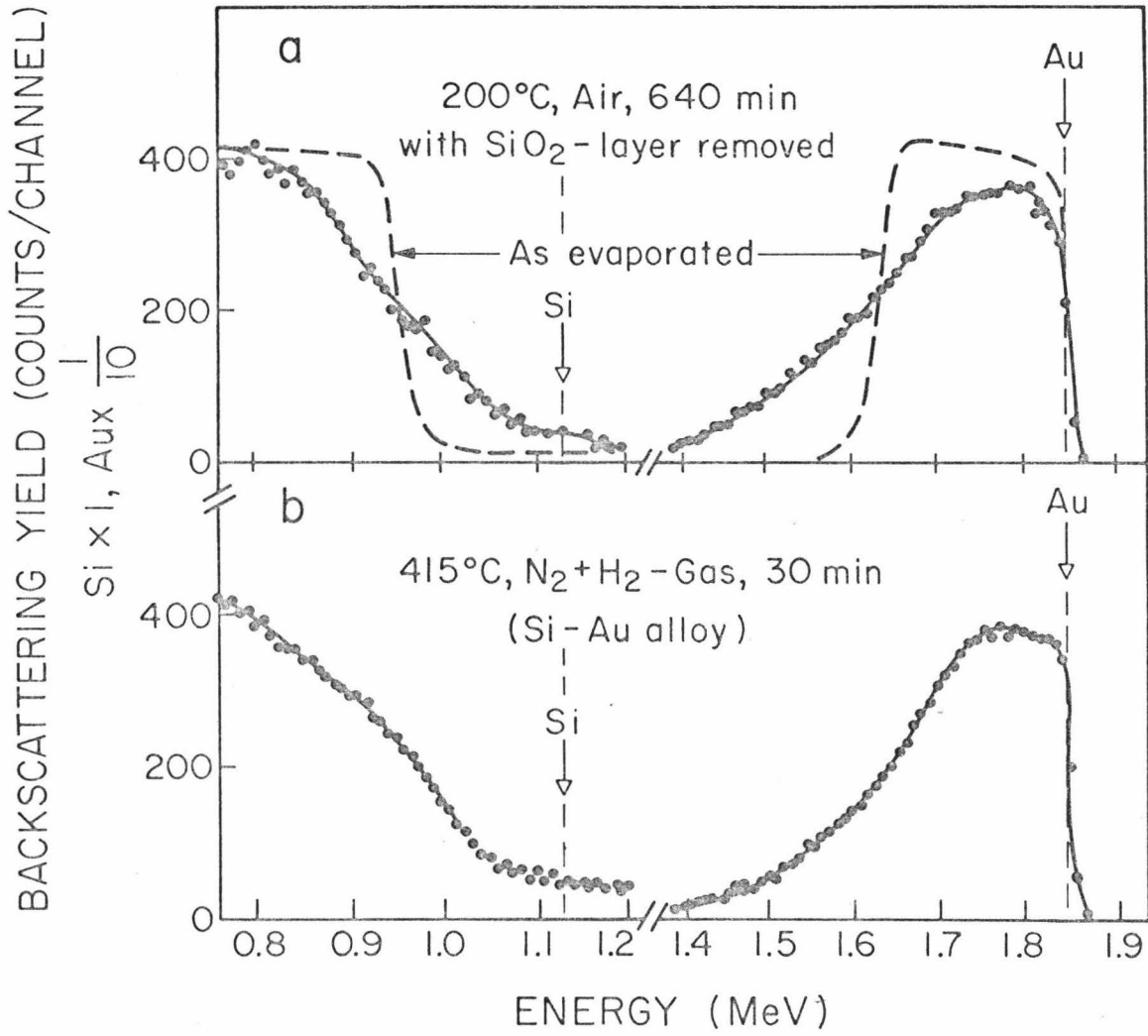after evaporation of the Au layer.

Figure 11

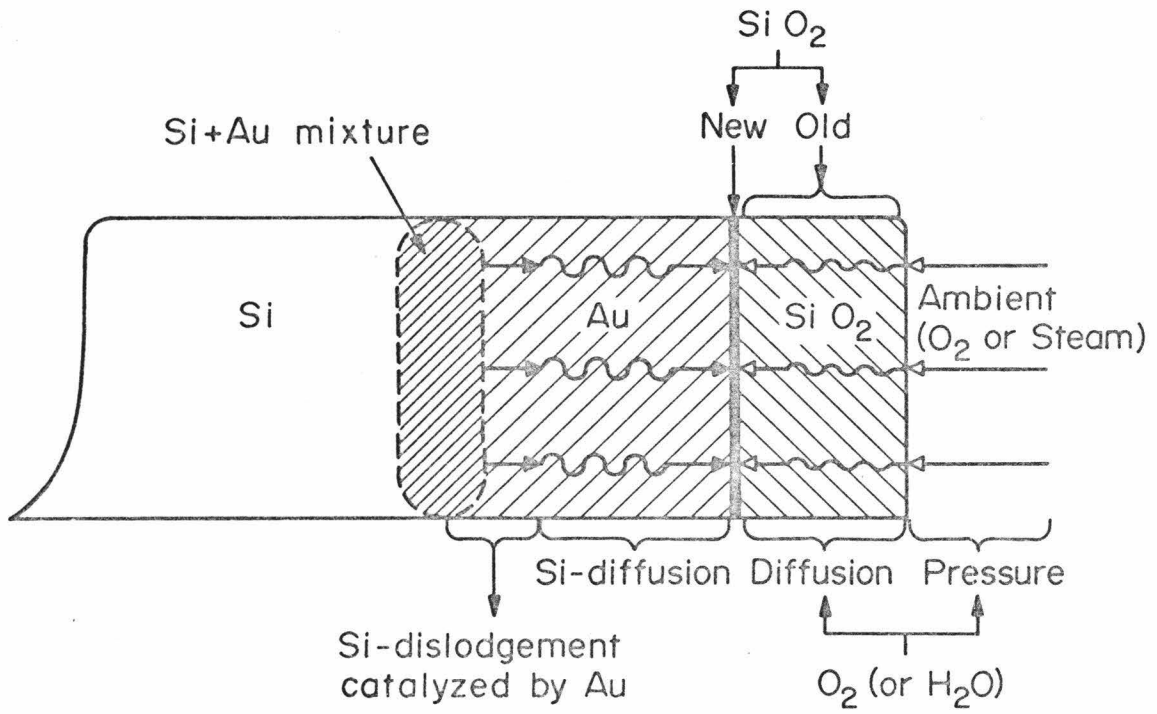Figure 12. Model for the mechanism of SiO_2 formation at temperatures below the Si-Au eutectic point.

Figure 12

form an SiO$_2$ layer. The two possible places at which SiO$_2$ layer can grow are the Au-SiO$_2$ interface (oxygen diffusion through the oxide layer) and the SiO$_2$-ambient interface (Si diffusion through the oxide layer). On basis of strong ambient effects (Fig. 8) it is proposed here that the former case holds, i.e., that the oxidizing species diffuse through the oxide layer (Fig. 12). This is similar to the process of thermal oxidation of Si.

The Au-Si interface plays a role. The presence of a thin oxide layer at the interface between Au and Si can prevent the release of silicon. Variations in the thickness of this interface oxide layer could be responsible for the nonuniform thickness of the oxide layer grown on the Au surface. The characteristics of the Au-Si interface may also be responsible for the fact that the growth of the oxide layer is about 5 times faster on <110> oriented silicon than on <111> oriented samples.

The thickness of the deposited Au film also has a strong effect on the growth of the oxide layer. The initial oxide growth rate decreases with increased thickness of the Au layer. However, the most striking phenomenon is the termination of the oxide growth for long process times. The final oxide layer thickness increases with increased thickness of the Au film. After removal of a "saturated growth" oxide layer by HF no further oxide growth is observed following heat treatment.

It is suggested that the termination of the oxide growth is due to the formation of the Au-Si mixture which prevents the further release of silicon atoms. The SiO_2 layer formation is provided through the interaction of both silicon and gold at the interface to form a Au-Si mixture as a byproduct. Based on this hypothesis, the oxide layer will grow until all the Au has interacted with the Si. Consequently the oxide growth terminates sooner for a thin Au film than for a thicker one.

Some support for this concept is provided by the behavior of Si-Au samples heated above the eutectic point in forming gas. No oxide layer was detected following subsequent heat treatment in air. In an alloyed sample, it is reasonable to consider that all the Au has intermixed with Si. Backscattering spectra (Fig. 11) from an alloyed sample and a sample heated until oxide growth terminated showed similar Au and silicon distributions. The broad tail on the Au signal is suggestive of Au-Si intermixing. This tail was not observed in samples heated at $200^{\circ}C$ (below the eutectic) in forming gas when no oxide layer was formed. This suggests that marked Au-Si intermixing occurs when either an oxide layer is formed or when the sample is heated above eutectic.

V. SUMMARY

We have shown the application of backscattering techniques to study some low-temperature migration phe_ nomena. In particular, work on Si-Au and Si-Ag systems has been presented. The interaction of Si with the metal layers with the subsequent migration of Si through the layer and eventual formation of an oxide in an oxidizing ambient has been investigated.

When a silicon wafer is covered with evaporated gold film and heated at temperatures below the Si-Au eutectic point ($375^{O}C$), a silicon dioxide layer is formed on top of gold if the ambient contains a trace of water or oxygen molecules. Steam gas is the most effective ambient as it induces oxide growth far more rapidly even at $100^{O}C$ than does pure oxygen gas at $300^{O}C$.

There are major differences between thermal oxi- dation and the present Si-Au system where oxide-formation temperature is low, the oxide layer is nonuniform in thick- ness, and the final amount of SiO_2 formed is proportional to the original thickness of the evaporated Au layer.

We present a model associating the above effects with the properties of the Si-Au interface. The model proposed is that the interaction between Au and the sub- strate Si crystal at the Si-Au interface provides Si atoms

which can diffuse to the Au surface. There, Si atoms react with oxidizing molecules which had diffused through the existing oxide layer.

This initial study of the interaction and migration of Si in metal films at low temperatures led to investigations of silicide formation and subsequent work on silicon-metal systems using the backscattering technique.[48-54]

REFERENCES

1. E. Bøgh and E. Uggerhøj, Nucl. Inst. Method 38, 216 (1965).

2. J.A. Davies, J. Denhartog and J.L. Whitton, Phys. Rev. 165 345 (1968).

3. S.T. Picraux, J.A. Davies, L. Eriksson, N.G.E. Johansson and J.W. Mayer, Phys. Rev. 180, 873 (1969).

4. E. Bøgh, Can. J. Phys. 46, 653 (1968).

5. L.C. Feldman and J.W. Rodgers, J. Appl. Phys. 41, 3776 (1970).

6. J.E. Westmoreland, J.W. Mayer, F.H. Eisen and B. Welch, Rad. Effects 6, 161 (1970).

7. J.W. Mayer, L. Eriksson and J.A. Davies, Ion Implantation in Semiconductors (Academic, New York, 1970), Ch. 4.

8. O. Meyer, J. Gyulai and J.W. Mayer, Surface Sci. 22, 263 (1970).

9. S.T. Picraux, Appl. Phys. Lett. 20, 91 (1972).

10. I.V. Mitchell, M. Kamoshida and J.W. Mayer, J. Appl. Phys. 42, 4378 (1971).

11. E. Rimini, E. Lugujjo and J.W. Mayer, Phys. Lett. 37A, 152 (1971).

12. E. Rimini, E. Lugujjo and J.W. Mayer, Phys. Rev. B6, 716 (1972).

13. J.F. Ziegler, J. Appl. Phys. 43, 2973 (1972).

14. R. Hart, Rad. Effects 6, 51 (1970).

15. E. Keil, E. Zeitler and W. Zinn, Z. Naturforsch. 15a, 1031 (1960).

16. G. Moliere, Z. Naturforsch 3a, 78 (1948).

17. L. Meyer, Phys. Stat. Solidi B44, 253 (1971).

18. F. Bernhard, J. Lippold, L. Meyer, S. Schwalse and R. Stolk, in Atomic Collision Phenomena in Solids, Edited by D.W. Palmer, W.M. Thompson and P.D. Townsend (North-Holland, Amsterdam, 1970), p. 633.

19. H.H. Andersen and J. Bøttiger, Phys. Rev. B4, 2105 (1971).

20. W.T. Scott, Rev. Mod. Phys. 35, 231 (1963).

21. R.B. Leighton, Principles of Modern Physics, (McGraw-Hill, New York, 1959), Ch. 14.

22. E.J. Williams, Proc. Roy. Soc. A169, 531 (1939).

23. E. Rutherford, Phil. Mag. 21, 669 (1911).

24. G. Wentzel, Ann. Physik 69, 335 (1922).

25. E.J. Williams, Phys. Rev. 58, 292 (1940).

26. J. Lindhard, Kgl. Danske Videnskab Selskab, Mat. Fys. Medd. 34, 14 (1965).

27. S. Datz, C. Erginsoy, G. Leibfried and H.O. Lutz, Ann. Rev. of Nucl. Sci. 17, 129 (1967).

28. S.T. Picraux, Ph.D. Thesis, California Institute of Technology, June 1969.

29. J.U. Andersen, Kgl. Danske Videnskab. Selskab, Mat.

Fys. Medd. $\underline{36}$, 7 (1967).

30. J.F. Ziegler and B.L. Crowder, Appl. Phys. Lett. $\underline{20}$, 178 (1972).

31. C.G. Darwin, Phil. Mag. $\underline{28}$, 499 (1914).

32. J.F. Ziegler and J.E.E. Baglin, J. Appl. Phys. $\underline{42}$, 2031 (1971).

33. J.B. Marion and F.C. Young, Nuclear Reaction Analysis, p. 142, American Elsevier, New York, 1968.

34. J.F. Ziegler and W.K. Chu (unpublished, 1973).

35. J.A. Davies, J. Denhartog and J.L. Whitton, Phys. Rev. $\underline{165}$, 345 (1968).

36. F.H. Eisen and J. Bøttiger (to be published in Thin Solid Films).

37. J.M. Khan, D.L. Potter, R.D. Worley and H.P. Smith, Phys. Rev. $\underline{148}$, 413 (1966).

38. G. Foti, F. Grasso, R. Quattrocchi and E. Rimini, Phys. Rev. $\underline{B3}$, 2169 (1971).

39. N.F. Mott and H.S.W. Massey, The Theory of Atomic Collisions, (Oxford University Press, London, 1949) Second edition, Chap. VII, Secs. 4 and 5.

40. H. Goldstein, Classical Mechanics, pp. 58-92, (Addison-Wesley, Cambridge, Mass., 1950).

41. J. Lindhard, V. Nielsen and M. Scharff, Mat. Fys. Medd. Dan. Vid. Selsk. $\underline{36}$, 10 (1968).

42. Peter Sigmund (private communication) points out that this term is an artifact from the specific approxi-

mation procedure used by Meyer.

43. E.H. Rhoderick, Prit, J. Appl. Phys., Vol. 3, p. 1153 (1970).

44. W. Tantraporn, IEEE Trans. Electron Devices, Vol. ED-19, pp. 331-338, March 1972.

45. A. Hiraki, E. Lugujjo, M-A. Nicolet and J.W. Mayer, Phys. Stat. Solidi(a) 7, 401 (1971).

46. A. Hiraki, E. Lugujjo and J.W. Mayer, J. Appl. Phys. 43, 3643 (1972).

47. A. Hiraki and E. Lugujjo, J. Vac. Sci. Technol. 9, 155 (1972).

48. A. Hiraki, M-A. Nicolet and J.W. Mayer, Appl. Phys. Lett. 18, 178 (1971).

49. R.W. Bower and J.W. Mayer, Appl. Phys. Lett. 20, 359 (1972).

50. R.W. Bower, Ph.D. Thesis, California Institute of Technology, May 1973.

51. J.F. Ziegler, J.W. Mayer, C. Kircher and K.N. Tu, J. Appl. Phys. 44, 3851 (1973).

52. K.N. Tu, J.F. Ziegler and C.J. Kircher, Appl. Phys. Lett. 23, 493 (1973).

53. H. Krautle, W.K. Chu, M-A. Nicolet, J.W. Mayer and K.N. Tu (to be published).

54. C.J. Kircher, J.W. Mayer, K.N. Tu and J.F. Ziegler, Appl. Phys. Lett. 22, 81 (1973).

55. J.O. McCaldin and H. Sankur, Appl. Phys. Lett. 19,

524 (1971).

56. G. Ottaviani, D. Sigurd, V. Marrello, J.W. Mayer and J.O. McCaldin (to be published in J. Appl. Phys.).

57. D. Sigurd, G. Ottaviani, H.J. Arnal and J.W. Mayer (to be published in J. Appl. Phys.).

58. M-A. Nicolet, J.W. Mayer and I.V. Mitchell, Science 177, 841 (1972).

59. E.J. Franzgrote, J.H. Patterson, A.L. Turkevich, T.E. Economou and K.P. Sowinski, Science 167, 376 (1970).

60. J.H. Patterson, A.L. Turkevich and E.J. Franzgrote, J. Geophys. Res. 70, 1311 (1965).

61. A. Turos and Z. Wilhelmi, Nukeonika 13, 795 (1968).

62. E. Bøgh, Proc. Royal Soc. A311, 35 (1969).

63. J. Gyulai, J.W. Mayer, V. Rodriguez, A.Y.C. Yu and H.J. Gopen, J. Appl. Phys. 42, 3578 (1971).

64. M. Hansen and K. Anderko, Constitution of Binary Alloys, McGraw-Hill, New York, 1958.

65. A.S. Grove, Physics and Technology of Semiconductor Devices (Wiley, New York, 1967), Chap. 3.

66. B.E. Deal and A.S. Grove, J. Appl. Phys. 36, 3770 (1965).

67. J.R. Ligenza, J. Phys. Chem. 65, 2011 (1961).